Fabrication and Physics of CdTe Devices by Sputtering

Annual Technical Report for the Period

June 1, 2006 to May 31, 2007

(Deliverable D.2.8)

Contract No. RXL-5-44205-01

Alvin Compaan, principal investigator

Robert Collins, co-principal investigator

Victor Karpov, co-principal investigator

Dean Giolando, co-investigator

NREL technical monitor: Bolko von Roedern

Department of Physics and Astronomy
The University of Toledo
Toledo, OH 43606

Summary

There are three overall emphases in this subcontract: 1) improving our understanding of key aspects of the CdS/CdTe solar cell device physics, 2) improving our understanding of magnetron sputtering and imcreasing the sputter deposition rate while maintaining high device quality, and 3) reducing the thickness of CdTe layers in the CdS/CdTe cell below 0.5 μm while maintaining voltage and fill factor.

In Phase II of this subcontract, much of our effort on device physics has focused on studies of the optical and morphological properties of CdS and CdTe films using spectroscopic ellipsometry. This has been carried out both *in situ* in real time during the sputter deposition processes and *ex situ* on films after sputter deposition is interrupted at different stages or after the $CdCl_2$ processing is completed. Other characterization has included EXAFS and high resolution TEM and EDS. Using transparent back contacts we have begun to explore carrier collection through the bifacial response of cells with CdTe layers between 0.7 and 2.3 μm. We have sought better understanding of the factors controlling growth rates by studying the dependence on gas pressure as well as rf power paying close attention to film morphology and strain. We have explored alternative shunt passivation treatments and have modeled the fundamental physics of ultrathin solar cells.

Highlights of accomplishments during Phase II include:

- The nucleation and coalescence behaviors of CdTe, CdS, and alloys of CdS_xTe_{1-x} have been studied in detail by real time spectroscopic ellipsometry (RTSE) and have led to insights into the observed structural evolution of the films, as reported in the Phase I final report. Transitions as functions of substrate temperature T from initial islanding to an initial dense layer then islanding are observed at T=160°C and 260°C for CdS and CdTe, respectively.

- By combining ex situ SE and transmittance spectroscopy, a full set of reference dielectric functions have been obtained for the components of TEC-15 glass, the CdS, and the as-deposited and $CdCl_2$-treated CdTe. Such a database has been applied to characterize the layer thicknesses and interface structure of CdTe solar cells, complete with the exception of the back contact. Measurements through the glass as well as from the back CdTe, the latter after Br_2-methanol smoothening etches, give consistent results and demonstrate through-the-glass measurement capability for on-line monitoring.

- The dielectric functions of CdS_xTe_{1-x} alloys have been determined, and this database has been applied for RTSE characterization of the ion mixing and interdiffusion that occurs during the formation of smooth CdS/CdTe heterojunctions. A tail of S diffusion corresponding to x=0.02 is detected up to ~ 100 Å from the interface of the as-deposited heterojunction -- determined using a virtual interface analysis of RTSE data.

- In depth analysis of the CdTe and CdS dielectric functions for films prepared at different substrate temperatures have provided the temperature coefficients, group speeds, and stress coefficients of the E_0 (band gap) transition as well as the higher energy critical point transitions. Such results demonstrate the possibility of measuring the temperature,

grain size, and stress for both CdS and CdTe in a single on-line measurement through the glass.

- The ability to depth profile grain size and strain of $CdCl_2$ treated and untreated CdTe solar cells (without back contact) has been established through successive Br_2-methanol etch steps. The results show that the strain in the as-deposited films is relaxed upon $CdCl_2$ treatment, and that the grain size increases considerably upon treatment; however, the grain size nearest the CdS interface is larger than that at the near surface.

- Using high resolution TEM and EDS in combination with EXAFS studies of Cu in CdS/CdTe device structures, we find that a Cu:Au alloy forms at the back contact with little Cu observable in the CdTe beyond 10 nm from the CdTe/Au interface when a Cu(3nm)/Au(20nm) contact is used.

- We have achieved a short-circuit current ratio of 0.9 for back-side to front-side illumination with cells having 0.7 μm of CdTe and a back contact of ZnTe:N/ITO.

- We have shown that the much less toxic pyrrole and be used in place of aniline as a light-activated, shunt passivation treatment to the back surface of CdTe prior to contact application.

- We have modeled the physics of ultrathin PV with film thickness less than the depletion width and less than the diffusion width (1 μm or less) for different cases having grain sizes much less than, approximately equal to, and greater than the film thickness. We predict situations of large capacitive energy fluctuations that will lead to shunting breakdown.

TABLE OF CONTENTS

Summary i
Table of Contents iii
List of Figures v
List of Tables 9
1. Introduction 1
2. Nucleation and Growth of CdTe, CdS, and CdS_xTe_{1-x} 2
   2.1. Introduction 2
   2.2. Experimental Details and Deposition Processes 2
   2.3. Nucleation of CdTe and CdS 5
   2.4. Nucleation of CdS_xTe_{1-x} 7
3. $CdCl_2$ Treatment of CdTe 8
4. Modeling Solar Cell Structures 14
   4.1. Component Optical Properties 15
   4.2. Thickness and Basic Structural Information 20
   4.4. Expansion to Temperature, Grain Size, and Strain 30
      4.4.1. Temperature Effects 30
      4.4.2. Grain Size Effects 34
      4.4.3. Strain Effects 37
5. EXAFS of Light Stressed Cells with Complete Cell Structure 41
   5.1. Introduction 41
   5.2. Sample preparation 41
   5.3. Cu_2O and Cu/Au alloy in Cells Before and After Light Soaking 43
   5.4. Conclusion 48
6. High Resolution Transmission Electron Microscopy on Back Contact Region 49
   6.1. Introduction 49
   6.2. High Resolution TEM and Sample preparation 49
   6.3. Interfacial Cu-Rich Layer 50
   6.4. Distribution of Copper in Near Back Contact Region 50
   6.5. Conclusion 53
7. Bifacial Transparent Back Contacts 54
   7.1. Introduction 54
   7.2. Performance of 2.3 μm Cells with Different Back Contacts 55

7.3. Effect of ITO Deposition Temperature 56
7.4. 1.8 and 0.7 μm cells with ZnTe:N/ITO as Back Contact 57
7.5. Bifacial Measurements 57
7.6. Conclusions 59
8. High Growth Rate Magnetron Sputtering of CdTe 60
8.1. Introduction 60
8.2. Sample Preparation and Characterization 60
8.3. Conclusions 65
9. XRD and SEM Studies of Pyrrole Treatment 66
9.1. IV-Characterization 66
9.2. GIXRD-Characterization 68
9.3. SEM-Characterization 69
10. Modeling of Ultrathin Cells 71
11. References (from section 1 through 10) 73
12. Publications 75
12.1. Refereed papers published or in press 75
12.2. Publications and presentations at DOE Program Reviews 76
13. Project Personnel 77
13.1. Postdoctoral Associate 77
13.2. Graduate Students (with Principal Advisor) 77
13.3. Undergraduate Students 77
13.4. Technical Assistants 77
Appendix A 78

LIST OF FIGURES

Figure 2.1 Deposition rate as a function of substrate temperature for the CdTe and CdS series studied in detail in this report. 3
Figure 2.2 The calibration of CdTe and CdS deposition rates as functions of target RF power. 4
Figure 2.3 Measured deposition rate versus composition for ~200 Å thick CdS_xTe_{1-x} alloys 4
Figure 2.4 Nucleation modes of CdS thin films deposited at different temperatures: (a) 145°C; (b) 160°C; (c) 225°C. 5
Figure 2.5 Key nucleation parameters: ds when the first complete dense ML appears; db when the first surface roughness monolayer formed; peak nucleation height before coalescence. 6
Figure 2.6 Nucleation and surface roughness evolution characteristics of CdS_xTe_{1-x} alloy deposition on c-Si wafer substrates at a deposition temperature of 190°C. 7
Figure 3.1 Critical point energies (upper panel) and widths (lower panel) as functions of CdTe bulk layer thickness during etching by Br_2+methanol for co-deposited CdTe films processed in three different ways: (i) as-deposited, (ii) annealed in Ar for 30 min, and (iii) $CdCl_2$ treated for 5 min. 9
Figure 3.2 Relative void volume fractions as functions of CdTe bulk layer thickness during etching by Br_2+methanol for co-deposited CdTe films processed in three different ways: (i) as-deposited, (ii) thermally annealed for 30 min, and (iii) $CdCl_2$-treated for 5 min. 9
Figure 3.3 Energy of the E_1 transition as a function of CdTe bulk layer thickness in successive Br2-methanol etching steps for a sputtered CdTe solar cell. 10
Figure 3.4 Broadening parameter Γ_{E1} as a function of CdTe bulk layer thickness in successive Br2-methanol etching steps for a sputtered CdTe solar cell. 10
Figure 3.5 Energy of the E_1 transition and its width Γ_{E1} as functions of CdTe bulk layer thickness in successive Br_2-methanol etching steps for ~3000 Å thick CdTe films. 11
Figure 3.6 Energy of the E_1 transition (upper panel) and its width Γ_{E1} (lower panel) as functions of CdTe bulk layer thickness in successive Br2-methanol etching steps for ~3000 Å thick CdTe films. 11
Figure 3.7 Void volume fraction as a function of CdTe bulk layer thickness in successive Br_2-methanol etching steps for ~3000 Å thick CdTe films in a second experiment for comparison with the results in Figure 3.2. 12
Figure 4.1 Mapping SE configuration with focusing optics to collect reflection from the (TEC glass)/(solar cell) interface. 14
Figure 4.2 Optical properties expressed in terms of the dielectric function of three of the four components of TEC-15 glass including (a) the soda lime glass substrate, (b) the near-substrate undoped SnO_2, and (c) the SiO_2 interlayer. 15
Figure 4.3 Dielectric functions of SnO_2:F, the top-most layer of the TEC-15 substrate deduced in the analysis that includes a fit to the ellipsometric angles (Ψ, Δ) and the transmittance T. 16
Figure 4.4 Index of refraction and extinction coefficient of SnO_2:F, the top-most layer of the TEC-15 substrate deduced in the analysis that includes a fit to the ellipsometric angles (Ψ, Δ) and the transmittance T. 17

Figure 4.5 Best fit analytical models of the room temperature dielectric functions for as-deposited (no treatments; broken line) and $CdCl_2$-treated for 5 min at 387°C (solid line) CdTe films; (right) a comparison between the $CdCl_2$-treated CdTe film (solid line) and single crystal CdTe (broken line). 18
Figure 4.6 Comparison of the ordinary dielectric function of bulk hexagonal single crystal CdS and two polycrystalline CdS thin films deposited in this study..... 19
Figure 4.7 (a) SE angle ψ and (b) the transmittance T at normal incidence ($\theta_i = 0^o$) for a TEC-15 substrate.. 20
Figure 4.8 Structural parameters and their confidence limits deduced in a combined analysis of ellipsometric angles (ψ, Δ) and normal incidence transmittance T for a TEC-15 glass substrate. 21
Figure 4.9 Optical configuration for ex situ SE data acquisition from the CdTe free surface after etching steps and from the prism/glass substrate side without CdTe etching. 22
Figure 4.10 The smoothening effect of Br_2+methanol etching of CdTe. 22
Figure 4.11 Ex situ SE spectra in (ψ, Δ) (symbols) for a CdTe solar cell after $CdCl_2$ treatment, but before back contact formation, as measured from the prism/glass side. 23
Figure 4.12 Ex situ SE spectra in (ψ, Δ) (symbols) from the free CdTe surface after 8 Br_2+methanol etching steps. 24
Figure 4.13 A comparison of the structural parameters deduced from spectra collected from the CdTe surface after eight etching steps and from spectra collected through the prism/glass. 25
Figure 4.14 CdS and CdTe/CdS interface layer thicknesses deduced from spectra collected through the prism/glass and from spectra collected from the CdTe surface in successive etches..... 25
figure 4.15 Proposed interface layers in a TEC-15/CdS/CdTe structure for on-line analysis of CdTe solar cell structures by spectroscopic ellipsometry..... 26
Figure 4.16 Complex dielectric functions versus x obtained in real time for ~200 Å thick CdS_xTe_{1-x} alloys at T = 190°C. 27
Figure 4.17 Complex dielectric functions versus x obtained in situ for ~200 Å thick CdS_xTe_{1-x} alloys after cooling the deposited film to 17°C 28
Figure 4.18 Optical model and characteristics of the virtual interface analysis method for investigation of CdS/CdTe interface formation by RTSE 28
Figure 4.19 Composition profiles $x(d_b)$ in CdS_xTe_{1-x} for depositions at T = 190°C for CdTe on CdS (upper) and CdS on CdTe (lower)..... 29
Figure 4.20 The E_0 critical point energy plotted as a function of true temperature obtained during cooling of a CdTe film from the deposition temperature of 304°C to room temperature (15°C) (left). Also shown are the linear variations in critical point energies for the set of five CdTe films prepared at different temperatures (right). Results for single-crystal CdTe are shown in both panels for comparison..... 30
Figure 4.21 The E_0 critical point width Γ_0 plotted as a function of true temperature obtained during cooling of a CdTe film from the deposition temperature of 304°C to room temperature. 31
Figure 4.22 The E_0 critical point energy plotted as a function of true temperature obtained during cooling of a CdS film from near the deposition temperature of 320°C to near room temperature (25°C). 32

Figure 4.23 The E_0 critical point width Γ_0 plotted as a function of true temperature obtained during cooling of a CdS film from near the deposition temperature of 320°C to room temperature (15°C). 32
Figure 4.24 Dielectric functions measured at ~15°C for CdS films magnetron sputter-deposited at three different temperatures. 33
Figure 4.25 Second derivative spectra (open squares and circles) in ε for CdS deposited at T=160°C and measured at T~15°C 33
Figure 4.26 Broadening parameters measured at ~15°C for CdS films deposited at different T; the lowest broadening parameter values are circled. 34
Figure 4.27 (a) Schematic band diagram of a direct gap semiconductor (such as CdS) around the fundamental gap E_0; (b) Schematic semiclassical model for grain boundary scattering. 35
Figure 4.28 Grain size in CdS thin films estimated from the broadening parameter of the E_0 transition by using the inverted form of Equation (2). 36
Figure 4.29 Broadening parameters of the E_1-A and E_1-B CPs vs. inverse grain size. 36
Figure 4.30 Grain size as a function of deposition temperature for CdTe deduced from the E_2 transition widths. 38
Figure 4.31 Broadening parameters versus inverse grain size 1/R for the E_0, E_1, and $E_1+\Delta_1$ transitions of CdTe films prepared versus substrate temperature. 38
Figure 4.32 Room temperature (15°C) E_0 band gap for CdTe films obtained after a deposited thickness of 1000 Å, plotted as a function of the substrate temp-erature used in the deposition process. 39
Figure 4.33 Shifts in the room temperature E_1, $E_1+\Delta_1$, and E_2 critical point energies measured relative to the single crystal values for the series of CdTe films prepared at different substrate temperatures. 39
Figure 4.34 Stress in CdS films as a function of deposition temperature. 40
Figure 5.1 Change of energy efficiencies from the initial performance. 42
Figure 5.2 χ(R) functions of light soaked sample and Cu_2O reference. 43
Figure 5.3 Unit cell of Cu-Au alloy crystal 44
Figure 5.4 Theoretical fitting and experimental EXAFS data of complete cell structure. (a) fresh cell; (b) 2 days light soaked; (c) 5 days light soaked. 45
Figure 5.5 Cu-Au alloy layer in (001) direction: (a) Side view of the (001) plane, (b) top view of the (001) plane. Circled atoms are the Cu atoms in reference Cu-Au crystal which are substituted by Au atoms in our proposed model structure. 47
Figure 6.1 High resolution TEM image with point-to-point resolution 1.7 Å at the CdTe/Au interface. 50
Figure 6.2 Cross-section TEM image of CdTe and Au layer. Circles are the locations where the fine-probe EDS spectra were taken. 51
Figure 6.3 Fine-probe EDS spectra taken at locations indicated in Figure 6.2 52
Figure 7.1 Cell structure and meaning of front and back side illumination 54
Figure 7.2 J-V data for cells with 2.3 μm CdTe, illuminated from the front side. (a), with ZnO:Al as the n-type contact. (b), with ITO as the n-type contact. 55
Figure 7.3 Variation of ITO conductivity with deposition temperature. 56
Figure 7.4 J-V curves of CdTe/ZnTe:N/ITO cells using (a) low temperature and conductivity, (b) medium temperature and conductivity, and (c) high temperature and conductivity ITO. 56

Figure 7.5 J-V curves of cells with (a) 2.3 μm, (b) 1.8 μm, and (c) 0.7 μm CdTe, using front and back illumination. 58
Figure 7.6 Normalized generation rates for front and back side AM1.5 illumination in the case of (a) 2.3 μm (with schematic electric field), (b) 1.8 μm, and (c) 0.7 μm CdTe cells. 58
Figure 7.7 Relative intensity of 800, 650 and 500 nm light as a function of position within a 2.3 μm CdTe cell for front and back side illumination, with schematic electric field. 58
Figure 7.8 External Quantum Efficiency, measured with front and back side illumination, on (a) 2.3 μm, (b) 1.8 μm, and (b) 0.7 μm CdTe cells. 59
Figure 8.1 Deposition rate at 20 W of RF power as a function of argon pressure 61
Figure 8.2 Deposition rate in 5 mT Ar as a function of RF power (linear fit is shown). 61
Figure 8.3 Typical XRD spectra of as-deposited and $CdCl_2$-treated films 62
Figure 8.4 AFM images of CdTe films grown at 20W at 50 mTorr (left), 18 mTorr (middle) and 5 mTorr (right) 63
Figure 8.5 AFM images of CdTe films grown at 5 mTorr at 20 W (left), 40 W (middle) and 60 W (right). 63
Figure 8.6 Average efficiency vs. $CdCl_2$ treatment temperature of best 50% of cells deposited at four different conditions. 64
Figure 8.7 QE of the high-rate cells after $CdCl_2$ treatment at different temperatures 64
Figure 8.8 J-V curves of the best cells grown at different conditions: a) 18 mTorr, 20 W (UT standard), b) 9 mTorr, 6.6 W, c) 9 mTorr, 20 W, d) 9mTorr, 60 W (high rate) and $CdCl_2$ treated at four different temperatures. 65
Figure 9.1 IV curves of CdS/CdTe devices with and without pyrrole surface treatment Dot cells were 0.068 cm^2 of evaporated gold. 67
Figure 9.2 GIXRD pattern of a typical sample before light treatment 68
Figure 9.3 GIXRD pattern of a sample immediately after pyrrole light treatment and 72h after the treatment. 68
Figure 9.4 GIXRD sample immediately after aniline light treatment, 4h and 72h after the treatment 69
Figure 9.5 (a) SEM image of an as-deposited CdTe device. (b) SEM image of a sample after $CdCl_2$-Treatment. 69
Figure 9.6 (a) SEM image of a pyrrole light treated sample. (b) SEM image of an aniline light treated sample. 69

LIST OF TABLES

Table 2.1 CdTe, CdS, and $CdTe_{1-x}S_x$ deposition parameters. 2
Table 5.1 Cell efficiencies vs. light soaking time 42
Table 5.2 Theoretical fitting to EXAFS spectra of complete cell structure before and after light soaking. 46
Table 6.1 Comparison of Cu K_α and Mo K_α intensities. 52
Table 7.1 Summary of efficiency and second-order metrics for 2.3 μm CdTe cells. 55
Table 7.2 Summary of efficiency and second-order metrics for cells with ZnTe:N/ITO back contact. 57
Table 9.1 Best cell parameters of pyrrole treated (light), pyrrole treated (dark), aniline treated (light) and untreated cells..... 67

1. Introduction

1.1 Background

The purpose of this subcontract, as part of the R&D Partners, Solar Cell Optimizer Category is to 1) understand the mechanisms driving CdTe device performance and degradation; 2) experiment with raising the deposition rate of sputtered CdTe to make it more attractive economically; 3) investigate the limits of thickness reduction of CdTe using sputtering to reduce Te shortage issues and add to the economic attractiveness of the sputtering method; and 4) to support workforce development through the education and training of undergraduate, graduate, and postdoctoral students in the PV area.

This annual report covers the first year NREL thin-film partnership subcontract with the University of Toledo which has three task areas: 1) understanding key aspects of CdTe device physics, 2) increasing the deposition rate of CdTe magnetron sputtering, 3) investigation of the limits of reducing the thickness of CdTe layers to below 0.5 microns, with special focus on voltage and fill factor.

1.2. Objectives of this subcontract

The primary objectives of this research by this subcontractor as an R&D partner is to address fundamental issues especially related to:

- enhancing the total-area, thin-film cell efficiency through magnetron sputtering,
- improving the understanding of the materials and devices and growth processes through the use of spectroscopic ellipsometry (SE), photoluminescence (PL), Hall, Raman, absorption, scanning electron microscopy (SEM) with energy dispersive x-ray spectroscopy (EDS), and X-ray absorption fine structure (XAFS),
- identifying materials and structural issues that can lead to improved cell stability, including buffer and interfacial layers and novel back contacts,
- identifying novel device structures to find pathways for reducing utilization of CdTe,
- improving the understanding of nonuniformities and their impact on device and module performance through novel experiments and modeling, and
- strengthening the thin-film PV infrastructure through education and training of undergraduate and graduate students as well as postdoctoral associates.

1.3. Technical approach and annual report organization

The technical activities of Phase II are reviewed in this report in the following sequence:

- Real Time Spectroscopic Ellipsometry (RTSE) studies of nucleation and growth of CdS, CdTe, and CdSTe alloys are covered in Section 2, and RTSE of $CdCl_2$ treatment in Section 3.
- Optical modeling of CdS/CdTe cell structures is reported in Section 4.
- EXAFS studies of local bonding of Cu is covered in Section 5.
- High Resolution cross-sectional TEM studies of back contact regions in Section 6.
- Bifacial response of cells with transparent back contacts is reported in Section 7.
- Further studies of high growth rate sputtered CdTe is covered in Section 8.
- XRD and SEM studies of Pyrrole treatments for non-uniformities, Section 9
- Theoretical modeling of ultra-thin cells is summarized in Section 10 and covered more completely in the reprint of Appendix A.

2. Nucleation and Growth of CdTe, CdS, and CdS_xTe_{1-x}

2.1. Introduction

In situ, real time spectroscopic ellipsometry (RTSE) analyses of II-VI thin films are important because of the insights they provide into the structural evolution of the films and its potential influence on the ultimate photovoltaic properties, as well as into heterojunction formation. Such insights can be applied to control multi-step processing and to optimize interface, bulk, and surface properties separately for high performance cells. RTSE is being used in this project to obtain a better understanding of sputter deposition and $CdCl_2$ post-processing of CdS/CdTe solar cells. In the Phase I Annual Report, the evolution of the surface roughness and void structure in CdTe and CdS films prepared on smooth, native oxide-covered crystal Si wafer substrates at different deposition temperatures was described in detail. Here, the structural evolution in the early stage of growth is described with a focus on comparisons among CdTe, CdS, and the alloy system CdS_xTe_{1-x}. First the characteristics of the deposition processes will be presented with a focus on deposition rate, and then the nucleation behavior will be presented.

2.2. Experimental Details and Deposition Processes

The design principles of the rotating compensator multichannel ellipsometer used in this study are analogous to those developed earlier for studies of a-Si:H based solar cells.[1] The instrument provides ellipsometric spectra (ψ, Δ) over the spectral range from 0.75 to 6.5 eV. In this study, the spectra were acquired in times from 1 to 3 s, as averages over ~30 to 90 optical cycle pairs, during which ≤ 3 Å deposited material has accumulated. This provides sufficient thickness resolution for the characterization of the nucleation processes with monolayer resolution.

Polycrystalline CdTe, CdS, and $CdTe_{1-x}S_x$ films were magnetron sputtered under the conditions listed in Table 2.1, which are similar to those yielding efficient solar cells. Native oxide-covered crystalline Si wafers were used as substrates due to their consistent smoothness. The deposition temperature T, a key process variable, was determined from the E_0 band gap shifts that occur upon cooling the deposited film to 15°C and reheating to the deposition temperature T, as described later in this report. This temperature represents the true temperature averaged within the top ~1000 Å of the growing film/substrate.

Table 2.1 CdTe, CdS, and $CdTe_{1-x}S_x$ deposition parameters.

Deposited material	RF power (Watt)	Ar pressure (mTorr)	Ar flow (sccm)	Deposition temperature (°C)
CdTe	60	18	23	188-304
CdS	50	10	23	145-320
$CdTe_{1-x}S_x$	co-sputtering CdTe 20-75 CdS 33-53	18	23	190

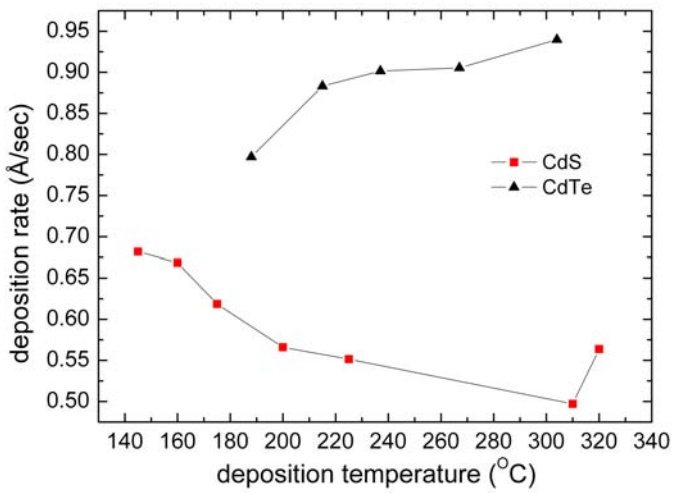

Figure 2.1 *Deposition rate as a function of substrate temperature for the CdTe and CdS series studied in detail in this report. For the CdTe, there is a significant variation in void fraction with substrate temperature that is used to correct the results and extract the true rate which is based on volume of material deposited per unit area. Such a correction is not needed for CdS due to the near constant void volume fraction of <0.02.*

A key deposition characteristic deduced from RTSE is the deposition rate. Figure 2.1 compares the deposition rate trend versus temperature for the series of CdTe and CdS films studied in this report whose deposition parameters are listed in Table 2.1. It is interesting that opposite trends are observed for CdTe and CdS; however, an uncontrolled parameter may exist as noted by the two different rates for the highest temperature CdS depositions. This is likely to be the rf power coupled into the target rather than parameters such as temperature, pressure, or gas flow. The results for CdTe have been corrected for an increase with temperature in the void volume fraction incorporated into the film that leads to an increase in thickness rate at constant atom incorporation rate. Such a correction is not needed for CdS since the void fraction is very low (<0.02, relative to the highest density film) for all samples independent of deposition temperature. The possible origin of the increase in rate with temperature for CdTe is a reduction in atom concentration in the sputtering gas with increasing gas temperature, but constant pressure. Such a reduction in gas concentration would lead to a reduction in the gas phase scattering of deposited species. Possibly this effect is not dominant in CdS (which shows opposite behavior) due to the lower pressure of CdS deposition (10 mTorr vs. 18 mTorr). The reduction in the deposition rate of CdS with increasing temperature may be due to a reduction in sticking coefficient of the incident growth species with increasing temperature. It is not clear, however, why this is also not a dominant effect in CdTe, as well.

Table 2.2 Target power levels used in the fabrication of CdS_xTe_{1-x} by co-sputtering along with the predicted molar fraction of S.

Sample #	CdS target power (W)	CdTe target power (W)	*x*
1	0	36	0
10	33	75	0.10
11	33	43	0.19
9	36	36	0.28
12	35	30	0.39

Sample #	CdS target power (W)	CdTe target power (W)	*x*
13	60	30	0.59
18	40	25	0.72
14	60	25	0.82
15	53	20	0.89
3	36	0	1

The CdS_xTe_{1-x} alloys were deposited at T=190°C, which is close to the highest temperature possible without phase segregation.[2] The key variable x was determined on the basis of RTSE calibration of the individual CdTe and CdS deposition rates versus target rf power. Figure 2.2 shows the dependence of deposition rate on rf power for the CdTe and CdS targets. The adopted rf powers and the corresponding expected x values are shown in
Table 2.2.

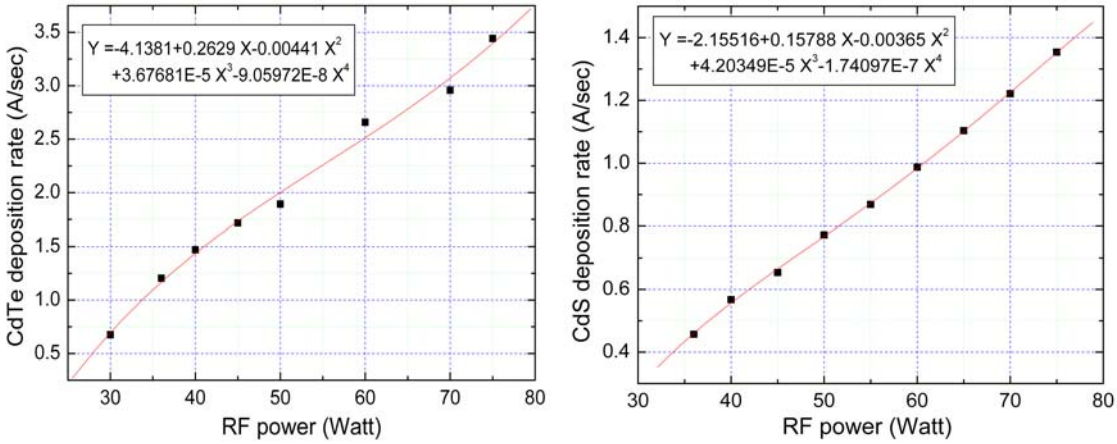

Figure 2.2 *The calibration of CdTe and CdS deposition rates as functions of target RF power. All other deposition parameters are held constant: T = 190°C, Ar pressure = 18 mTorr, and Ar flow = 23 sccm. The solid lines are fourth order polynomial fits to the data that allow one to interpolate the rate from any rf power between the data value extremes and, thus, the molar fraction for any pair of power levels in co-sputtering (assuming non-interacting CdTe and CdS deposition processes). For extrapolation, linear fitting of data was performed over restricted ranges.*

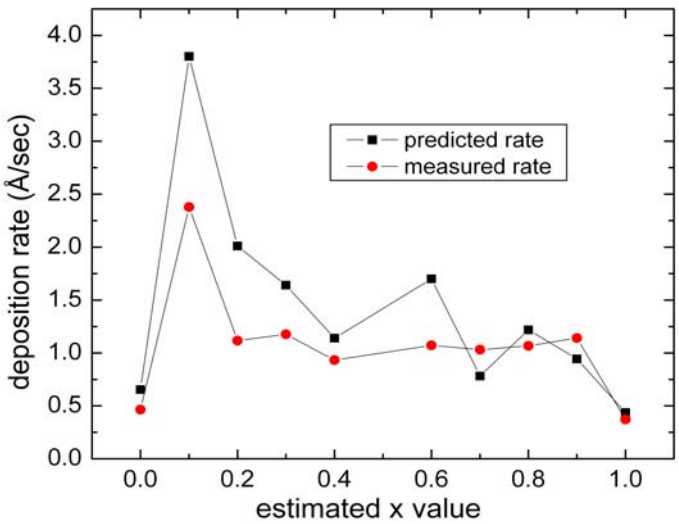

Figure 2.3 *Measured deposition rate versus composition for ~200 Å thick CdS_xTe_{1-x} alloys. Also shown is the predicted rate based on the addition of the individual rates from the calibration curves of Figure 2.2. The difference may be attributed to plasma stabilization on the time scale of minutes and to plasma "crosstalk" at high power levels.*

The measured deposition rates versus x for the CdS_xTe_{1-x} are shown in Figure 2.3. One point to notice is that over a wide range of x from 0.2 to 0.9, the deposition rate is nearly constant. This makes it easier to relate trends in optical properties and structural evolution over this range to composition rather than to rate deviations. A problem encountered, however, is highlighted in Figure 2.3 -- namely that the measured deposition rate for the alloys can be significantly different than the predicted rate based on the calibrations of Figure 2.2. This effect may be attributed to two possible causes. The first is previously unrecognized plasma stabilization on the time scale of 10 min or more during which the rate increases with time at fixed plasma power. This behavior occurs more strongly for the CdTe process than for the CdS process, as indicated by the non-linear calibration curve for the former. The measured rates for the alloy process are obtained in the first three minutes after opening the shutter for presputtering whereas the individual processes that yield the calibration data of Figure 2.2 are obtained as a function of time from low to high power over ~40 min without extinguishing the plasma. As a result, one can understand why the predicted rate is higher than the measured rate for high CdTe plasma power levels (low x) and lower than the predicted power for low power levels (high x). A second cause of the deviation in Figure 2.3 may be plasma interference in which case the plasma may expand into the region between the sputter sources when both are operating. Such an effect seems possible based on the observation of slow deposition occurring during presputtering when both sputtering sources are operated -- even with shutters blocking the targets. Such deposition is not observed during presputtering when each source is operated separately. Apparently, the errors in x generated by the two effects give rise to non-monotonic behavior for some samples -- most notably for $x = 0.28$.

2.3. Nucleation of CdTe and CdS

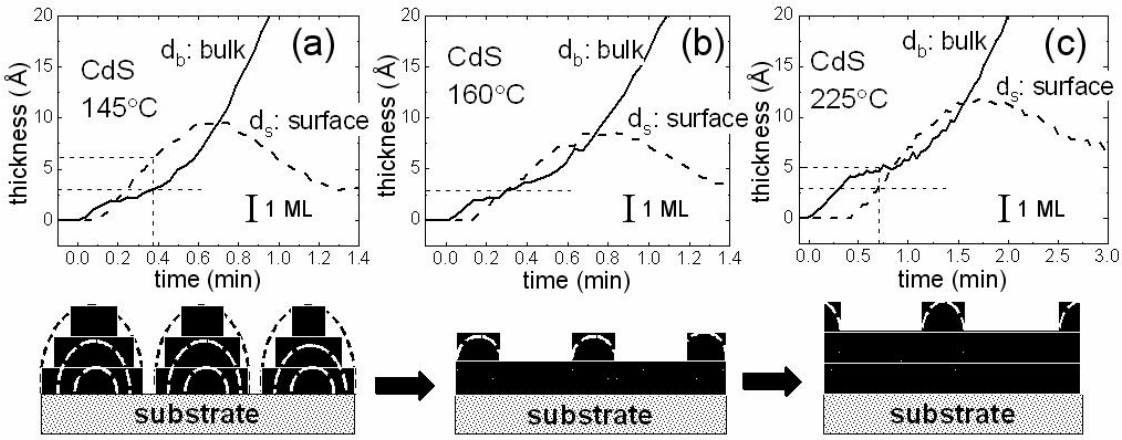

Figure 2.4 *Nucleation modes of CdS thin films deposited at different temperatures: (a) 145 ℃; (b) 160 ℃; (c) 225 ℃.*

In analyses of RTSE data in the initial stages of the deposition, a model for the film was used consisting of two layers, (i) a dense layer of thickness d_b with a bulk-like dielectric function and (ii) a surface roughness layer of thickness d_s with a dielectric function determined from the Bruggeman effective medium theory as a 0.5/0.5 volume fraction mixture of (bulk material)/void.[3] Figure 2.4 shows the time evolution of d_b and d_s for CdS deposition at three temperatures; qualitatively similar results are obtained for CdTe. At T=145°C in Figure 2.4, a

~6 Å thick roughness layer appears before the first dense monolayer (ML) (~3 Å), as shown in Figure 2.4(a). This is typical of the island or Volmer-Weber (V-W) nucleation mode. In contrast, at T=225°C, ~1-2 dense MLs appear before the first ML of roughness, as shown in Figure 2.4(c). This is typical of the layer-to-island or Stranski-Krastanov (S-K) growth mode. At T=160 °C, the first MLs of surface roughness and dense material appear virtually simultaneously, as shown in Figure 2.4(b). This temperature describes a transition from V-W to S-K type modes. At higher T, a layer-by-layer mode is favored for both CdTe and CdS due to a reduction in free energy density of the interface relative to that of the surface possibly as a result of enhanced diffusion at higher T.

Figure 2.5(a) shows the two ways to determine the V-W to S-K transition temperature (vertical lines), either (i) as the temperature at which the surface roughness layer thickness (d_s) drops below a single monolayer at the bulk monolayer thickness (d_b ~ 3 Å) (top panel) or (ii) as the temperature at which the bulk layer thickness (d_b) increases above one monolayer for a surface roughness layer thickness of a single monolayer (d_s ~ 3 Å) (bottom panel). The trends versus temperature in Figure 2.5(a) are systematic and reveal the high sensitivity of the methods for extracting the transition temperatures. The resulting values are ~160°C for CdS and ~260°C for CdTe, values which are likely to reflect the kinetics of bonding at the interface. The peak nuclei height for CdTe is larger than that for CdS as observed in Figure 2.5(b), indicating a lower nuclei density in the initial stages. In both cases, the nucleation density decreases with increasing deposition temperature, most likely due to activated diffusion processes. Different nucleation behavior in the initial stage of deposition has been observed to impact the subsequent structural evolution of film and ultimate material properties, as has been discussed in the Phase I Annual Report.

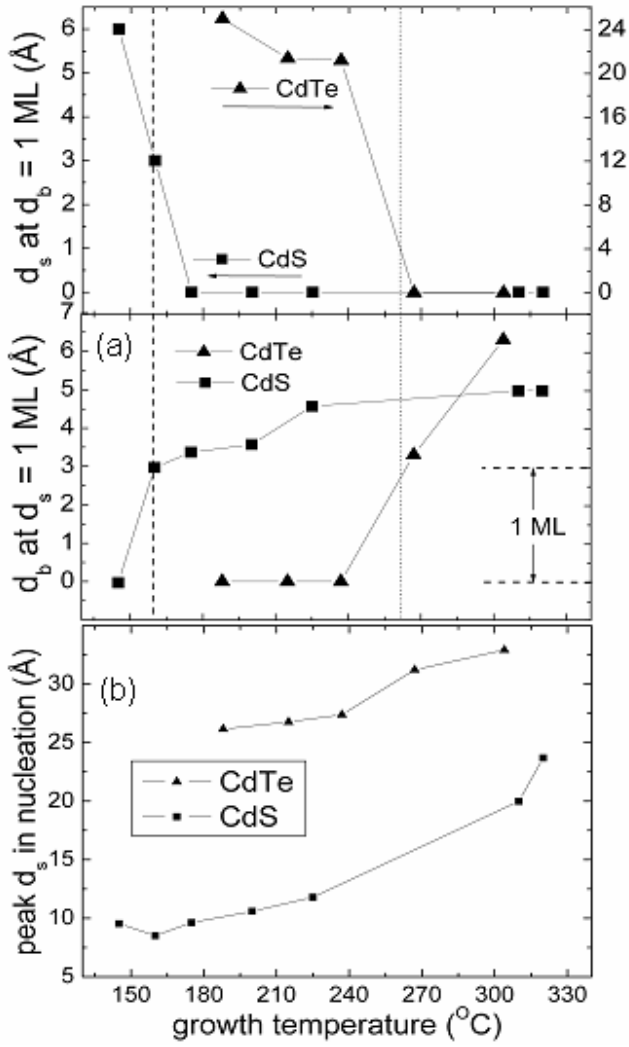

Figure 2.5 *(a: top two panels) Key nucleation parameters: d_s when the first complete dense ML appears (upper panel); d_b when the first surface roughness monolayer formed (center panel); peak nucleation height before coalescence (b: lower panel).*

2.4. Nucleation of CdS_xTe_{1-x}

Considering next the nucleation characteristics in Figure 2.6, all alloys show island-layer growth mode (Volmer-Weber mode) at the beginning of deposition regardless of the x value. In addition, they all have similar surface roughness thickness values, d_s = 21.5±1.5 Å, when the first bulk monolayer appears (d_b = 3 Å). Up to this point, the film growth pattern is nearly the same among all alloys. However, the peak amplitude in the nucleating layer thickness (occurring at bulk layer thicknesses from d_b=10 to 25 Å), the roughness after coalescence, and the roughening rate near the end of deposition vary consistently with x. First, the overall roughness amplitude decreases upon addition of S to CdTe considering the nucleation and coalescence regime. For $CdS_{0.28}Te_{0.72}$, the surface is very smooth and stable for the first 200 Å of bulk layer growth -- considerably smoother than pure CdTe. In contrast, the addition of Te to CdS leads to an increase in the roughness amplitude in this regime. For $CdS_{0.59}Te_{0.41}$, the surface is very rough -- considerably rougher than pure CdS even after coalescence, and the roughness is increasing rapidly after 100 Å of bulk layer growth. Because increased surface roughness amplitude has been found to be associated with increased compressive stress as indicated by the blue shift of the band gap relative to the single crystal, then the smoothening with S addition to CdTe is possibly due to the relaxation of compressive stress due to the smaller atomic radius of S relative to Te. Similarly, the enhancement of roughness with addition of Te to CdS may be due to the generation of an additional compressive stress component due to the larger atomic radius of Te. In the composition range between x=0.3 and x=0.6, there is an abrupt transition from the CdTe-rich smooth surface to the CdS-rich rough surface. This roughening between x=0.3 and x=0.6 possibly represents the phase transition from more relaxed cubic CdTe to compressively stressed hexagonal CdS. Additional discussion of the stress in the binary compounds will appear later in this report.

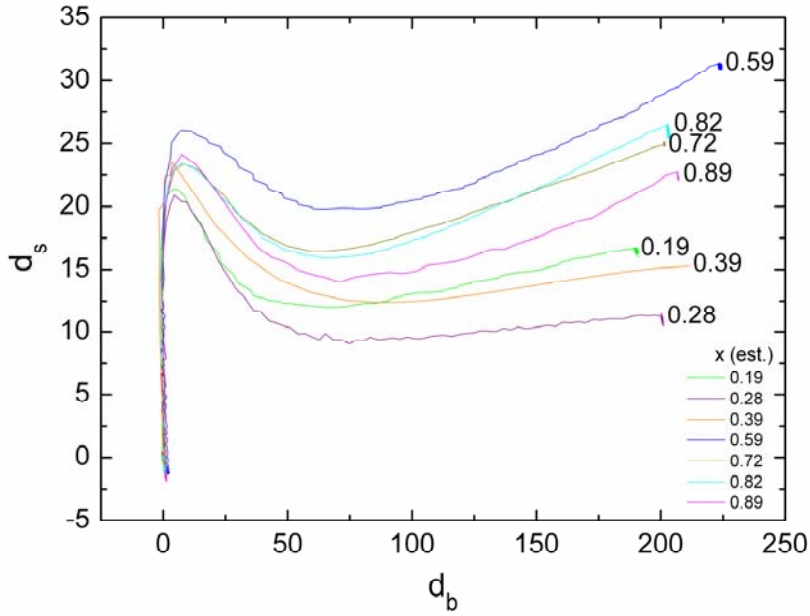

Figure 2.6 *Nucleation and surface roughness evolution characteristics of CdS_xTe_{1-x} alloy deposition on c-Si wafer substrates at a deposition temperature of 190°C. In this plot, d_s is the surface roughness layer thickness and d_b is the bulk layer thickness. The deposition rates of these alloys are similar: 1.05 ± 0.15 Å/s (see Figure 2.3).*

3. $CdCl_2$ Treatment of CdTe

Another focus of SE research is to probe the effects of post-deposition processing on the properties of II-VI films and device structures deposited by magnetron sputtering. These studies start with CdTe on native oxide-covered c-Si substrates to avoid the complication of alloying effects that would occur with a heterojunction, and then progress to solar cells (without the back contact). The experiment to be described first applies the etch-back method to ~3000 Å thick CdTe films co-deposited on c-Si substrates held at 188°C. Co-deposited films were exposed to the following post-deposition processing conditions: (i) as-deposited (i.e., no treatments), (ii) annealed in Ar at 387°C for 30 min, and (iii) $CdCl_2$ treated also at 387°C, but for 5 min. The new work completed here was to explore the effect of $CdCl_2$ treatment procedure on the film properties. For each sample prepared here, the etch-back method was performed using successive immersion steps in Br_2+methanol, with each etch step leading to a ~300 Å reduction in the bulk layer thickness. Because of the relative smoothness of the as-deposited CdTe films (compared, for example, to films on TEC glasses), the successive etching treatments lead to very smooth surfaces from which accurate dielectric functions can be determined in depth-profile. In addition, the absence of an underlying CdS film in this case avoids potential complication of alloying of CdTe due to S in-diffusion.

Figure 3.1 presents an overview of previous work in which depth profiles in the E_1 critical point energy and width relative to those of the single crystal provide information on the depth profiles in the strain and grain size, respectively, throughout the film. New results presented in this report suggest that the E_1 transition shifts to lower energy with increasing strain consistent with a stress shift of (–0.2 eV/GPa). With these new insights, the depth profiles in the critical point energies take on greater meaning. Similarly, Figure 3.2presents depth profiles in the void fraction that provide information on the structural uniformity.

- For the *as-deposited film*, the red-shift of E_1 relative to the single crystal value in the top panel of Figure 3.1 suggests significant strain in this film over the studied depth range of 1500-2000 Å; (the depth is measured relative to the substrate interface at 0 Å). The maximum E_1 energy shift of –0.12 eV at a depth of 1500 Å converts to a stress level of 0.6 GPa, which is consistent with results for these as-deposited films to be presented later in this report. The depth profile in Figure 3.2 provides additional indirect evidence for this strain; the film is observed to undergo a structural transition near 1500 Å whereby the strain is ultimately relaxed (after 2000 Å thickness) through generation of voids and their continued evolution with thickness. The lower panel of Figure 3.1 shows that the as-deposited film has a very large broadening parameter $\Gamma_{E1} \sim 0.6 \pm 0.15$ eV, indicative of a very small grain size (~ 10 nm), also described later in this report.
- Upon *Ar annealing of the film*, the strain nearest the substrate is significantly reduced as the grain size increases (reduced Γ_{E1}). Even after 30 min of annealing in Ar, however, there is no significant reduction in the grain size within 500 Å of the surface, and the strain in this region increases somewhat relative to the as-deposited film (as indicated by the lower E_1 energy). Figure 3.2 shows that the void fraction in the surface region is reduced upon annealing in Ar and thus, the structure of the film becomes more uniform throughout the thickness.
- A *5 min $CdCl_2$ treatment* leads to an E_1 energy within 10 meV (i.e., within experimental error) of the single crystal value throughout the thickness, suggesting a fully strain-relaxed film.

In addition, Γ_{E1} has been reduced significantly to a constant value of $\Gamma_{E1} \sim 0.30 \pm 0.02$ eV throughout the bulk of the film, indicating a significant increase in grain size. Finally the $CdCl_2$

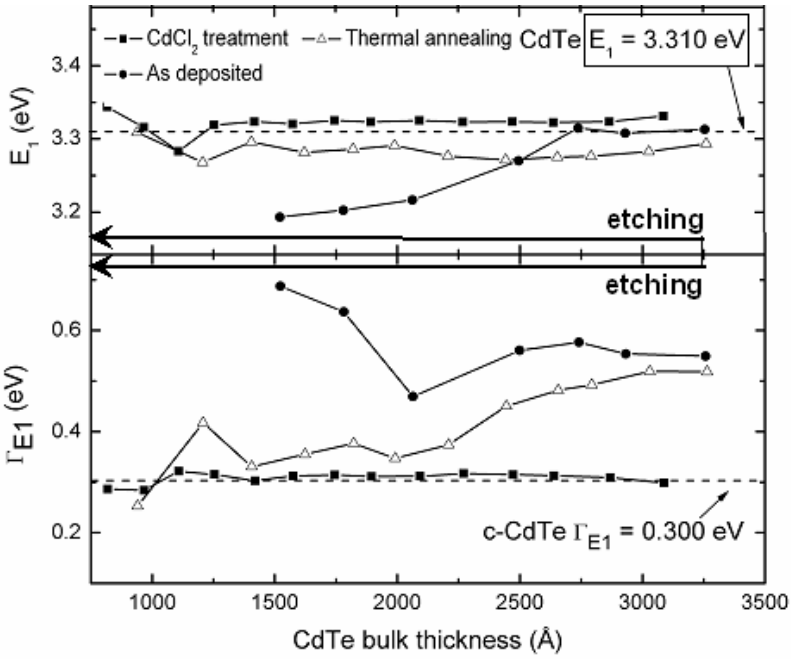

Figure 3.1 *Critical point energies (upper panel) and widths (lower panel) as functions of CdTe bulk layer thickness during etching by Br_2+methanol for co-deposited CdTe films processed in three different ways: (i) as-deposited, (ii) annealed in Ar for 30 min, and (iii) $CdCl_2$ treated for 5 min. The deviations at low thickness are due to the onset of semi-transparency for the E_1 critical point energy.*

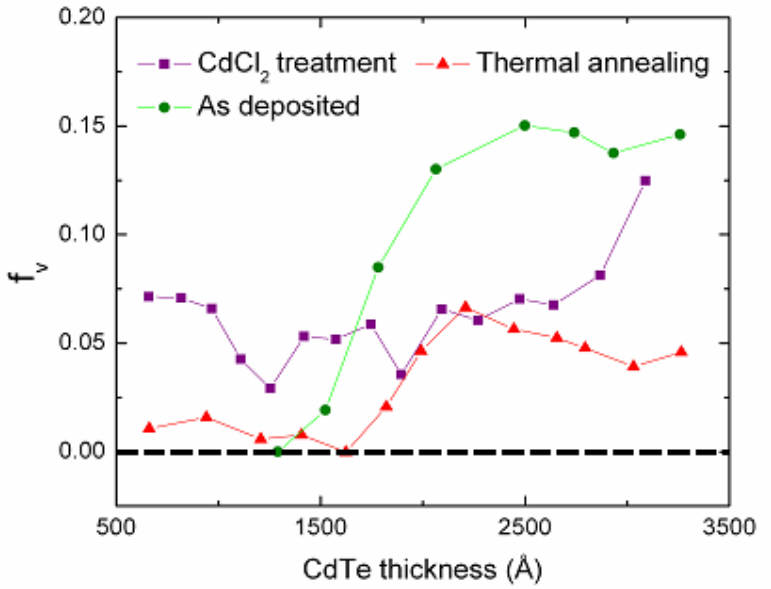

Figure 3.2 *Relative void volume fractions as functions of CdTe bulk layer thickness during etching by Br_2+methanol for co-deposited CdTe films processed in three different ways: (i) as-deposited, (ii) thermally annealed for 30 min, and (iii) $CdCl_2$-treated for 5 min. For the as deposited and annealed films, the void fraction is scaled relative to the depth at which the highest density is observed. For the $CdCl_2$-treated film, the void volume fraction is scaled relative to single crystal CdTe.*

treatment leads to a uniform void volume fraction throughout most of the bulk of the film 0.05 ± 0.02; however, considerable scatter exist in the data, possibly an effect of the Br_2+methanol etching of a large-grained, relatively thin film. Figure 3.2 shows that voids have been pushed to the near-surface region of the $CdCl_2$ treated film which is likely to be the result of a much larger surface roughness layer thickness. Finally, it should be noted that the void fractions for the as-deposited and Ar annealed films in Figure 3.2 are plotted relative to that of the as-deposited film at the minimum thickness of ~1250 Å. For this material, which is under significant compressive stress (0.6 GPa), the apparent density is ~0.03 higher than that of single crystal CdTe. For the $CdCl_2$ treated film, the void fraction is scaled relative to the single crystal.

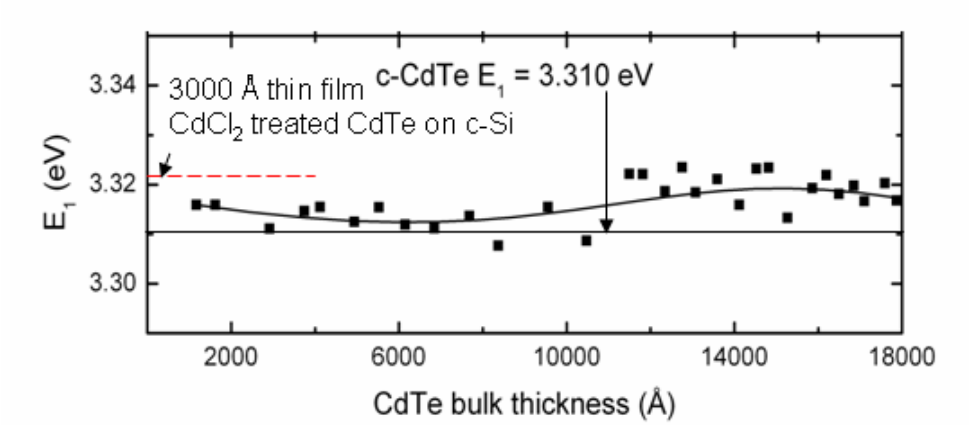

Figure 3.3 *Energy of the E_1 transition as a function of CdTe bulk layer thickness in successive Br_2-methanol etching steps for a sputtered CdTe solar cell. Also shown is the constant energy of the E_1 transition of thin film CdTe (3300 Å thick) fabricated on a c-Si wafer substrate.*

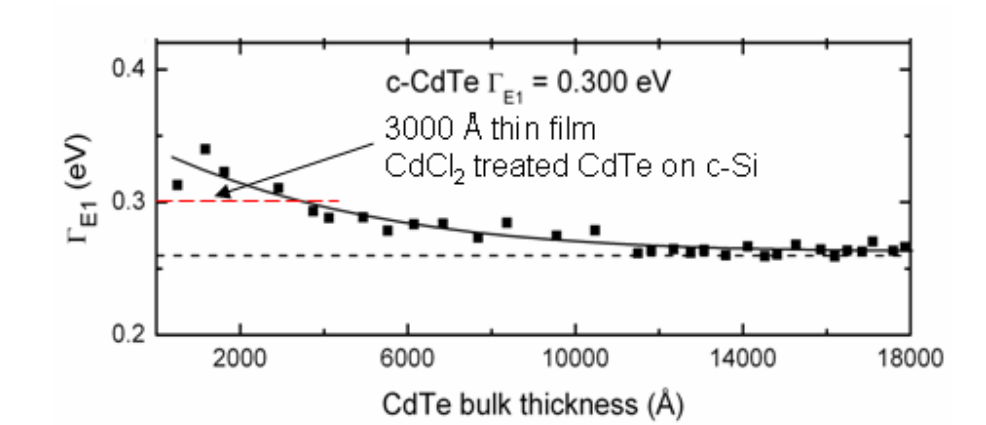

Figure 3.4 *Broadening parameter Γ_{E1} as a function of CdTe bulk layer thickness in successive Br_2-methanol etching steps for a sputtered CdTe solar cell. Also shown is the constant width of the E_1 transition of thin film CdTe (3300 Å thick) fabricated on a c-Si wafer substrate.*

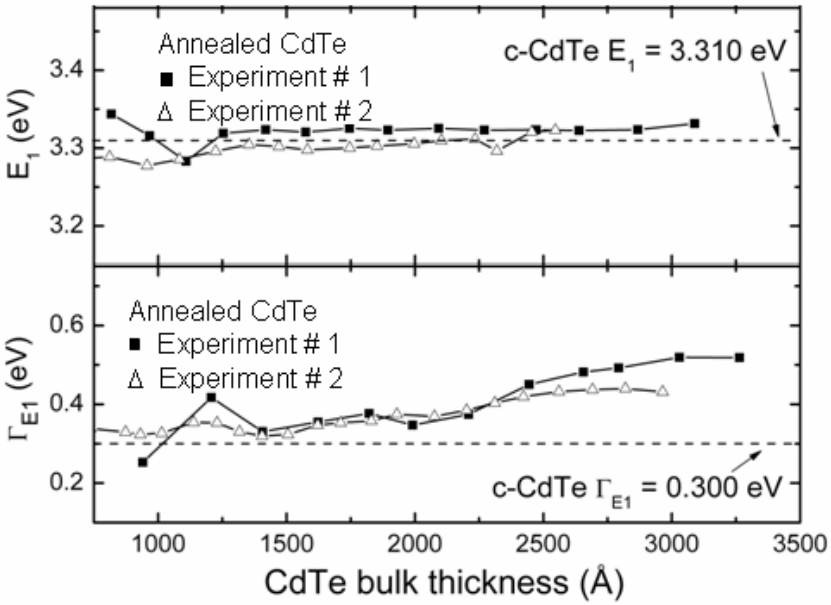

Figure 3.5 *Energy of the E_1 transition (upper panel) and its width Γ_{E1} (lower panel) as functions of CdTe bulk layer thickness in successive Br_2-methanol etching steps for ~3000 Å thick CdTe films. The two films were processed under identical conditions including fabrication on c-Si wafer substrates and anneals in Ar at 387°C for 30 minutes. The data for experiment #1 are the same as those depicted in Figure 3.1.*

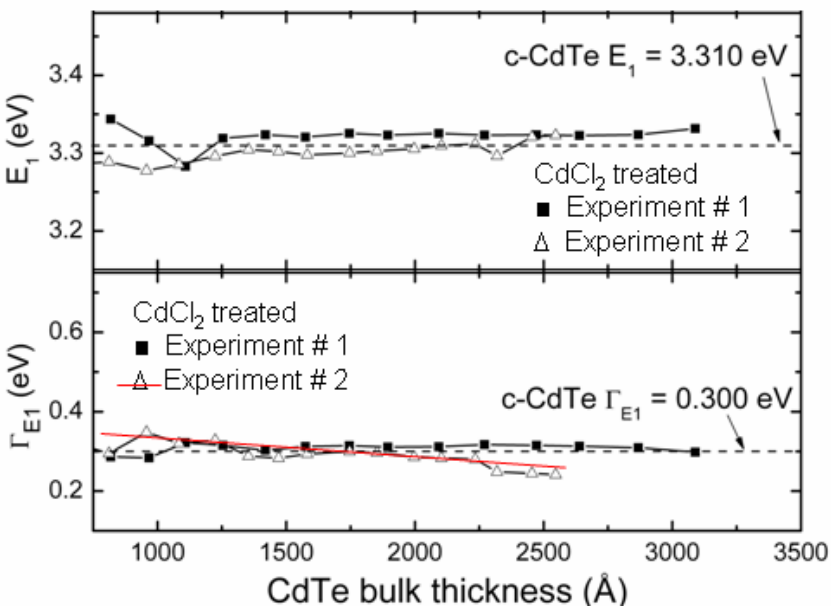

Figure 3.6 *Energy of the E_1 transition (upper panel) and its width Γ_{E1} (lower panel) as functions of CdTe bulk layer thickness in successive Br_2-methanol etching steps for ~3000 Å thick CdTe films. The two films were processed under similar conditions including fabrication on c-Si wafer substrates and $CdCl_2$ treatments for 5 minutes. The data for experiment #1 are the same as those depicted in Figure 3.1.*

Results of similar studies of solar cell structures on TEC-15 glass are shown in Figure 3.3 and Figure 3.4. The solar cells are complete, including $CdCl_2$ treatment, but with the exception of the back contact, and the SE measurements are performed from the film side during etch back. Figure 3.3 shows the E_1 energy of the CdTe layer on a scale that is expanded by a factor of 4 about the single crystal value relative to that of Figure 3.1. This energy remains within ±5 meV of the single crystal value from 1000 Å to 1.8 μm, indicating stress relaxation throughout the thickness. The results in Figure 3.4 for the E_1 critical point width Γ_{E1} reveal two important points. First because the value $\Gamma_{E1} \sim 0.26 \pm 0.01$ eV at the film surface side is less than that of single crystal CdTe, it suggests more careful measurements of the single crystal are needed. It is likely that surface scattering in the epitaxially grown single crystal is the origin of the larger Γ_{E1} value.[4] Second, the gradual increase in Γ_{E1} as the interface to the CdS is approached indicates that the grain size is decreasing toward this interface and that the grain structure in the cell is not as uniform as for the thin films on c-Si.

In further experiments, the reproducibility of the etch-back studies of films annealed in Ar has been explored, and the effect of the $CdCl_2$ treatment condition on film structure has also been investigated.

Figure 3.5 shows the Ar annealing behavior of thin (3000-3300 Å) CdTe films on c-Si substrates from two separate experiments for comparison. The solid squares are the same results as shown in Figure 3.1, and the open triangles are the results of a second experiment performed on a different sample prepared and annealed under identical conditions. The annealing behavior is reasonably well reproduced in the two experiments, considering that the film thickness in the second experiment is somewhat lower. In both experiments, the E_1 energy lies ~ 20 meV lower than that of single crystal CdTe, indicating residual strain of ~0.1 GPa, and the width Γ_{E1} increases toward the surface, indicating a smaller near-surface grain size in both experiments.

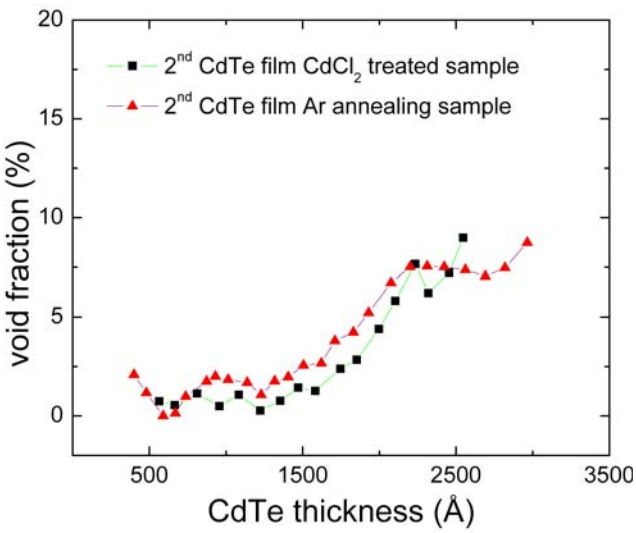

Figure 3.7 *Void volume fraction as a function of CdTe bulk layer thickness in successive Br_2-methanol etching steps for ~3000 Å thick CdTe films in a second experiment for comparison with the results in Figure 3.2. Two different post-deposition processing procedures were used: (i) anneal in Ar for 30 min, and (ii) $CdCl_2$-treatment for 5 min. For the Ar annealed films, the void fraction is scaled relative to the depth at which the highest density is observed. For the $CdCl_2$-treated film, the void volume fraction is scaled relative to single crystal CdTe. The void structure for the film annealed in Ar is attributed to structure in the as-deposited film (as in Figure 3.2). In contrast, the void structure for the $CdCl_2$ treated film is attributed to extensive near-surface roughness.*

Figure 3.5 shows results for E_1 and Γ_{E1} from two experiments applying $CdCl_2$ treatments for 5 min. The results of the first experiment have been presented earlier in Figure 3.1. This first experiment was performed with a $CdCl_2$ treatment temperature of 387°C, whereas the second was performed using a higher temperature of 397°C. Another difference between the

two experiments -- the age of the prepared $CdCl_2$ sources -- was deemed insignificant. More importantly, for both experiments, the treatment was the starting one for each of the two sources. Although the overall results of the two experiments are similar, certain details in the second experiment appear to reveal the effect of the higher temperature. First, for the second experiment, the grain size increases more significantly toward the surface than in the first experiment. In addition, a comparison of Figure 3.7 with Figure 3.2 shows that the void profile in the second experiment is not nearly as uniform as in the first. This feature is likely due the higher temperature which leads to a densification of the underlying large grain crystalline material at the expense of significant roughness that extends well into the film. A hint of this effect appears for the $CdCl_2$ treated film in Figure 3.2, but the effect appears quite strongly in Figure 3.7. In the future, complete studies of the effect of $CdCl_2$ treatment time and temperature will be undertaken.

4. Modeling Solar Cell Structures

There are three goals of optical analysis of complete CdTe solar cell structures. The first goal is to achieve a better understanding of the processing-property relationships so that the cells can be designed rationally for higher efficiency. The second goal is to establish the methodology required to extract the maximum possible information when SE is applied as a spatially resolved mapping tool on the CdTe solar cell production line. The third goal is to obtain insights into the quantum efficiency as well as the optical losses that limit the short-circuit current. Spectroscopic ellipsometry (SE) is a powerful optical probe; however, the CdTe solar cell poses considerable challenges for analysis by ex situ SE. First, the relatively large thickness of the as-deposited CdTe layer leads to considerable surface roughness, and the usual $CdCl_2$ post-deposition treatment generates significant additional oxidation and surface inhomogeneity. Thus, ex situ SE measurements in reflection from the free CdTe surface (prior to back contact formation) can be very difficult. Second, SE from the glass side of the cell is adversely affected by the top glass surface which generates incoherent reflections and consequent depolarization. In this research, these problems are solved through the use of Br_2+methanol treatments that smoothen the CdTe free surface and a 60° prism optically-contacted to the top glass surface that eliminates the top surface reflections. Figure 4.1 shows the optical geometry that is anticipated for such a mapping instrument. Focusing optics are needed in order to avoid collecting the top surface reflection from the glass substrate which is not of interest. In addition, this beam is incoherent relative to the light beam of interest which is the one reflected at the interface between the coated glass and the solar cell.

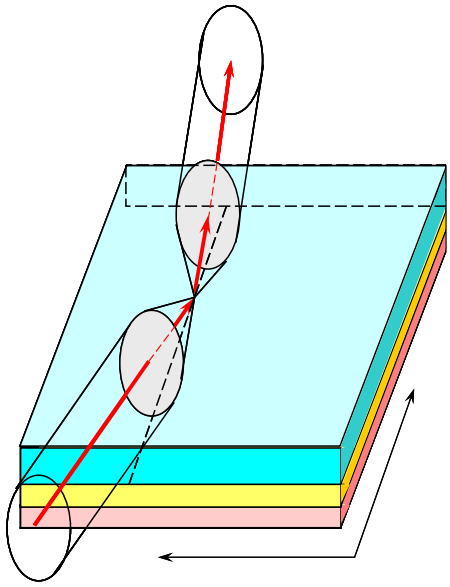

Figure 4.1 *Mapping SE configuration with focusing optics to collect reflection from the (TEC glass)/(solar cell) interface.*

4.1. Component Optical Properties

Before multilayer optical analysis can be applied to the CdTe solar cell, a library of dielectric functions $\varepsilon = \varepsilon_1 + i\varepsilon_2$ is needed that includes all the component layers, including the multilayer coating of the TEC-15 substrate. In fact, the TEC-15 is the most challenging problem since only a single measurement (as opposed to a real time measurement) is possible and there are three unknown layers and a substrate. Figure 4.2 shows the optical properties

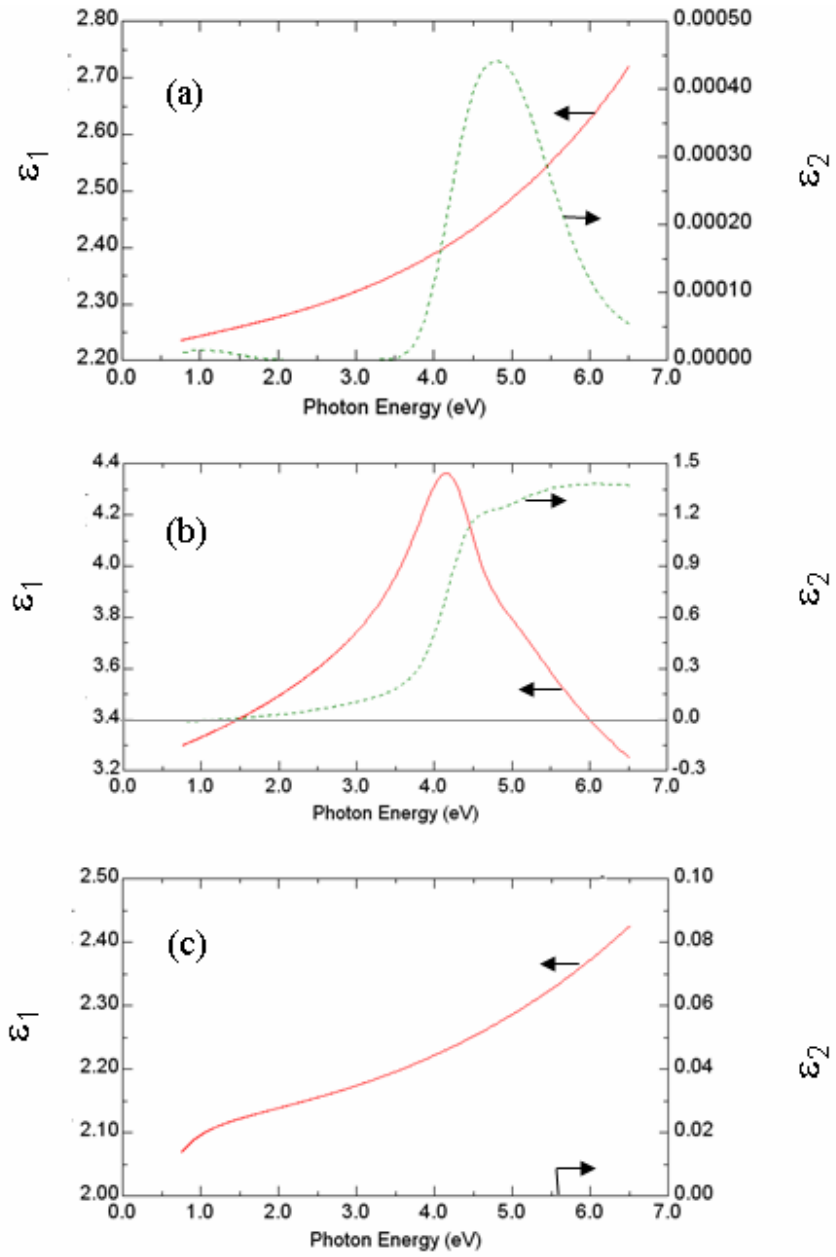

Figure 4.2 *Optical properties expressed in terms of the dielectric function of three of the four components of TEC-15 glass including (a) the soda lime glass substrate, (b) the near-substrate undoped SnO_2, and (c) the SiO_2 interlayer. Results for the topmost layer is shown in Figure 3.2.*

deduced in this study (expressed in terms of the dielectric function) for three of the four components of the TEC-15 glass. Results from top to bottom are included for: (a) the soda lime glass substrate, (b) the ~300 Å thick near-substrate undoped SnO_2, and (c) the ~ 200 Å thick SiO_2 interlayer. Results for the ~3500 Å topmost doped SnO_2:F layer are shown separately in Figures 4.3 and 4.4. In the analysis of this structure, ex situ transmission data along with SE data are employed, and this provides the ability to accurately measure weak absorption in the top SnO_2:F, which has an impact on quantum efficiency of the solar cell due to its greater thickness. Figure 4.4Figure 4.4 shows the optical data for the top SnO_2:F layer expressed in terms of index of refraction *n* and extinction coefficient *k*, such that *k* is plotted on a logarithmic scale to emphasize the weak absorption.

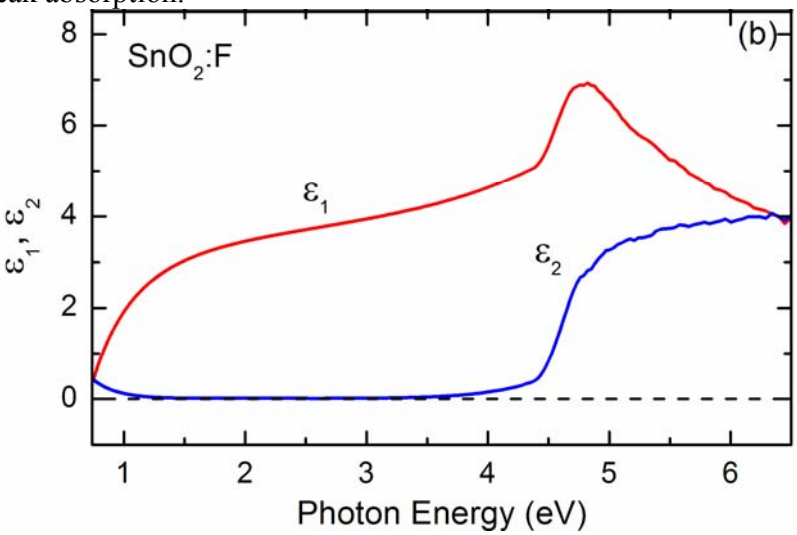

Figure 4.3 *Dielectric functions of SnO_2:F, the top-most layer of the TEC-15 substrate deduced in the analysis that includes a fit to the ellipsometric angles (Ψ, Δ) and the transmittance T. For photon energies above 5 eV, the SnO_2:F is opaque, and the optical properties are extracted from (Ψ, Δ) via inversion, correcting for surface roughness.*

Figure 4.5 depicts a comparison of best fit analytical models for the dielectric functions of untreated thin film CdTe, optimally $CdCl_2$ treated thin film CdTe, as well as single crystal CdTe, all obtained from measurements performed at room temperature. The untreated sample selected is a 1000 Å film prepared at the lowest temperature of T=188°C in Table 2.1. For this film, the growth process was tracked by RTSE, which provided accurate values of bulk layer and surface roughness layer thicknesses, so that upon cooling the film to room temperature, the dielectric function could be determined by exact numerical inversion. By measuring the sample after deposition and cooling but still under vacuum, oxides and surface contamination which influence the measured optical properties are avoided. The T=188°C deposition was selected because it exhibited the lowest void volume fraction among the samples of the temperature series, and a thin film was selected to avoid the microstructural transition (and associated void development) that occurs in the low temperature depositions near 1300 Å. For the treated sample, a thicker film (~3000 Å) deposited at the same temperature was used after exposure to $CdCl_2$ vapor at 387°C for 5 min (a shorter time than for solar cells due to the thin layer). Prior to measurement, this sample was exposed to several Br_2-methanol treatments to eliminate the surface oxide and smoothen the surface, as well as to match the thickness at which the as-deposited film was measured (~1000 Å). Although a correction for residual surface roughness

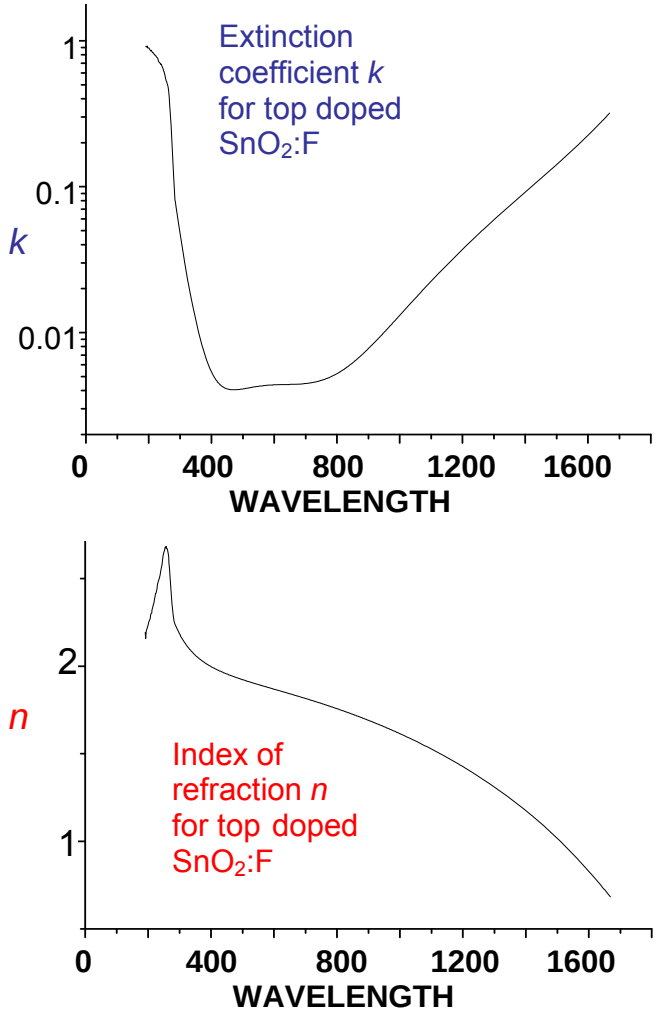

Figure 4.4 *Index of refraction and extinction coefficient of SnO_2:F, the top-most layer of the TEC-15 substrate deduced in the analysis that includes a fit to the ellipsometric angles (Ψ, Δ) and the transmittance T. The extinction coefficient is plotted on a logarithmic scale to emphasize the weak absorption.*

was made, there was no attempt to correct for any Te-rich layer at the surface. The results for the crystalline CdTe were obtained from a database of single crystal layers grown by molecular beam homoepitaxy.[4] All measured dielectric functions were fit using the same model which included four critical points (E_0, E_1, $E_1+\Delta_1$, E_2) as well as one broad background oscillator to simulate transitions not associated with the citical points.[5] Each critical point is characterized by five parameters, an energy gap, amplitude, broadening, phase, and exponent. The broad background is based on a simple Lorentz oscillator with an imposed band gap. In this case, there are five parameters including the gap, amplitude, resonance energy, broadening, and constant dielectric function contribution. Thus, with this method, it is possible to vary 25 parameters in the fitting. To reduce this number, the four critical point exponents are fixed to physically reasonable values, the resonance energy and gap of the broad background are fixed, and the same fixed values are used for all samples. This approach led to a total of 20 fitted parameters.

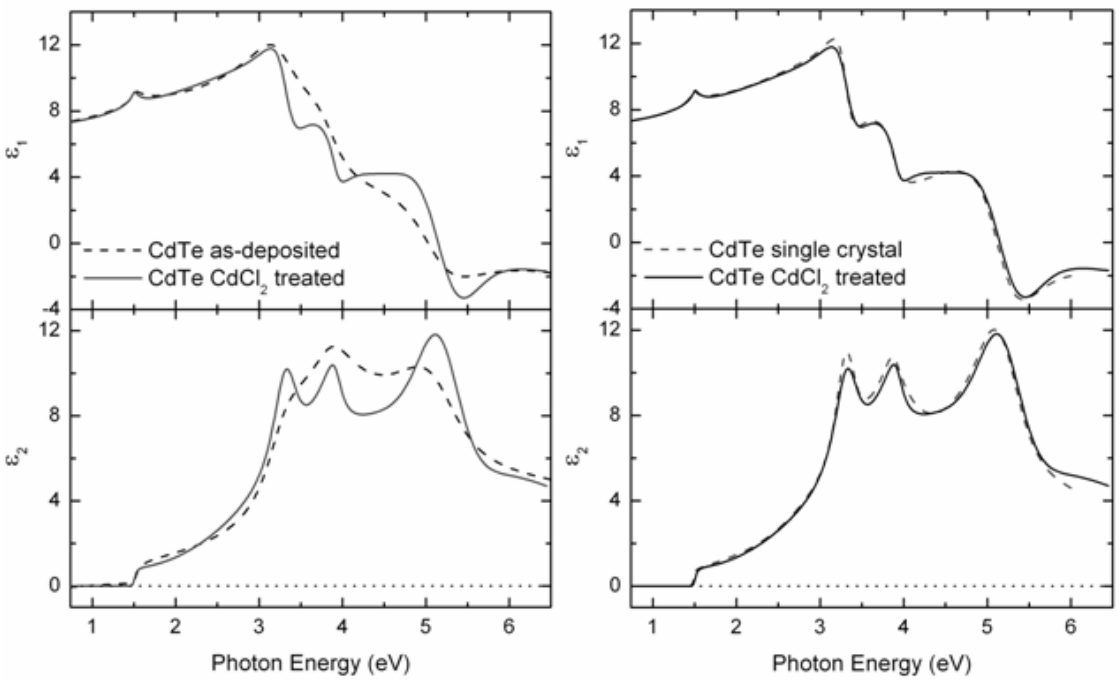

Figure 4.5 *(left) Best fit analytical models of the room temperature dielectric functions for two CdTe films of thickness ~ 1000 Å, obtained from the same deposition but with different post-processing as-deposited (no treatments; broken line) and $CdCl_2$-treated for 5 min at 387°C (solid line); (right) a comparison between the $CdCl_2$-treated CdTe film (solid line) and single crystal CdTe (broken line).*

The results in Figure 4.5 show that the as-deposited film has significantly broader critical points than the $CdCl_2$ treated film and that the $CdCl_2$ treated film has a dielectric function closely matching that of single crystal CdTe. The fact that the real parts of the dielectric function at energies below the band gap for the treated and single crystal CdTe closely match suggest that there is no significant density deficit throughout the entire ~3000 Å thickness of the treated film relative to the single crystal (< 0.05 in vol. fraction; see Figure 3.2). This is significant since the starting untreated film within the range of 2000-3000 Å from the substrate interface exhibits a density deficit in volume fraction of 0.10. This is an indication that the $CdCl_2$ treatment serves to densify the structure of the film, as indicted in an earlier section of this report, in addition to increasing the grain size. The discernibly larger real part of the dielectric function for the untreated film compared to the single crystal is also of interest and may indicate a slightly higher density (~0.03) due to strain from the high degree of compressive stress in the thin films. This stress is partially relaxed as the film crosses the microstructural transition after 1300 Å.

In the characterization of the $CdCl_2$-treated solar cell structure for on-line measurement applications, it suffices to use the single crystal CdTe dielectric function with void volume fraction as a possible variable parameter that accounts for differences in treated film structure. The analyses described in the following section employ this approach; however, for a more comprehensive description of untreated, treated, as well as non-optimally treated, a physically justifiable method for broadening the critical points is required. This approach has just been developed over the last two quarters of the project and will be described in a later section.

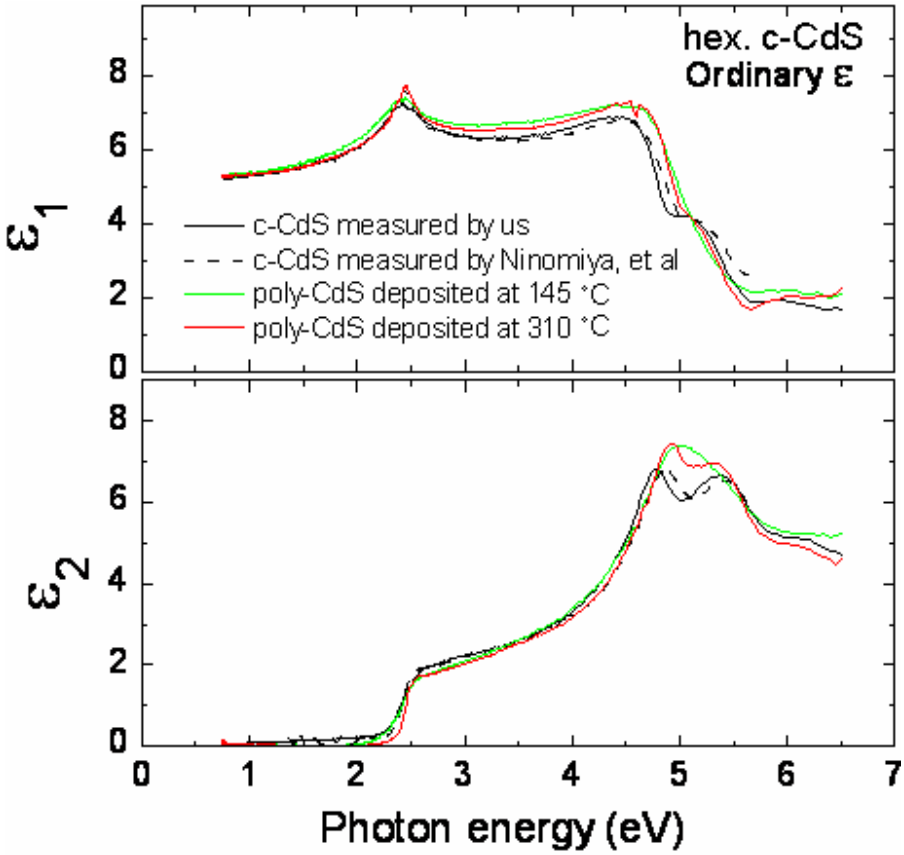

Figure 4.6 *Comparison of the ordinary dielectric function of bulk hexagonal single crystal CdS and two polycrystalline CdS thin films deposited in this study.*

Figure 4.6 shows the dielectric functions measured at room temperature for two CdS thin films -- one deposited at the lowest temperature and the other deposited at a high temperature. Deposition details are provided in Table 2.1. These spectra have been obtained by exact inversion, without assuming a specific analytical form; otherwise the measurement procedure is the same as that for CdTe (see Figure 4.5). In the figure the thin film dielectric functions are compared with the ordinary component of the dielectric function of hexagonal single crystal CdS also measured at room temperature.[6] The similar features of the spectra between the thin film deposited at the higher temperature (310°C) and the bulk crystal -- including the appearance of the (E_1-A, E_1-B) doublet -- suggest that the thin film is hexagonal and that SE probes the ordinary dielectric function. In fact, the extraordinary component of the hexagonal single crystal, as well as the zincblende phase of CdS, exhibit only a singlet at the E_1 energy.[7] As a result, one can conclude that the film is crystallographically oriented with its *c*-axis normal to the surface. A similar conclusion can also be made for the low temperature film; however, in this case the E_1-A and E_1-B are difficult to resolve due to broadening. It can be seen in Figure 4.6 that the CP features of the dielectric function for the higher temperature sample are even stronger and sharper than those of bulk hexagonal single crystal CdS as measured in this study as well as by Ninomiya et al..[6] The broader critical points for the single crystal are likely due to defects from polishing, e.g., dislocations, that extend well below the surface.

In the characterization of the $CdCl_2$-treated solar cell structure for on-line measurement applications, the CdS dielectric function obtained from the higher temperature film in Figure 4.6 is used in the database. In addition, the void volume fraction is used as a variable parameter that accounts for differences that may occur in the film structure, in particular, in the overall amplitude of the optical features. For a more comprehensive description of CdS, a physically justifiable method for broadening the critical points is required, as in the case of CdTe. This approach has been established quite convincingly later in this report for CdS (less convincingly for CdTe). Finally, it should be noted that with the dielectric functions of the four components of the TEC-15 as well as those of thin film CdS and CdTe, a complete analysis of the solar cell structure (without back contact) can be performed to extract thickness and some basic structural and compositional information as will be described in detail in the next section.

4.2. Thickness and Basic Structural Information

Before multilayer optical analysis can be applied to the CdTe solar cell, the library of dielectric functions $\varepsilon = \varepsilon_1 + i\varepsilon_2$ for the TEC-15 glass components can be applied to establish basic structural information on the TEC-15 glass. Figure 4.7 provides an example of the analysis that yields component bulk layer and surface roughness thicknesses, and Figure 4.8 shows the stack structural parameters including the parameter confidence limits.

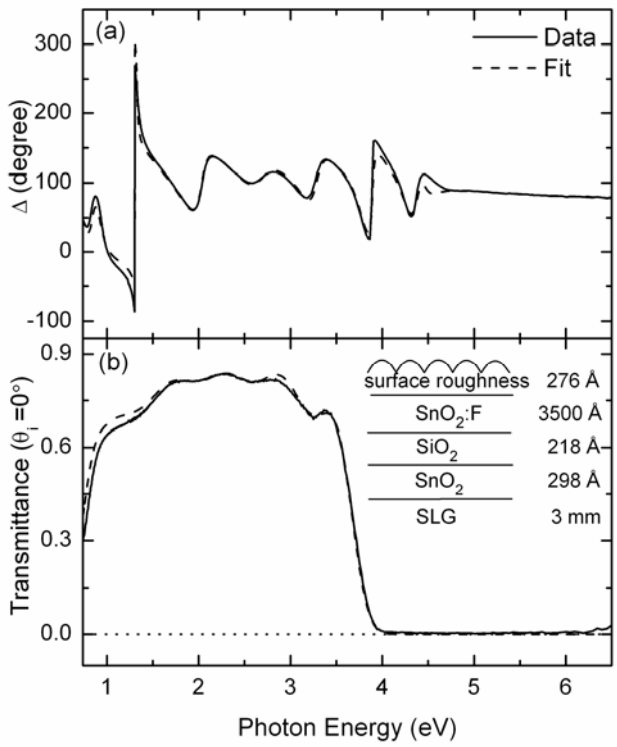

Figure 4.7 *(a) SE angle ψ and (b) the transmittance T at normal incidence ($\theta_i = 0^o$) for a TEC-15 substrate. From the fit (broken lines) to the data (solid lines), the structural information can be extracted [inset in (b)].*

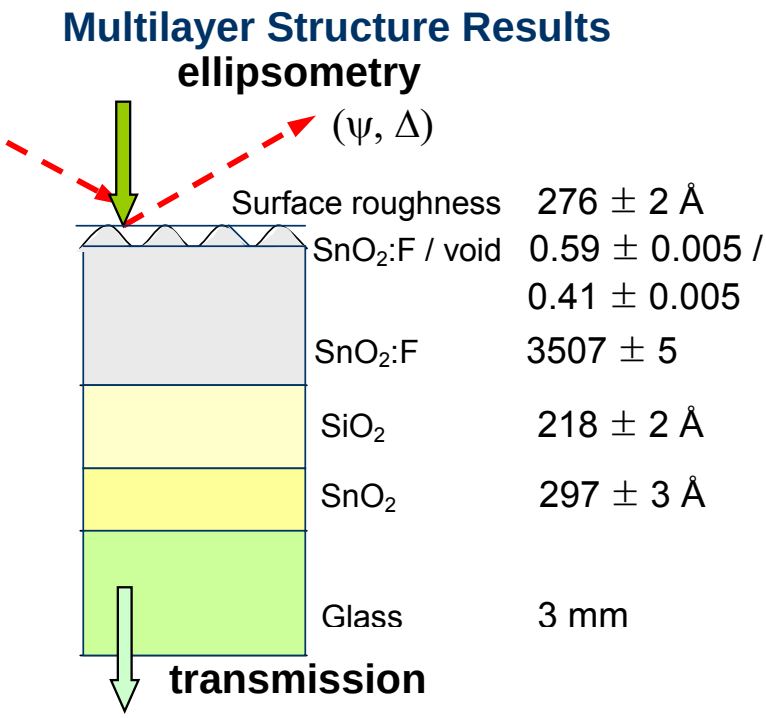

Figure 4.8 *Structural parameters and their confidence limits deduced in a combined analysis of ellipsometric angles (ψ, Δ) and normal incidence transmittance T for a TEC-15 glass substrate. Among the thicknesses deduced include the surface roughness layer, the top-most doped SnO_2:F layer, an intermediate SiO_2 layer, and the bottom undoped SnO_2 layer. In the surface roughness layer, a variable SnO_2:F volume fraction is included which is also deduced in the analysis.*

In Figure 4.7(a) the measured SE *p-s* phase shift difference Δ and in Figure 4.7(b) the transmittance *T* are shown for a TEC-15 substrate. From such data (solid lines), the structural parameters are deduced in a best fit (broken lines), as shown in schematic form in the inset of Figure 4.7(b) and in greater detail with confidence limits in Figure 4.8. With a full set of reference dielectric functions, analyses of the type shown in Figs. 4.7-8 can be performed routinely on TEC-15 glass, and process variations that lead to differences in thickness can be readily detected. In addition to the three bulk layer thicknesses, the microscopic surface roughness layer thickness is extracted using a model for the roughness as a $f_s/(1-f_s)$ volume fraction mixture of the top-most SnO_2:F/void. The dielectric function of this mixture is determined by the Bruggeman effective medium theory.[3] Although this theory is appropriate only for roughness whose in plane scale is much smaller than the wavelength of the light, the thickness of the microscopic roughness for various TEC glass types (7, 8 and 15) deduced using the same optical model scales monotonically with the haze percent of the glass. As a result, there is a close correlation between the microscopic roughness thickness as deduced by SE and the macroscopic roughness thickness that leads to scattering and haze. Thus, the approach developed here is useful for tracking not only thickness of the layers of the TEC glass, but also the haze level. Note that by using reference dielectric functions for the components of the glass, one would be unable to track variations in layer properties from substrate to substrate that may

give rise to variations in optical properties. It is possible, however, to parameterize the dielectric function of one or more of the components and allow some or all of the parameters of one or more components to vary in the fitting. For example, the free electron concentration in the Drude term of an analytical expression for the SnO_2:F dielectric function would be a useful parameter to vary; however, the effectiveness of this approach has yet to be evaluated.

Research to assess the capability of SE for on-line monitoring has been initiated over the last year of the project. In this effort, the top surface reflection from the glass has been eliminated by optically contacting a 60° prism to the glass surface. Although this approach cannot be applied in on-line applications, it is suitable for assessing the information content that can be extracted upon development of the focusing approach of
Figure 4.1. In order to provide a second check on this information, SE has also been performed from the back (CdTe) side of the same solar cell. The geometries of the glass side and CdTe side measurements are shown in Figure 4.9. In order to measure from the CdTe side, the CdTe surface is exposed to a Br_2 etch (0.05 vol.% Br_2 in methanol), which is performed after the $CdCl_2$ treatment, but before back contact formation.

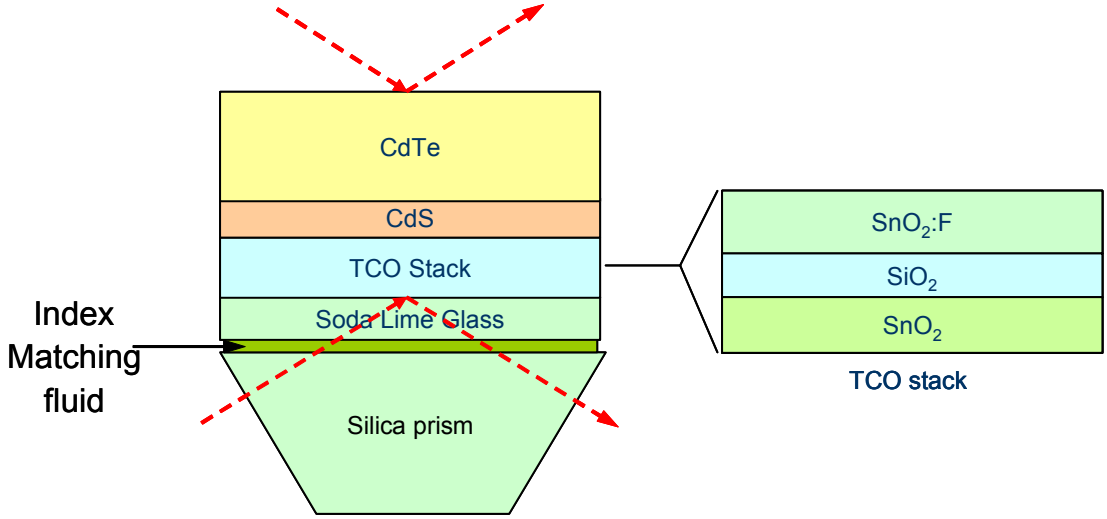

Figure 4.9 *Optical configuration for ex situ SE data acquisition from the CdTe free surface after etching steps and from the prism/glass substrate side without CdTe etching.*

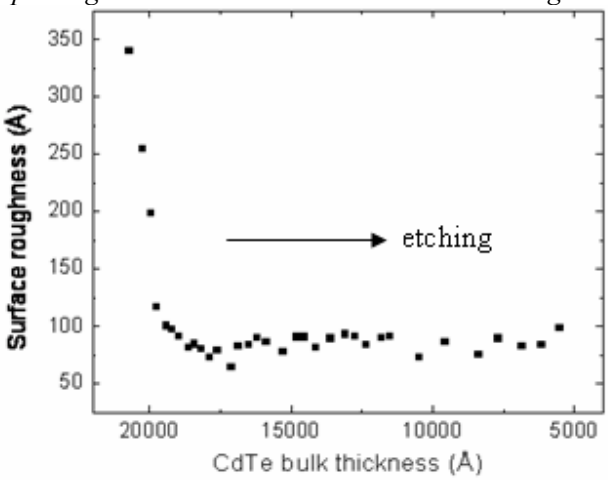

Figure 4.10: *The smoothening effect of Br_2+methanol etching of CdTe.*

The role of this etch is to remove the surface oxide layer, reduce the roughness, and provide a means for depth profiling through the bulk CdTe thickness. The bulk CdTe thickness removed per etching step can be controlled by the Br_2 concentration and etching time. After each etching step, the sample was rinsed with methanol, and then continuously blown with Ar gas during measurement to minimize reoxidation. The smoothening effect of the Br_2+methanol etch is evident in Figure 4.10. Roughness layer thicknesses after etching as small as ~20 Å are possible by optimizing this method.

A dielectric function library, deduced as described in the previous section, was used in the analysis of the ex situ SE data acquired after $CdCl_2$ treatment, but before back contact formation for a CdTe solar cell prepared by sputtering on TEC-15 glass. Measurements of the same sample

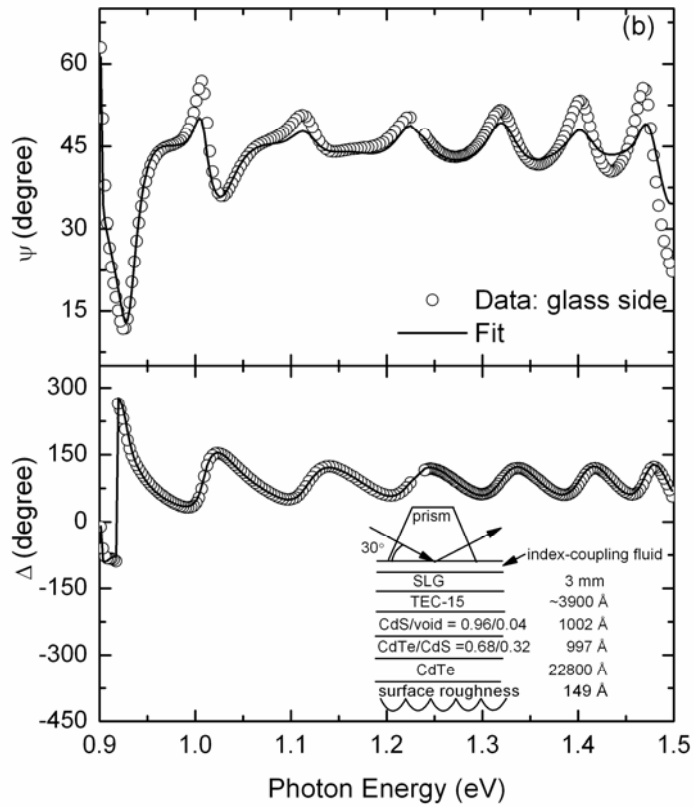

Figure 4.11 *Ex situ SE spectra in (ψ, Δ) (symbols) for a CdTe solar cell after $CdCl_2$ treatment, but before back contact formation, as measured from the prism/glass side. The best fit results (solid lines) yield the structural parameters in the inset.*

have been performed on the prism/glass substrate side (see Figure 4.11) and on the CdTe free surface, the latter after 8 etching steps (see Figure 4.12). The dielectric function library is continuously being refined for improved fitting of such ex situ SE data on the nearly complete devices; such efforts in this direction will be described later in the report. The results of the fits (solid lines) to the (ψ, Δ) spectra (symbols) obtained with the current library, described in the previous section of this report, are shown in Figure 4.11 and Figure 4.12. The structural model used in the analysis of both data sets is the same and includes (from film to substrate side): (i) a CdTe surface roughness layer; (ii) a CdTe bulk layer; (iii) an (interface-roughness + interdiffusion)

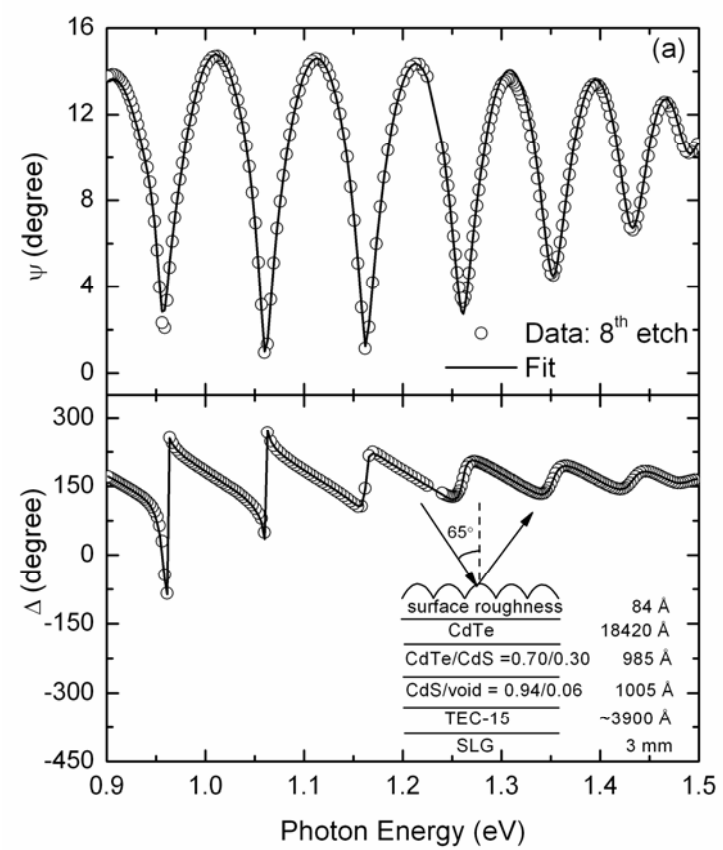

Figure 4.12 *Ex situ SE spectra in (ψ, Δ) (symbols) from the free CdTe surface after 8 Br_2+methanol etching steps. The best fit results (solid lines) yield the structural parameters in the insets.*

region between the CdTe and CdS, modeled for simplicity as a physical mixture using an effective medium theory to simulate an assumed dominant interface roughness effect; (iv) CdS with a variable void volume fraction; (v) an interface roughness layer between CdS and the SnO_2:F of TEC-15; and (vi) the TEC-15 structure.

The insets of Figure 4.11 and Figure 4.12 show the multilayer models of the structure, the former depicting the placement of a 60° fused silica prism on top of the superstrate. In this configuration, an index-matching fluid proves vital in eliminating unwanted incoherent reflections and making good fits possible. Considering the assumptions and simplifications of the model, the agreement in the structural parameters highlighted in Figure 4.13 is significant. (Note that agreement in the CdTe bulk and roughness thicknesses is not expected since the CdTe film has been etched for the back side measurements.) Good agreement is obtained in the CdTe/CdS composition even though this layer requires a more complex modeling approach that includes inter-diffusion. As final supporting results for the overall approach, the CdS layer and CdTe/CdS interface thicknesses deduced from spectra collected at the CdTe free surface in 24 successive etches shown in Figure 4.14 exhibit ~ ±1-1.5% deviations, and the average values lie within the confidence limits of the analyses performed on spectra collected through the prism/glass.

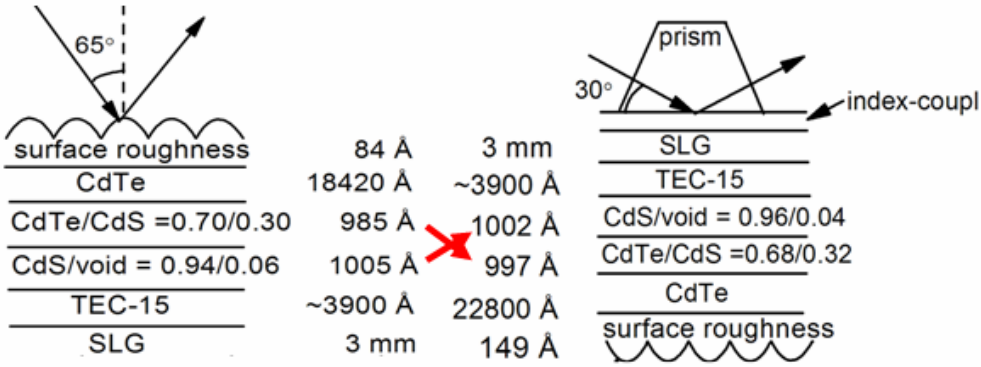

Figure 4.13 *A comparison of the structural parameters deduced from spectra collected from the CdTe surface after eight etching steps (left) and from spectra collected through the prism/glass (right). Excellent agreement in the CdS and CdTe/CdS interface layer thicknesses and compositional parameters are obtained. Agreement in the CdTe bulk and roughness layer thicknesses is not expected, however, since the CdTe film has been etched for the back side measurements (left).*

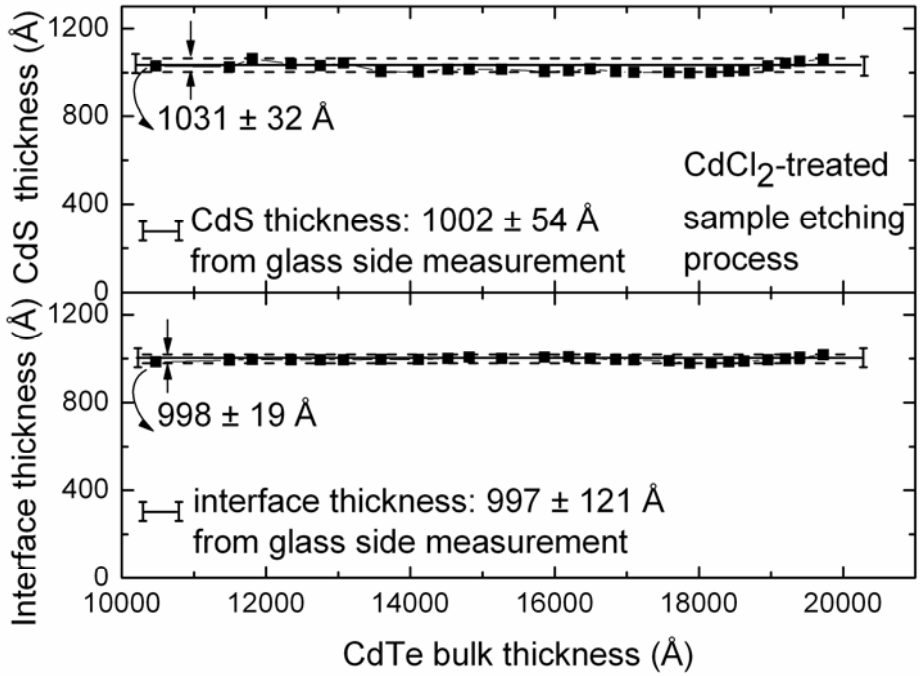

Figure 4.14**:** *CdS and CdTe/CdS interface layer thicknesses deduced from spectra collected through the prism/glass (solid line) and from spectra collected from the CdTe surface in successive etches (points, dotted line extrema).*

4.3. Interfaces

In the analysis of the solar cell structure by ex situ SE for on-line monitoring applications, the interface between CdS and CdTe has been modeled as a physical mixture of CdTe and CdS using an effective medium theory (see Figs. 4.11 -14). This model is based on the assumption that microscopic roughness between the two films dominates the imperfections of the interface, and this roughness is induced by the ~300 Å of microscopic roughness on the TEC-15 glass surface. When such a model is applied to the cell structure, however, an interface layer ~ 1000 Å is obtained (see Figs. 4.13-14), rather than the ~300 Å that would be expected if the CdS was to conformally cover the roughness on the TEC-15 glass. Thus, it is likely that the additional ~700 Å is simulating the effect of additional interface components as shown in figure 4.15. In this suggested schematic, the center of the interface is the microscopic roughness layer; on each side of this layer are likely to exist diffusion layers of CdS_xTe_{1-x} of small x (on the CdTe side) and CdS_xTe_{1-x} of x near 1.0 (on the CdS side). In order to establish a better understanding of the optical structure of the interface, along with reference dielectric functions that can be employed for a better fit and additional useful information in on-line monitoring applications, the optical properties of CdS_xTe_{1-x} alloys versus composition and measurement temperature have been determined in this study. Real time SE has been applied for this purpose beacuse it provides accurate thicknesses (bulk and surface roughness) that enable accurate determination of the dielectric functions of the alloy films. In addition, since such measurements are performed during deposition as well as upon cooling of the thin film to room temperature, contamination and oxidation effects on the optical properties are avoided. In addition to determining the optical properties of the interface components, it is also of interest to apply RTSE to understand how these two layers interact during interface formation under idealized conditions, i.e., in the absence of interface microscopic roughness layers.

A low substrate temperature of T=190°C was used in the fabrication of the CdS_xTe_{1-x} alloys to avoid phase separation.[2] Additional deposition parameters are listed in Table 2.1. The key variable x was determined on the basis of real time SE calibration of the individual CdTe and

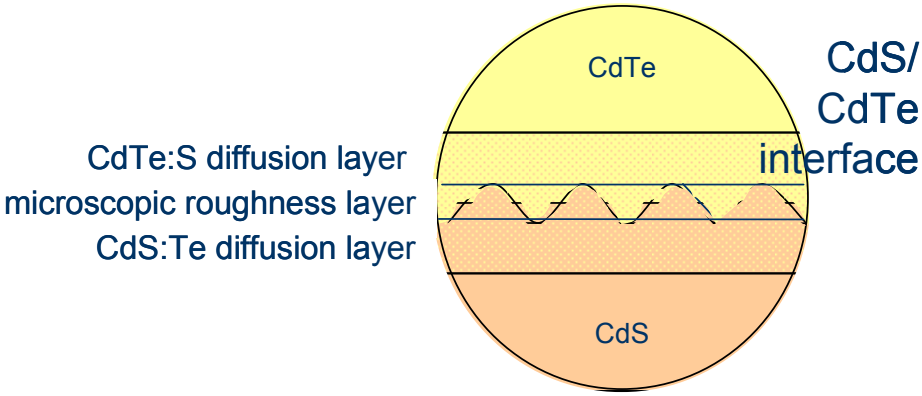

figure 4.15 *Proposed interface layers in a TEC-15/CdS/CdTe structure for on-line analysis of CdTe solar cell structures by spectroscopic ellipsometry.*

CdS deposition rates versus target rf power as described previously. The optical properties of the alloys as functions of composition for measurement temperatures of T = 190°C and T = 17°C are shown in Figure 4.16 and Figure 4.17, respectively. The general trends observed directly by inspection are as follows: (i) in most cases the dielectric functions vary consistently with x value, and lie between those of CdTe and CdS --- the two endpoint compositions; (ii) all dielectric functions of the alloys show critical point (CP) features; however, these are much broader than the endpoint features; (iii) the apparent band gap shows a clear bowing effect vs. x, observed most clearly in the peak of ε_1, in consistency with previous studies;[8] and (iv) all CP energies, including the band gap, undergo the expected blue shifts when samples are cooled from deposition T to room T. Similar trends with T have been observed for CdTe and CdS. Parameterization of these dielectric functions have been performed. Based on this parameterization, one is able to generate the dielectric function of an arbitrary alloy composition at an arbitrary measurement temperature.

This parameterization was applied in the analysis of RTSE results collected during T = 190°C depositions of CdTe on CdS/c-Si, and the reverse sequence of CdS on CdTe/c-Si. In this study, a crystalline Si substrate was used in order to minimize microscopic roughness at the interface between the two materials so that the dominant deviation from interface perfection is expected to be inter-diffusion. The virtual interface approximation was applied to the RTSE data to find x for the topmost ~ 8 Å of deposited material during interface formation. Figure 4.18 shows a schematic of the optical structure for the normal sequence of CdTe deposition on CdS as well as the capabilities of the virtual interface method. The final results of this analysis for the normal and inverted deposition sequences are shown in Figure 4.19. In both deposition

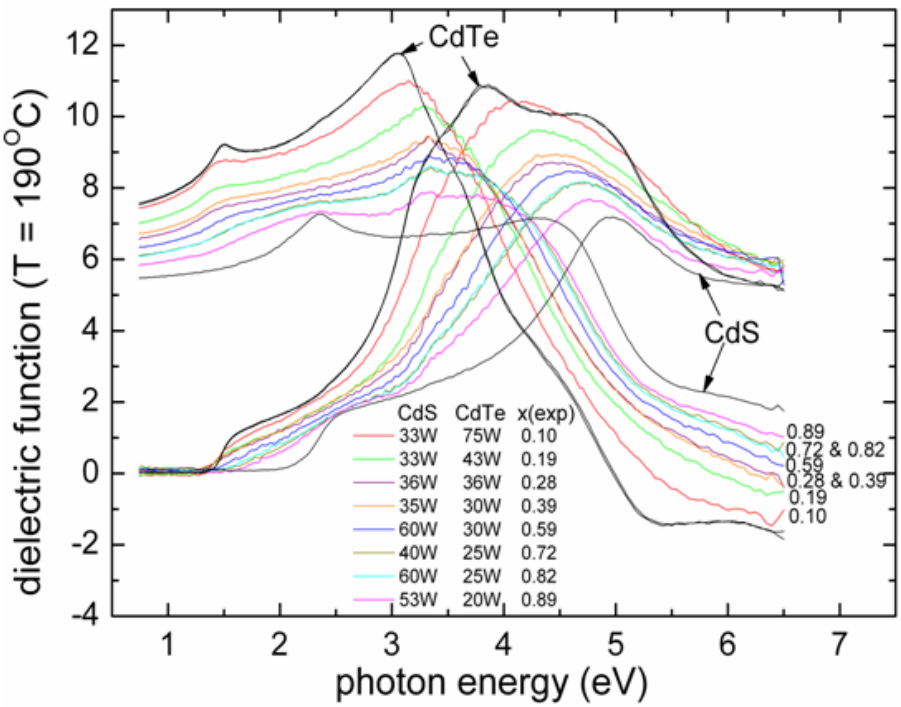

Figure 4.16 *Complex dielectric functions versus x obtained in real time for ~200 Å thick CdS_xTe_{1-x} alloys at T = 190°C.*

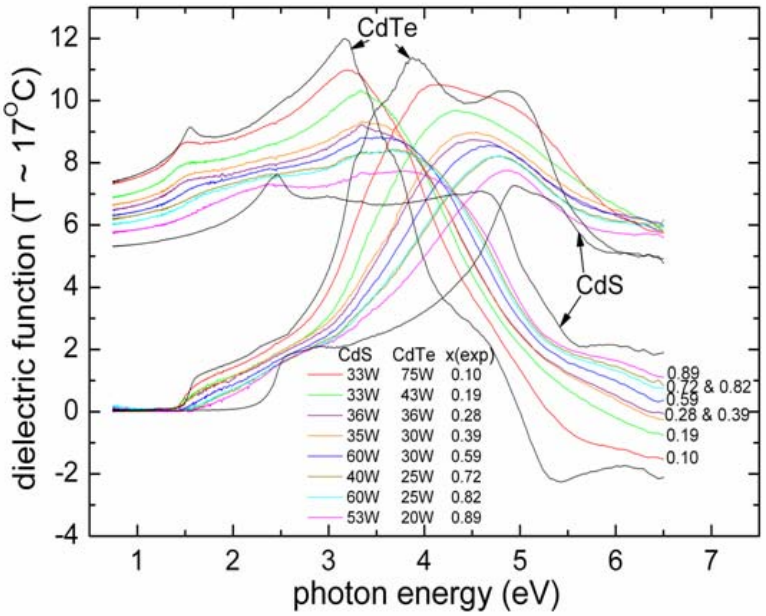

Figure 4.17 *Complex dielectric functions versus x obtained in situ for ~200 Å thick CdS_xTe_{1-x} alloys after cooling the deposited film to 17 °C .*

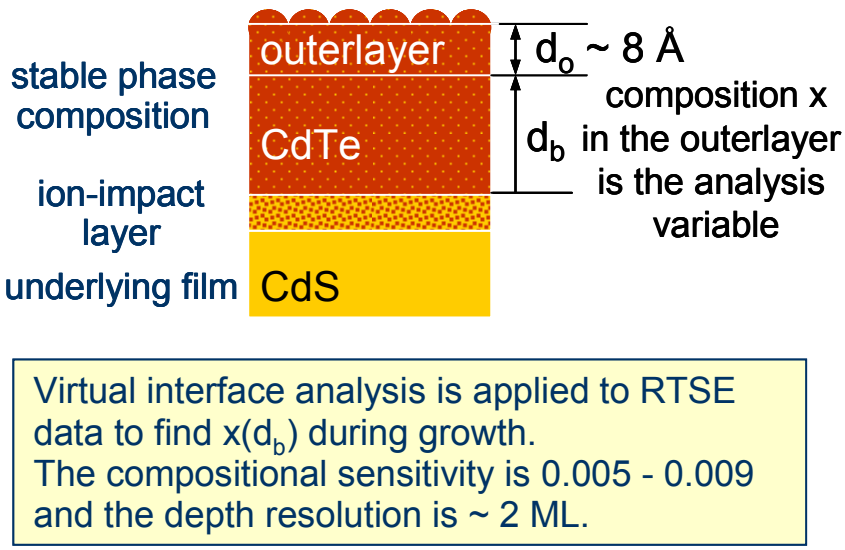

Figure 4.18 *Optical model and characteristics of the virtual interface analysis method for investigation of CdS/CdTe interface formation by RTSE*

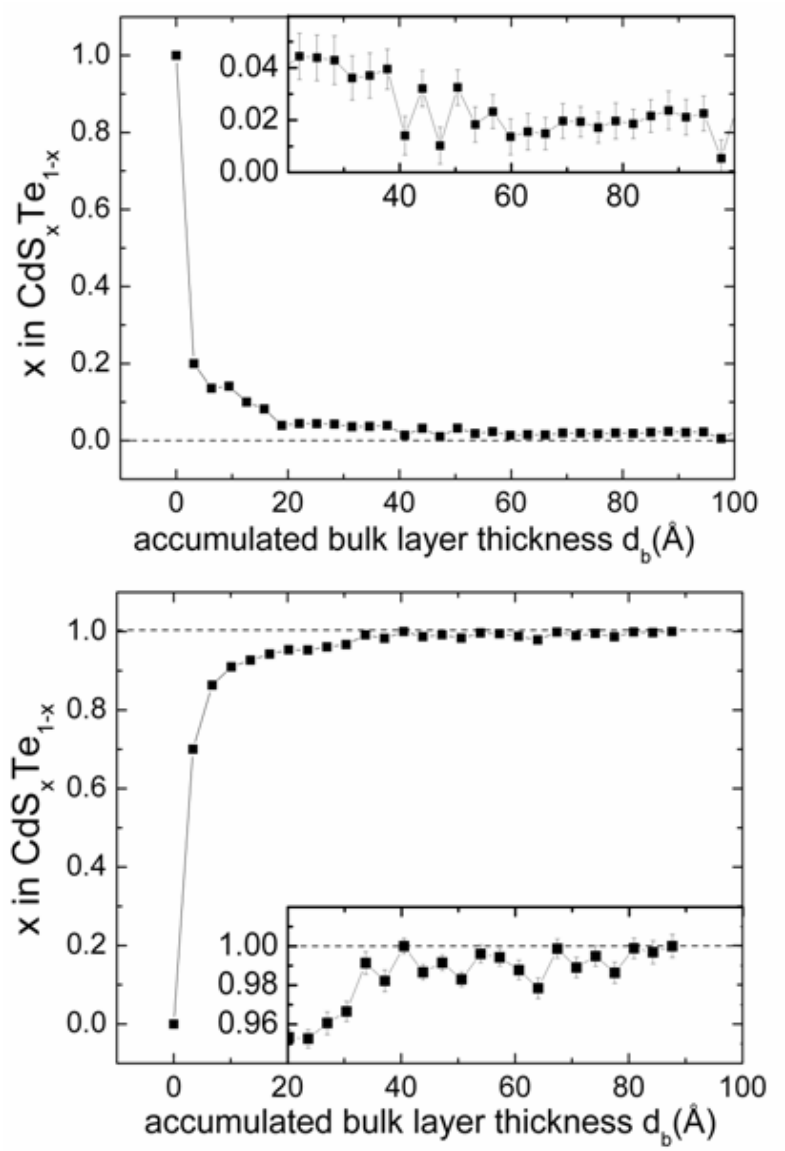

Figure 4.19: *Composition profiles $x(d_b)$ in CdS_xTe_{1-x} for depositions at T = 190°C for CdTe on CdS (upper) and CdS on CdTe (lower).*

sequences, there is a ~40 Å layer with a strong gradient in *x*, possibly generated by ion impact in the sputtering process (see Figure 4.18). Beyond this thickness, S diffusion into CdTe exhibits a tail with *x* ~0.02; whereas for the inverted structure, Te diffusion into CdS exhibits a negligible tail, indicating a lower diffusion coefficient. The interface structure measured in the studies of Figure 4.19 are characteristic of a deposition temperature of 190°C with no post-deposition treatment. In order to obtain a better understanding of the actual cell process, corresponding studies need to be performed at a higher deposition temperature, and the role of the post-deposition $CdCl_2$ treatment also needs to be studied. For the latter studies, it may be necessary to apply ex situ SE due to the difficulty of performing RTSE during the process with an opaque substrate such as a Si wafer.

4.4. Expansion to Temperature, Grain Size, and Strain

Capabilities for on-line optical monitoring are being sought in these studies beyond the simple thickness and compositional information described previously. The additional information that may be possible to deduce includes not only interface alloy compositions, as described in the previous section, but also temperature, grain size, and strain. All these film characteristics have a significant influence on the critical point energies or widths and so should be determinable from fitting of optical spectra. Because of the existence of multiple critical points, the capability of extracting all characteristics of the film independently without correlation may be possible. The requirement for such on-line process monitoring development is the database that will support these capabilities.

4.4.1. Temperature Effects

Because the temperature of a TEC-15/CdS/CdTe plate will be above room temperature as it progresses out of the CdTe deposition chamber, it is important to monitor the temperature if only to identify the proper database to use for the dielectric functions. Because all dielectric functions, including the critical parameters of CdTe and CdS depend on temperature, it is important to establish this information for proper interpretation of thicknesses, compositions, grain size, and strain. Here results are demonstrated first for the CdTe E_0 band gap parameters of energy and broadening and subsequently for the CdS E_0 energy and broadening. Although all dielectric function parameters will depend on temperature, the effect on the E_0 energy and width has the greatest impact in interpreting on-line spectra.

The E_0 band gap of the CdTe film is obtained as a function of measurement temperature by temporarily suspending the deposition after a thickness of ~1000 Å, then stepwise cooling as measurements are taken, and finally reheating for continuation of the deposition. Two derivatives of the spectra are taken, and the results are fit to the standard Lorentzian-broadened lineshape function. Figure 4.20(left panel) shows the final results for the band gap energy as a function of

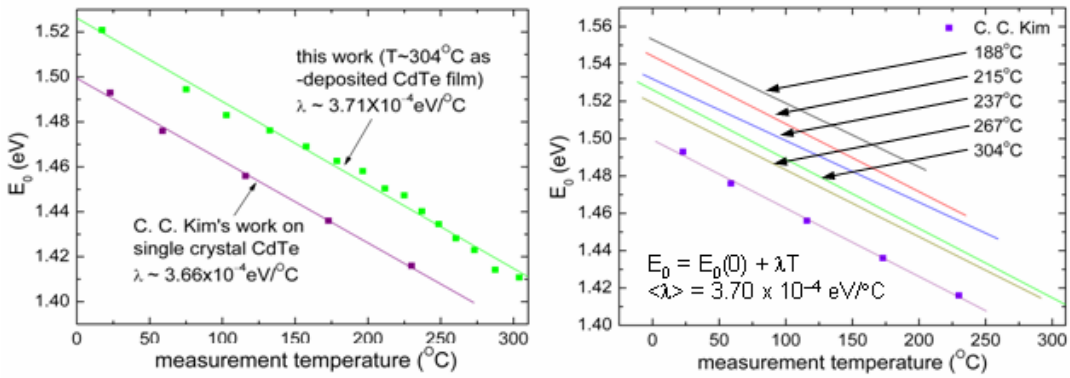

Figure 4.20 *The E_0 critical point energy plotted as a function of true temperature obtained during cooling of a CdTe film from the deposition temperature of 304 °C to room temperature (15 °C) (left). Also shown are the linear variations in critical point energies for the set of five CdTe films prepared at different temperatures (right). Results for single-crystal CdTe are shown in both panels for comparison.*

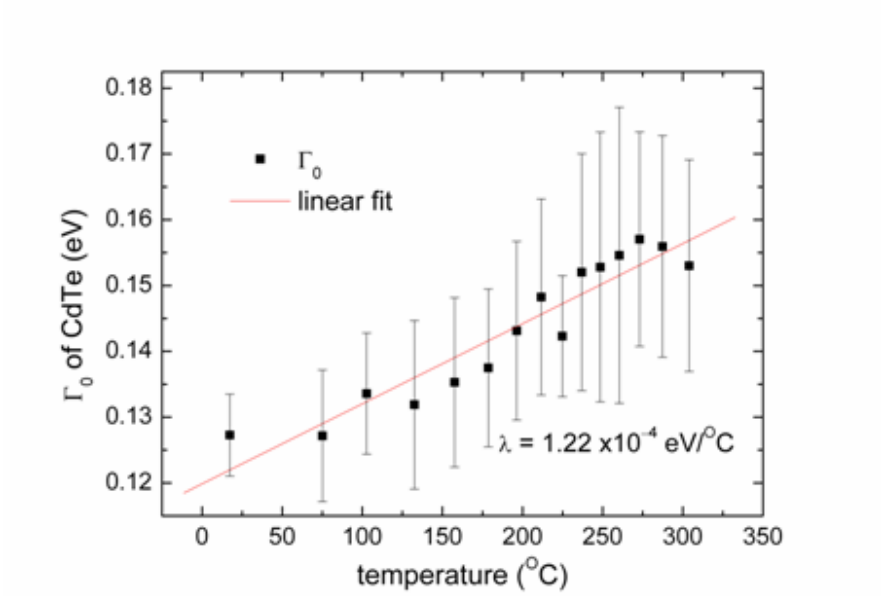

Figure 4.21 *The E_0 critical point width Γ_0 plotted as a function of true temperature obtained during cooling of a CdTe film from the deposition temperature of 304°C to room temperature.*

measurement temperature for the CdTe film deposited at 304°C, starting at the deposition temperature and progressing to room temperature. A key parameter in this study is the slope of the linear change in band gap with temperature. The value obtained for this CdTe film is 3.71 x 10^{-4} eV/°C, a value within ~ 1.5% of that reported for single crystal CdTe.[9] Similar results are obtained for all five CdTe samples, as shown in the right side of Figure 4.20. Averaging the slopes yields a value of 3.70 x 10^{-4} eV/°C. In addition to its potential usefulness in on-line monitoring, these data provide a means for calibrating the substrate temperature for any deposited CdTe film -- one simply measures the band gap shift between the process temperature and room temperature, and divides by the average temperature slope to obtain the process temperature. The width of the E_0 transition, indicated by Γ_0 also varies with temperature due to enhancement of electron-phonon scattering, as shown in Figure 4.21. For the range of temperatures of relevance in film deposition and processing, electron-phonon scattering occurs at a much lower rate than grain boundary scattering for the as-deposited films, but at comparable rates for $CdCl_2$ treated films.

The temperature dependences of the E_0 band gap and its associated broadening parameter Γ_0 for the CdS film deposited at the highest temperature of 320°C are shown in Figure 4.22 and Figure 4.23, respectively.

In spite of the nearly parallel data sets for the films and the single crystal in Figure 4.20, the band gap energies themselves are significantly shifted, by as much as 60 meV relative to the single crystal. This effect makes it impossible to calibrate substrate temperature based on a single measurement of band gap energy; either energy differences or data from multiple critical points are required. As described in greater detail later in this subsection, the variation in band gap among the different thin film samples at a fixed temperature is attributed to strain associated with compressive stress in the films.

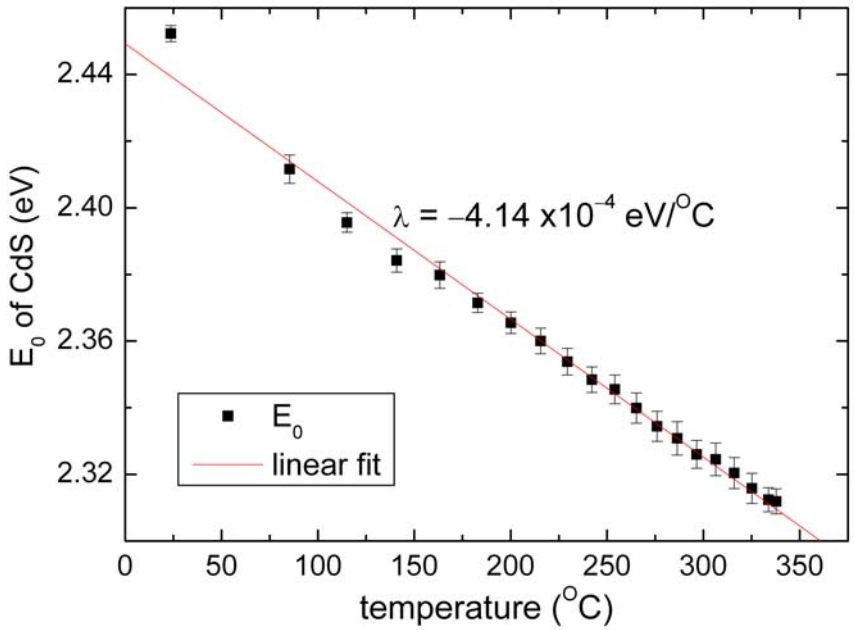

Figure 4.22 *The E_0 critical point energy plotted as a function of true temperature obtained during cooling of a CdS film from near the deposition temperature of 320℃ to near room temperature.*

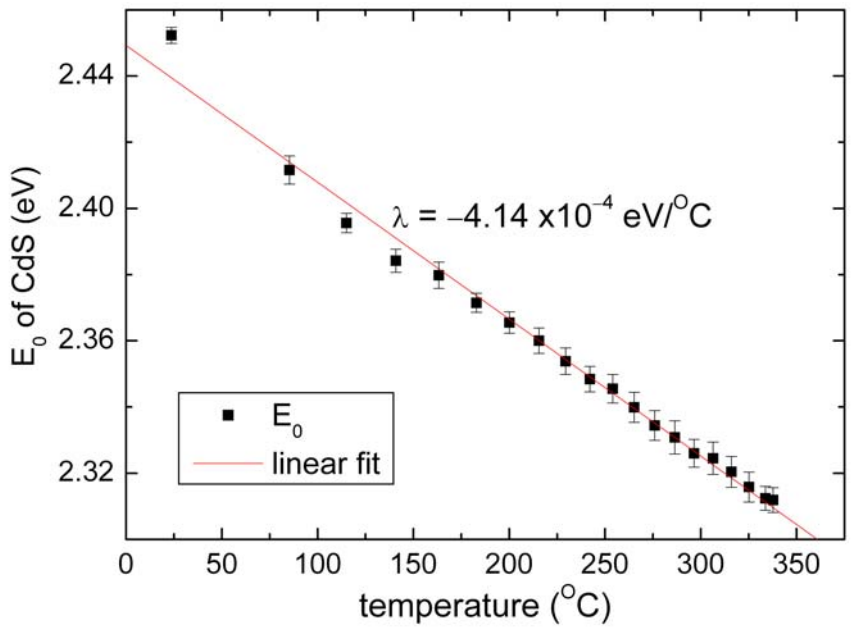

Figure 4.23 *The E_0 critical point width Γ_0 plotted as a function of true temperature obtained during cooling of a CdS film from near the deposition temperature of 320℃ to room temperature.*

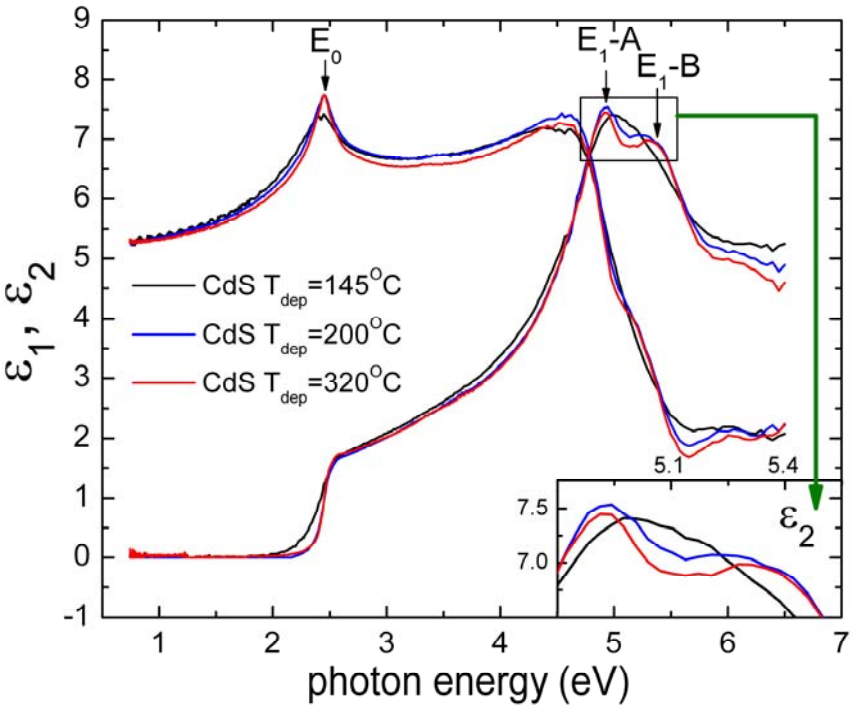

Figure 4.24 *Dielectric functions measured at ~15°C for CdS films magnetron sputter-deposited at three different temperatures.*

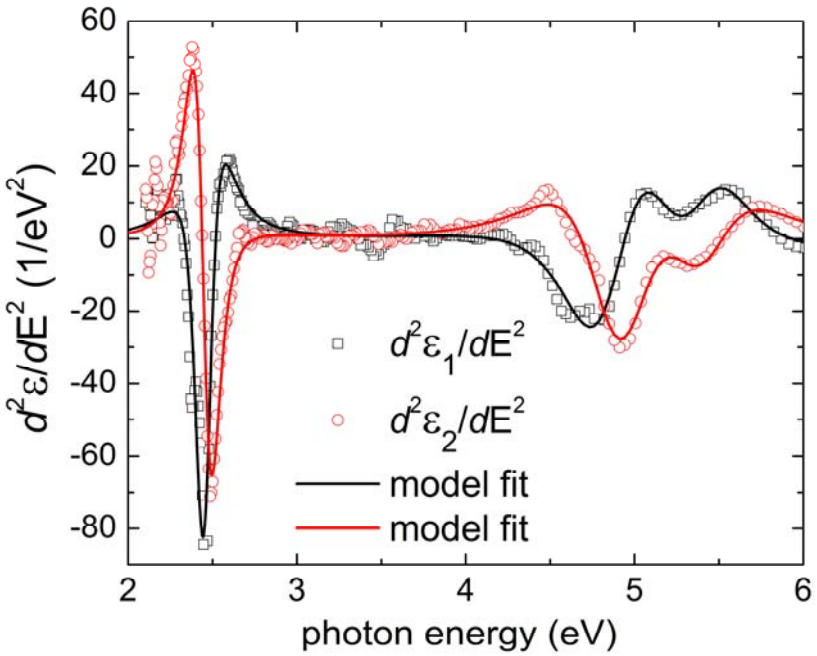

Figure 4.25 *Second derivative spectra (open squares and circles) in ε for CdS deposited at T=160°C and measured at T~15°C. The fit (solid lines) is based on Equation (1).*

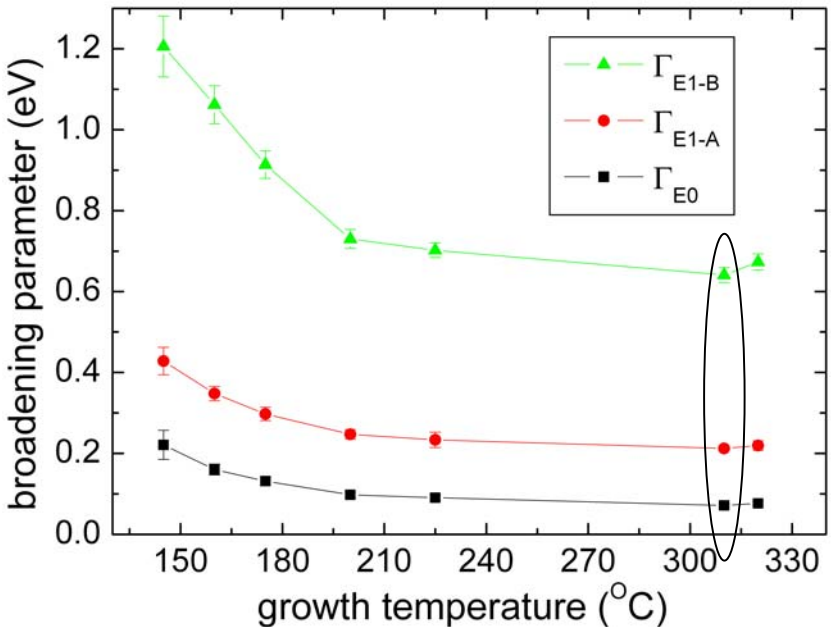

Figure 4.26 *Broadening parameters measured at ~15°C for CdS films deposited at different T; the lowest broadening parameter values are circled.*

4.4.2. Grain Size Effects

An additional complication that provides further opportunity for advanced on-line analysis of the CdS and CdTe components of the solar cell is the variability in the dielectric functions due to changes in the substrate nature and detailed deposition and post-process conditions. Although voids are being used currently to account for such sample-to-sample variations in CdS and CdTe structure, it has been recognized that a more sophisticated approach is required to overcome the weakness inherent in the oversimplified modeling of Figure 4.11 and Figure 4.12. This approach can be developed starting from a study of the dielectric functions of CdS and CdTe films sputter deposited at different temperatures (see Table 2.1). The CdS study will be presented first as its dielectric function shows clear characteristics consistent with a semi-classical model of electron scattering at grain boundaries.

Previously it was suggested that the grain size of as-deposited CdS shows a strong dependence on deposition temperature, as seen from the widths of the critical points (CP's) in the optical properties of the hexagonal CdS (see Figure 4.6). In this section, the procedure for quantifying this dependence will be demonstrated. From the observed consistent variations in width for the different CP's, important information can be deduced, including (i) the average grain size of the film (obtained in this case as a function of substrate temperature) and (ii) the group speeds of the electronic excitations in CdS. Once the group speeds are obtained, the optical properties for any hexagonal CdS film can be interpreted to deduce the grain size. As shown in Figure 4.24 and Figure 4.25, the E_0 (fundamental gap), E_1-A, and E_1-B CP's are evident in the T~15°C dielectric functions ε of the CdS samples. To quantify these CP's, the second derivative spectra in ε were fit assuming the parabolic band approximation to the critical points (CP-PB):

$$\varepsilon = \Sigma_n A_n (E - E_n - i\Gamma_n)^{\mu_n} \exp(i\varphi_n) \qquad (1)$$

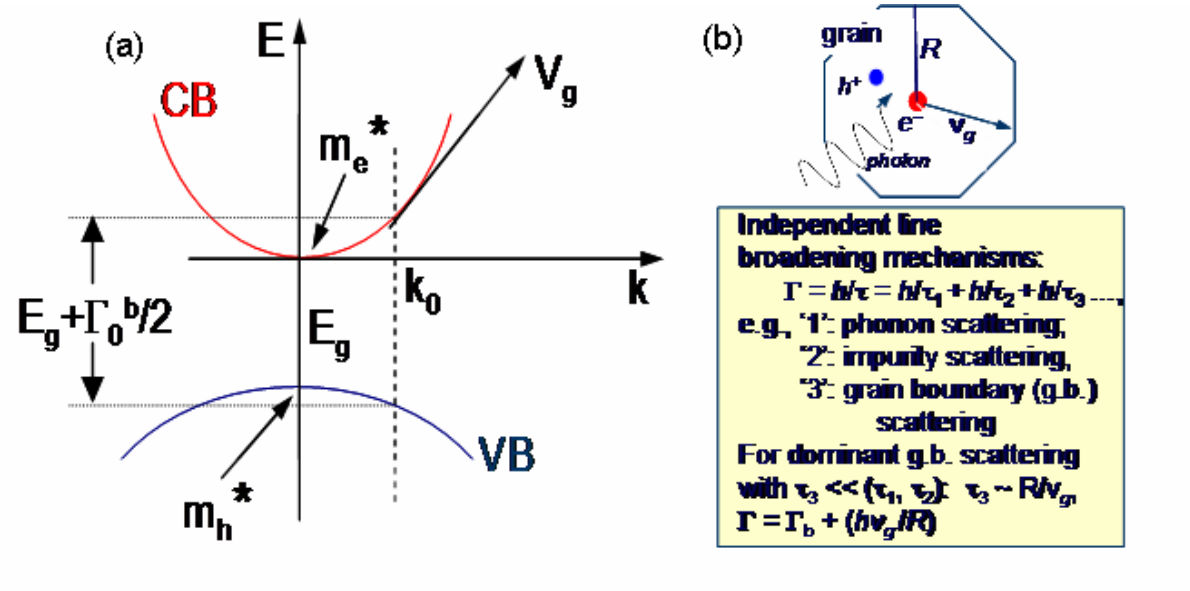

Figure 4.27: *(a) Schematic band diagram of a direct gap semiconductor (such as CdS) around the fundamental gap E_0; (b) Schematic semiclassical model for grain boundary scattering.*

where A_n, E_n, Γ_n, μ_n, and φ_n are the amplitude, band gap, broadening parameter, exponent, and phase of the nth CP, respectively. One such fit is shown in Figure 4.25.

The best fit broadening parameter Γ_n is plotted as a function of deposition temperature T in Figure 4.26. The variations of Γ_n with T for all CP's are quite consistent. The broader critical points for the single crystal are likely due to defects from polishing, as noted earlier. Thus, Γ_n for the 310°C sample can be taken as intrinsic to single crystal CdS (denoted by Γ_{bn}) -- even more so than results from careful measurements on single crystal CdS itself. Thus, the E_0 transition for this sample can be related to the band structure of CdS, shown schematically in Figure 4.27(a). Here the broadening parameter associated with the fundamental gap, Γ_{b0}, indicates how far away from the Brillouin zone center an excitation can occur and still contribute significantly to the optical transitions at E_0. Assuming the parabolic band approximation for the E_0 transition with electron and hole effective masses of $m_e^* = 0.2m_e$ and $m_h^* = 0.7m_e$,[10] the group speed associated with this excitation can be estimated as $v_{g0} \sim 2.2 \times 10^5$ m/s. If the dominant broadening effect is assumed to result from the limited excitation lifetime due to grain boundary scattering, then the following relation can be applied [see Figure 4.27(b)]:

$$\Gamma_n = \Gamma_{bn} + (\hbar v_{gn}/R) \qquad (2)$$

where R is the deduced grain radius.[11] Using the values of v_{g0} and Γ_{b0} for single crystal CdS, R can be calculated versus T as shown in Figure 4.28. As a check of the validity of the general approach, the other two critical point widths $\Gamma_{E1\text{-}A}$ and $\Gamma_{E1\text{-}B}$ are plotted versus R^{-1} in Figure 4.29. The linear relation predicted by Equation (2) is closely followed. From the linear fits, the group speeds for the E_1-A and E_1-B excitations are determined as 3.3×10^5 and 8.8×10^5 m/s, respectively.

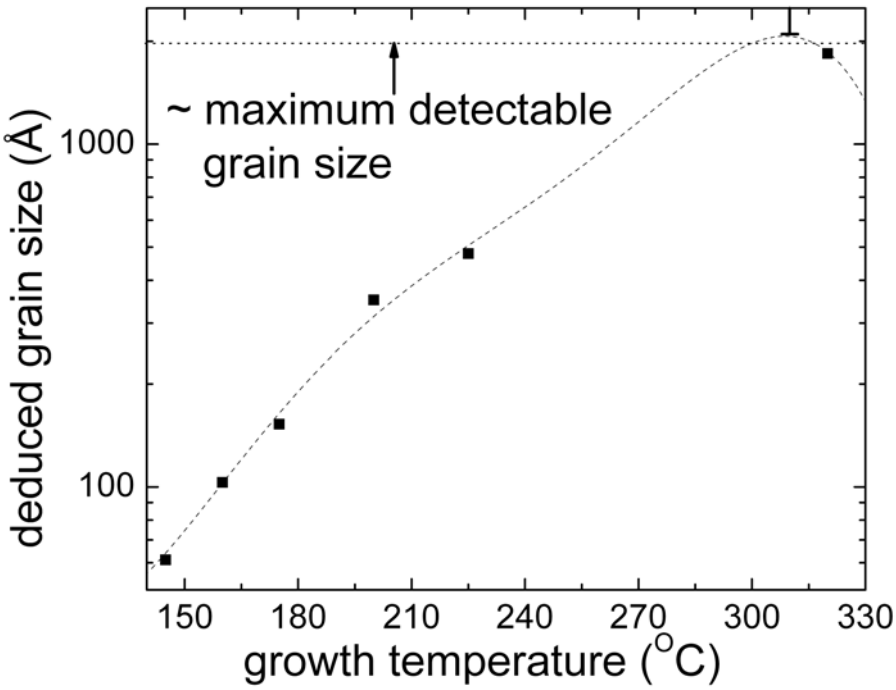

Figure 4.28: *Grain size in CdS thin films estimated from the broadening parameter of the E_0 transition by using the inverted form of Equation (2).*

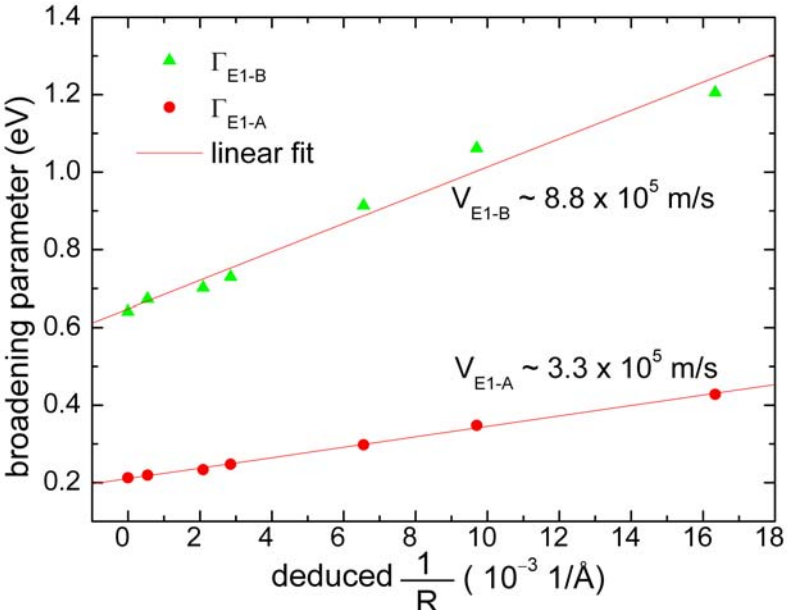

Figure 4.29: *Broadening parameters of the E_1-A and E_1-B CPs vs. inverse grain size; group speeds calculated from the linear fits and Equation (2) are indicated.*

With this information, a dielectric function parameterization is possible that uses the grain size as a controlling parameter -- similar to what is now possible with void fraction. In this parameterization the grain size is assigned, and using the known values of Γ_{bn} and v_n, then the Γ_n values can be determined according to Eq. (2). Once the Γ_n values are determined, they are substituted along with the other parameters associated with the T=310°C film into Eq. (1) to determine the dielectric function of a film with a given grain size. This is one of a few steps needed to extract physical parameters, including void fraction, grain size, and strain, from an ex situ measurement of the nearly complete solar cell with an on-line mapping capability.

A similar procedure has been performed for extracting the grain sizes and transition group speeds for the series of CdTe films prepared at different substrate temperatures. In this case, some complications are encountered. First, the CdTe E_0 transition has a weaker amplitude than that of CdS; as a result the Γ values are more difficult to determine accurately compared to the case of CdS. Inaccurate Γ values lead to inaccurate R values, which then introduce significant abscissa noise into the overall analysis procedure and de-linearize the relationships that establish the group speeds. As a result, the E_2 transition is used instead of E_0 to determine the grain size of CdTe; however, the band structure assocated with the E_2 is not well-known, and thus, the group speed is not known *a priori*. In this case, the group speed of E_2 is determined iteratively so as to ensure that the group speed of E_0 matches that estimated theoretically from the band structure according to Figure 4.27(a).

The overall results for R as a function of substrate temperature, as well as the Γ vs. $1/R$ relationships that establish the group speeds for the different transitions are shown in Figs. Figure 4.30 and Figure 4.31. These results show promising features that help support the procedure. First, the relationship that establishes the group speed of the $E_1+\Delta_1$ transition is followed quite accurately; this is to be expected since the $E_1+\Delta_1$ transition appears prominently in the dielectric function spectra, and next to E_2, its Γ value can be accurately determined. Second, the group speed of the E_1 transition is close to that of the $E_1+\Delta_1$ transition; this is to be expected since the $L_{4,5}$ and L_6 valence bands of CdTe (the initial states of the E_1 and $E_1+\Delta_1$ transitions) are closely parallel. Finally, although the error bars of Γ for the E_0 transition are large, the best fit Γ vs. $1/R$ linear relation almost crosses each error bar with a value that is in agreement with theory as described in Figure 4.27(a). In general, it can be concluded that analysis of the optical properties of CdTe can provide grain size in a similar way as has been observed quite convincingly for CdS.

4.4.3. Strain Effects

Figure 4.32 shows the variation in the room temperature (15°C) E_0 band gap as a function of deposition temperature for the series of CdTe films. It should be noted that these results were obtained for films deposited to thicknesses of ~1000 Å. Given the significant compressive stress observed in sputter-deposited thin films in general,[12] it is reasonable to attribute the band gap shifts in the CdTe films to the associated strain. An estimate of the stress level in these films can be obtained based on previous measurements that relate hydrostatic pressure to band gap in single crystal CdTe. These measurements have established a pressure coefficient of 65 meV/GPa.[13] Although the stress in the CdTe films is uniaxial rather than hydrostatic, the estimate may be a reasonable one because the optical electric field is strongly refracted into the material and thus probes the high strain direction. The right scale in Figure 4.32 uses the

pressure coefficient to estimate the compressive stress in the CdTe films; values from 0.4 to 0.9 GPa are obtained.

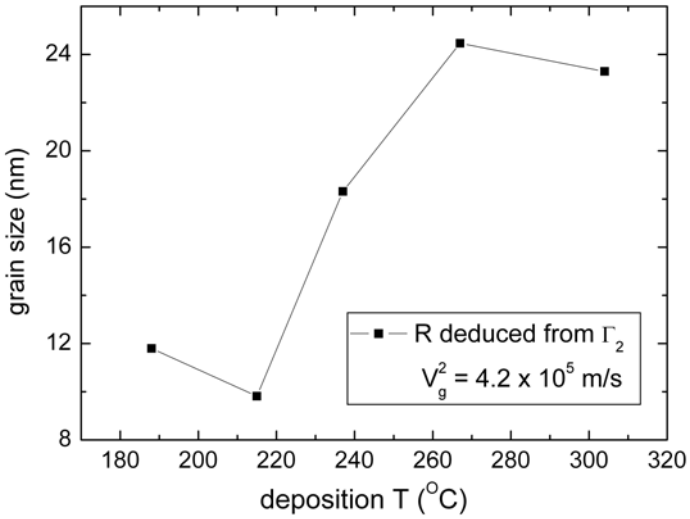

Figure 4.30 *Grain size as a function of deposition temperature for CdTe deduced from the E_2 transition widths. The group speed for this transition was determined so as to force the group speed of the E_0 transition to assume the value of 2.3 x 10^5 m/s, which is the value predicted from the band structure.*

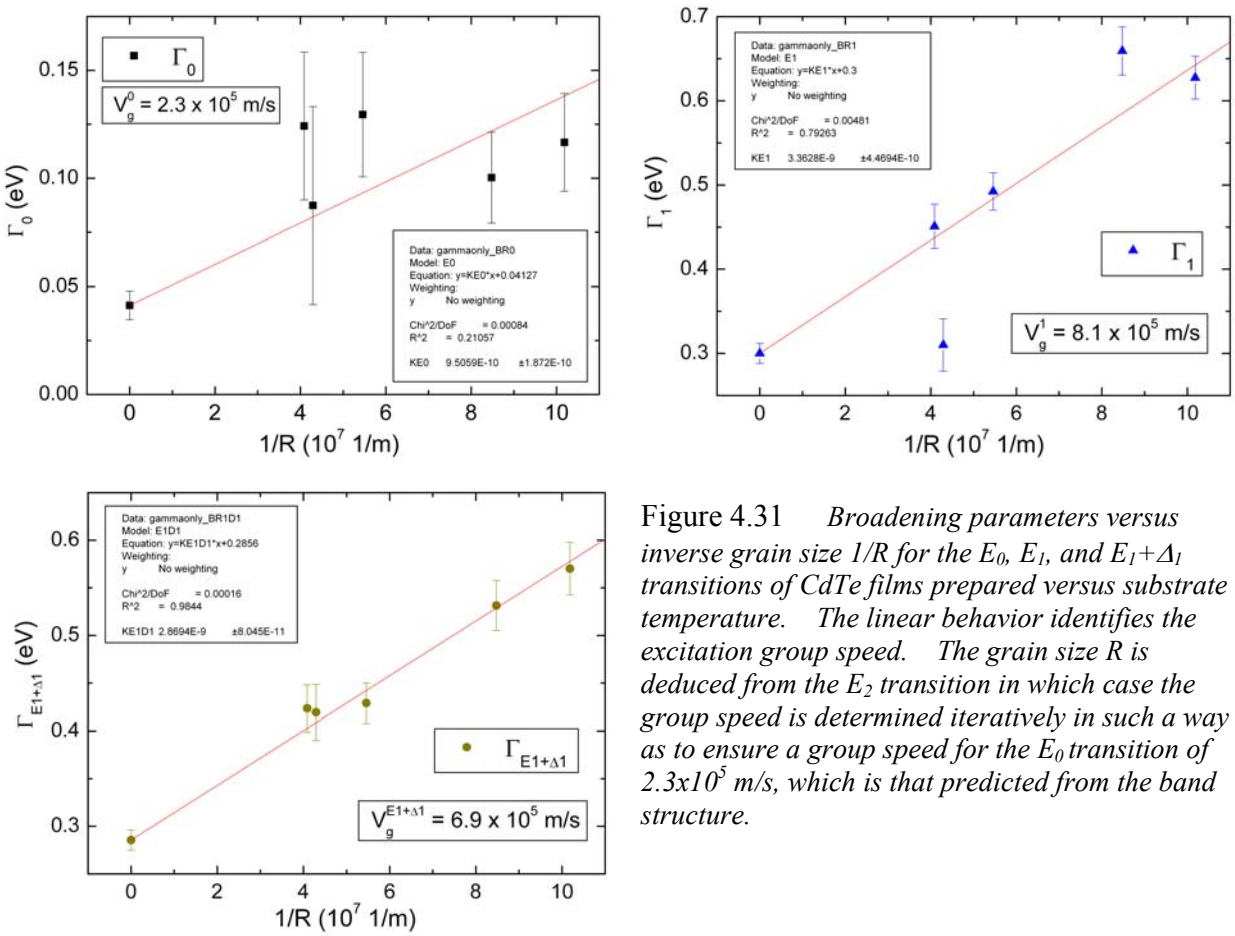

Figure 4.31 *Broadening parameters versus inverse grain size 1/R for the E_0, E_1, and $E_1+\Delta_1$ transitions of CdTe films prepared versus substrate temperature. The linear behavior identifies the excitation group speed. The grain size R is deduced from the E_2 transition in which case the group speed is determined iteratively in such a way as to ensure a group speed for the E_0 transition of 2.3x10^5 m/s, which is that predicted from the band structure.*

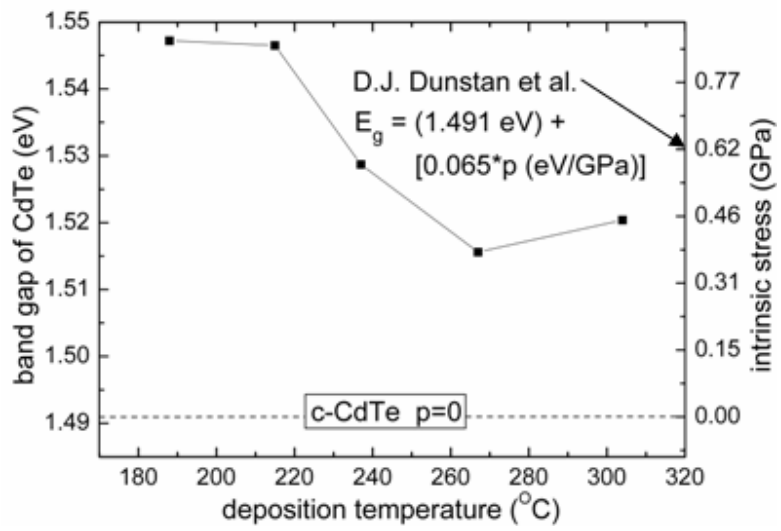

Figure 4.32 *Room temperature (15 °C) E_0 band gap for CdTe films obtained after a deposited thickness of 1000 Å, plotted as a function of the substrate temperature used in the deposition process. The right scale indicates the level of compressive stress in the film, assuming the linear relationship between the band gap and hydrostatic pressure as shown.*

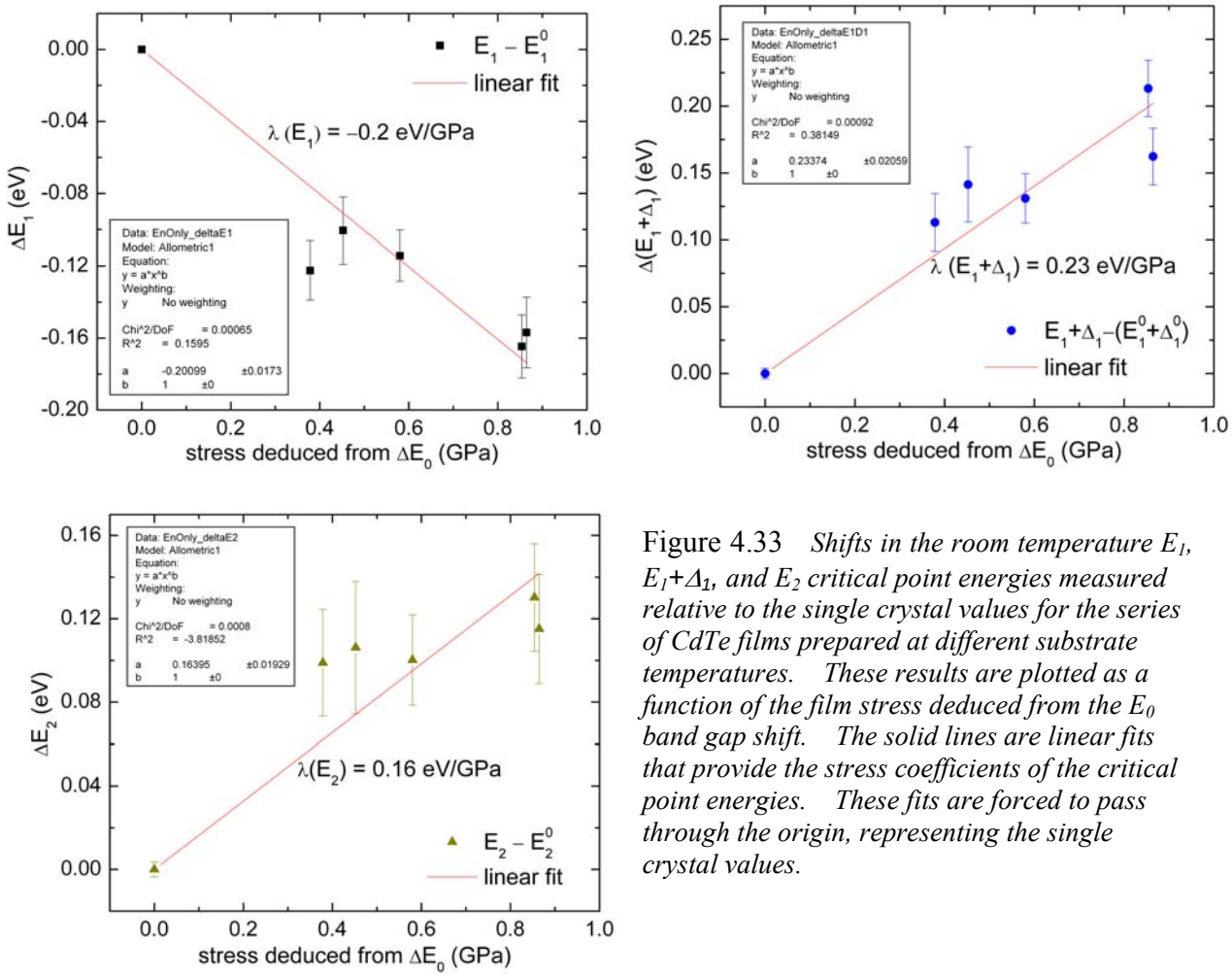

Figure 4.33 *Shifts in the room temperature E_1, $E_1+\Delta_1$, and E_2 critical point energies measured relative to the single crystal values for the series of CdTe films prepared at different substrate temperatures. These results are plotted as a function of the film stress deduced from the E_0 band gap shift. The solid lines are linear fits that provide the stress coefficients of the critical point energies. These fits are forced to pass through the origin, representing the single crystal values.*

Several observations support the validity of the trend in Figure 4.32, if not the absolute values. For deposition temperatures above 220°C, the 1000 Å thick films pass through a transition whereby the stress decreases by a factor of two over a ~50°C range. The very high stress levels in the two lowest temperature films are consistent with the observed void fraction evolution. For thicknesses greater than 1000 Å, these films undergo abrupt structural transitions in which the void fractions increase significantly. For the two higher temperature films, the void fraction in the thin film regime is higher and no structural transition is observed. Thus a high initial stress in Figure 4.32 is correlated with the appearance of a subsequent microstructural transition in the evolving film. Previous studies have indicated that for sputtered films deposited at different substrate temperatures, similar stress magnitudes are observed as those in Figure 4.32, and a transition to lower stress is also observed at a substrate temperature equal to 1/3 the melting temperature of the sputtered material.[12] Presumably surface diffusion is the mechanism by which strain generated by ion bombardment is relaxed during the deposition process.

It is also important to assess the effect of strain on the three other critical points of CdTe. If a relationship between stress, and the E_1, $E_1+\Delta_1$, and E_2 critical point energies can be established, then the short penetration depth of the light at these energies (compated to E_0) enables depth profiling of the strain in the film in step-wise fashion as described earlier. Figure 4.33 shows reasonable linear trends for the three critical points, and these are now being used to evaluate stress in a depth profiling mode as described earlier. In addition, a better understanding of the nature of the strain, the role of polycrystallinity, and the direction of the polarization vector is required. It seems possible that through SE measurement, one may be able to determine the preferential orientation of crystallites through a study of the full set of critical points. For such analysis, in-depth theoretical modeling support would be needed.

A similar study of stress has been perfomed on the CdS films prepared as a function of the deposition temperature. For these films, the deduced stress is nearly constant at ~1.5 GPa, within the error bars of the measurement, as shown in Figure 4.34. This stress level is a factor of two higher than that observed for CdTe. A nearly constant, high level of stress is consistent with the observed very low void fraction in all these films. This in turn is consistent with the higher melting point suggesting that a higher substrate temperature is needed for stress relaxation in CdS through void development.

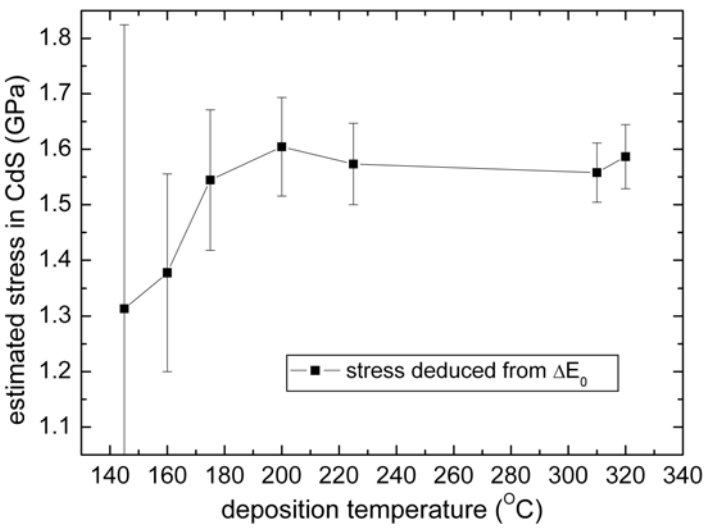

Figure 4.34 *Stress in CdS films as a function of deposition temperature. These results were estimated from the shift in the fundamental band gap E_0 from the single crystal value. The E_0 values were obtained experimentally from dielectric functions of 500 Å thick films measured in situ after cooling the newly-deposited film to room temperature.*

5. EXAFS of Light Stressed Cells with Complete Cell Structure

5.1. Introduction

In our previous studies of Cu K-edge extended x-ray absorption fine structure (EXAFS) from sputtered cells or partial cell structures, we have found that most of the ~30 Å of evaporated copper used as part of the Cu/Au back contact was found to bind with oxygen in the form of Cu_2O if the CdTe film had received a prior $CdCl_2$ treatment. However, in films without chloride treatment, copper was found to bind with tellurium primarily as Cu_2Te.[14] We have also studied Cu EXAFS in CdS polycrystalline films diffused with Cu. Those results indicated predominant scattering from sulfur neighbors (similar to the Cu-S scattering path in Cu_2S). [See our Annual Technical Report for Phase I. All these studies were done on CdTe or CdS films deposited on high purity fused silica to avoid any possible signal contamination from heavy elements such as Cu and Zn in tin-oxide-coated TEC glass. No spectra from CdTe devices with the complete structure (glass/TCO/CdS/CdTe/metal contact) were reported, or from light-soaked devices. In this section we will describe our studies of these two cases.

In order to study the local structural changes of copper in completed CdTe cells under light-stressed conditions, we prepared sputter-deposited CdS and CdTe layers on fused silica substrates. With this structure, a built-in field at the p-n junction is established which is expected to affect the diffusion of copper atoms through CdTe into CdS, yet without x-ray fluorescence contamination from regular glass. [Although we have used Al-doped ZnO as a front contact, it is inappropriate for this study because the photon energy of the Zn K_α fluorescence signal at 8639 eV is very close to the 8048 eV of Cu K_α. We have found previously that the Zn fluorescence can affect the Cu detection capability of the high purity Ge detector at MRCAT beamline at the Argonne APS.]

In Phase I, we reported Cu K-edge EXAFS from complete CdTe solar cell structures. A strong peak arising from the Cu-O bond in $\chi(R)$ spectrum was observed. However, there were two other peaks around 2Å and 2.74Å which were undetermined at the time we reported, due to lack of reference structure. Instructed by our x-ray fluorescence study of peeled-off Au contact layer (Phase I Quarter 3 report) and our recontact study (Phase II Quarter 2 report), we hypothesized that these two peaks might arise from Cu/Au alloys. This hypothesis was confirmed by our High Resolution Transmission Electron Microscopy images and small spot EDS spectra. (See Section 6 below.)

Our experimental and theoretical modeling results on Cu K-edge EXAFS studies of as-grown and light-stressed complete CdTe cells are described here.

5.2. Sample preparation

We prepared standard cells on TEC 7 glass and also CdS/CdTe/metal contact structures with the same thicknesses on fused silica. The thicknesses of CdS and CdTe are 0.13 and 2.3 μm, respectively. Deposition was carried out in 18 mTorr Ar at 250 °C without vacuum break between the n-type and p-type layer depositions. Film growths on the two different substrates were finished in separate but consecutive depositions, instead of side-by-side, because of different emissivity of the two substrates. Standard vapor $CdCl_2$ treatment was carried out, followed with 35Å Cu and 200 Å Au depositions by evaporation onto the room temperature

substrates to form dot cells with 0.15 cm^2 contact area. The process was finished with 45 minute heating in room air at 150 °C for back-contact diffusion/activation. (Except for the CdS and CdTe depositions, all processes were carried out on both types of samples (TEC 7 and fused silica) side by side.) In order to have the samples on fused silica for EXAFS going through the whole process including light soaking equivalent to the complete cells on TEC 7, we cut the finished samples into six groups for the side-by-side light soaking. The six groups of samples were light-soaked continuously for different periods: 0 (no light soaking), 0.5, 1, 2 , 4 and 5 days. Samples were light soaked under a Xe lamp with 1 sun power density. The temperature of the samples was around 70 °C under the illumination. During light soaking, the samples were left at open circuit, without encapsulation, and with no control of humidity. (We wanted to enhance degradation during the limited beam time available for the run.) EXAFS data were collected from the CdS/CdTe/Cu/Au samples on fused silica and the corresponding J-V data were measured on the complete sister cells on TEC 7, which had initial efficiencies averaging 11.5%. Table 5.1 and Fig. 5.1 summarize the average efficiencies of 9 cells each group before and after different light soaking periods. The energy conversion efficiencies are the average of 9 cells of each group.

Table 5.1 Cell efficiencies vs. light soaking time

Light soaking(days)	Ave. Initial η(%)	Ave. Final η(%)
0	11.4 ± 0.4	11.3 ± 0.3
0.5	11.2 ± 0.2	9.9 ± 0.4
1	11.1 ± 0.5	9.8 ± 0.3
2	11.6 ± 0.7	9.1 ± 0.4
4	10.2 ± 0.5	7.2 ± 0.4
5	10.2 ± 0.2	6.8 ± 0.7

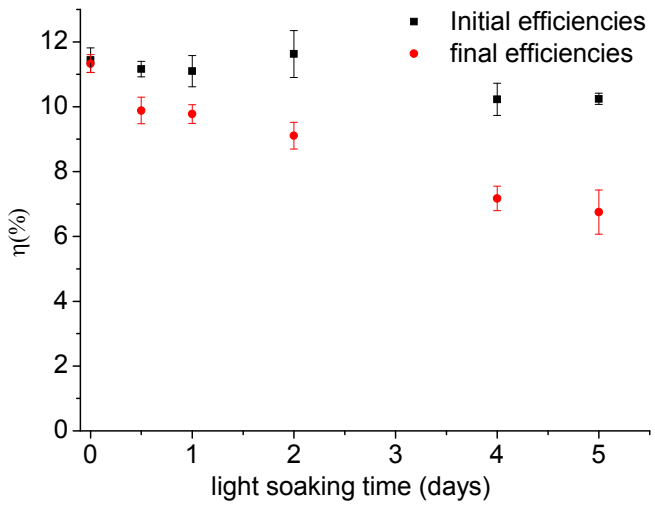

Fig. 5.1 Change of energy efficiencies from the initial performance. Note that different cells were used for each datum point and the bars represent the r.m.s. dispersion among 9 cells.

Due to the limitation of available beam time, we were only able to collect data from three sister samples (on fused silica) – 0, 2 and 5 days stressed and the results are discussed below.

5.3. Cu_2O and Cu/Au alloy in cells before and after light soaking

After data extraction, the modulus of the phase-uncorrected radial distribution functions, $|\chi(R)|$, of the as-grown sample (no light soaking) and the 2-day and 5-day light-soaked samples are plotted in Figure 5.2. For comparison, the spectrum of a powder Cu_2O reference is also plotted. The major peak at 1.47Å arises from the first nearest neighbor oxygen atom, equivalent to the Cu_2O structure, in both the fresh cell and light soaked ones. The peak width is different from that of Cu_2O, but the real and imaginary parts of the $\chi(R)$ function (Figure 5.2 b and c) in the region from 1.2 Å through 1.7 Å indicate this broadening is due to scattering intensity leakage from the other two peaks at 2.0 Å and 2.73 Å.

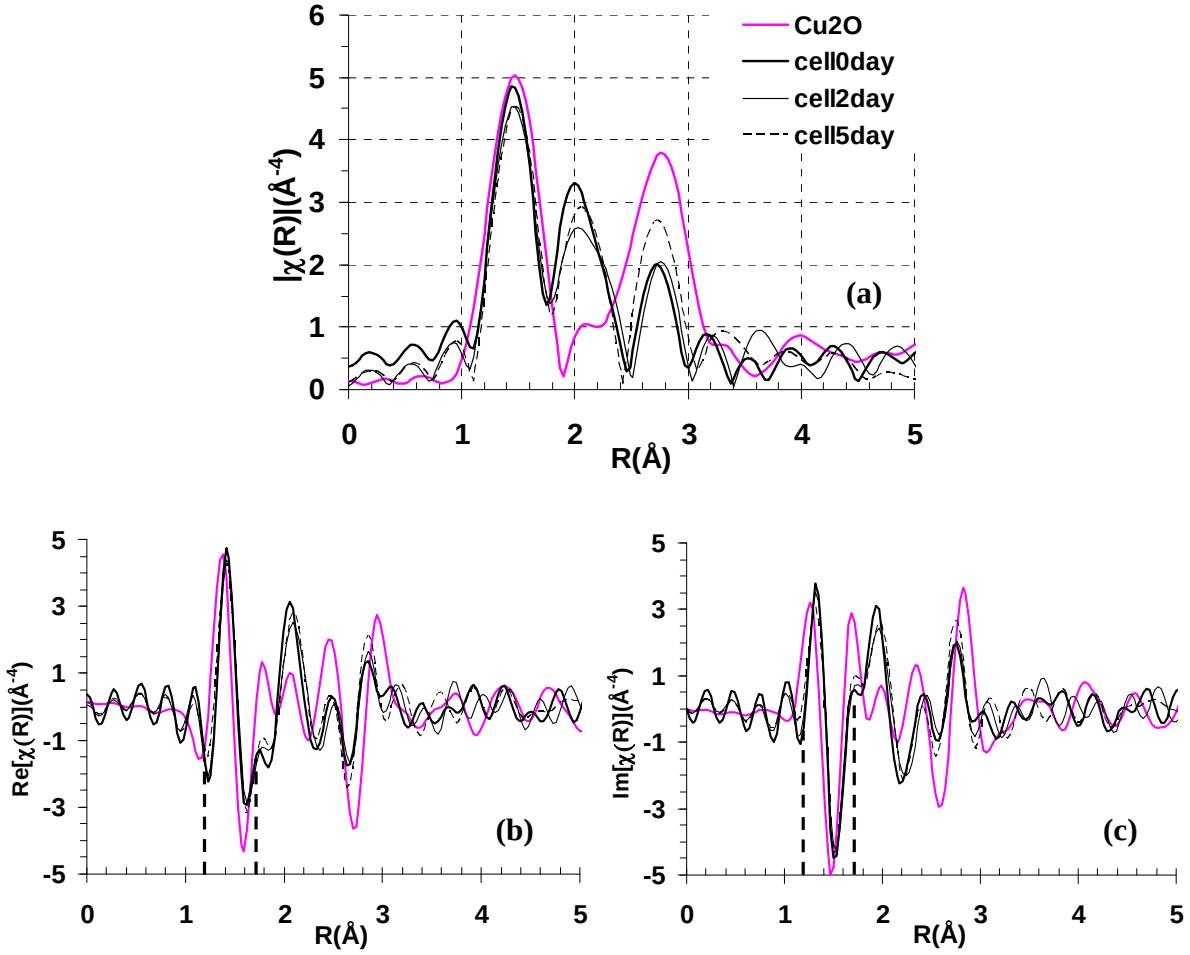

Figure 5.2 $\chi(R)$ functions of light soaked sample and Cu_2O reference.

Copper is a fast diffuser in CdTe crystals, and diffuses even faster along grain boundaries. In the complete cell structure, copper may accumulate in the CdS layer via diffusion from the back contact through the CdTe during the back-contact activation and during light stressing. This is suspected as a major degradation mechanism for CdTe solar cells under light-stressed conditions. Therefore, we have considered the possibility of sulfur neighbors as candidates for one of the two peaks at 2.0 Å and 2.73 Å. However, by comparing the imaginary and real parts of the $\chi(R)$ functions with those of the Cu_2S powder reference (not shown in this report), we conclude that neither of the two peaks could be due to scattering from sulfur neighbors such as the Cu-S scattering path observed in pure CdS.

These two peaks at 2.0 Å and 2.73 Å are also not generated from scattering by tellurium (as in Cu_2Te), chlorine (as in CuCl or $CuCl_2$), or copper (as in metal Cu crystal) neighbors. But given the small amount of Cu in the sample and the finite sensitivity of the x-ray detector, we cannot conclude that Cu_2S and Cu_2Te do not exist in the cell at low levels. What appear in the EXAFS spectra in this case should be the dominant chemical phases of copper in the samples. These are Cu_2O and Cu-Au as discussed below.

Model fits to the two EXAFS peaks was instructed by our x-ray fluorescence study of peeled-off Au contact layers, by the recontact study and by our HRTEM images. Scattering paths of Cu-Au and Cu-Cu from a model structure of the ordered 50:50 Cu-Au alloy[15] are fitted to the spectrum together with the Cu-O path from a Cu_2O reference. The model structure of Cu-Au alloy is a distorted FCC structure with space group P4/mmm and lattice constants: a = b = 3.966 Å, c = 3.673 Å. In this structure, the first nearest neighbor shell around Cu consists of eight Au atoms at a distance of 2.70 Å and the 2nd nearest neighbor shell is four Cu atoms at 2.80 Å. The structure of the unit cell of this Cu-Au alloy crystal is plotted in Figure 5.3. Our fitting gives the Cu-Au and Cu-Cu path lengths of 2.59 Å and 2.63 Å, respectively (Table 5.2). The coordination number of the Au and Cu neighbor shell provided in the theoretical fitting is 11.9 and 0.9 respectively. This may suggest that the Cu in the Au layer is substitutional on Au sites in the FCC gold structure, in which there would be 12 Au first neighbor atoms at 2.88 Å around the Cu.

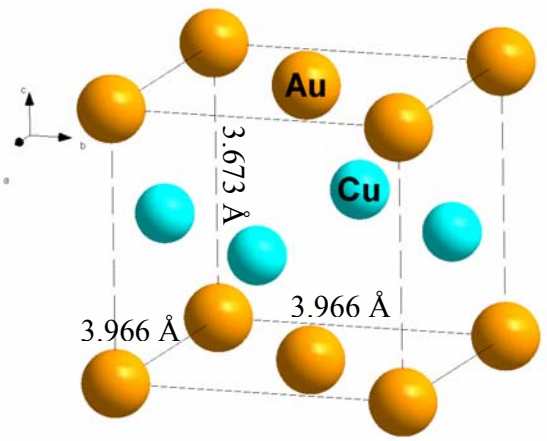

Figure 5.3 Unit cell of Cu-Au alloy crystal

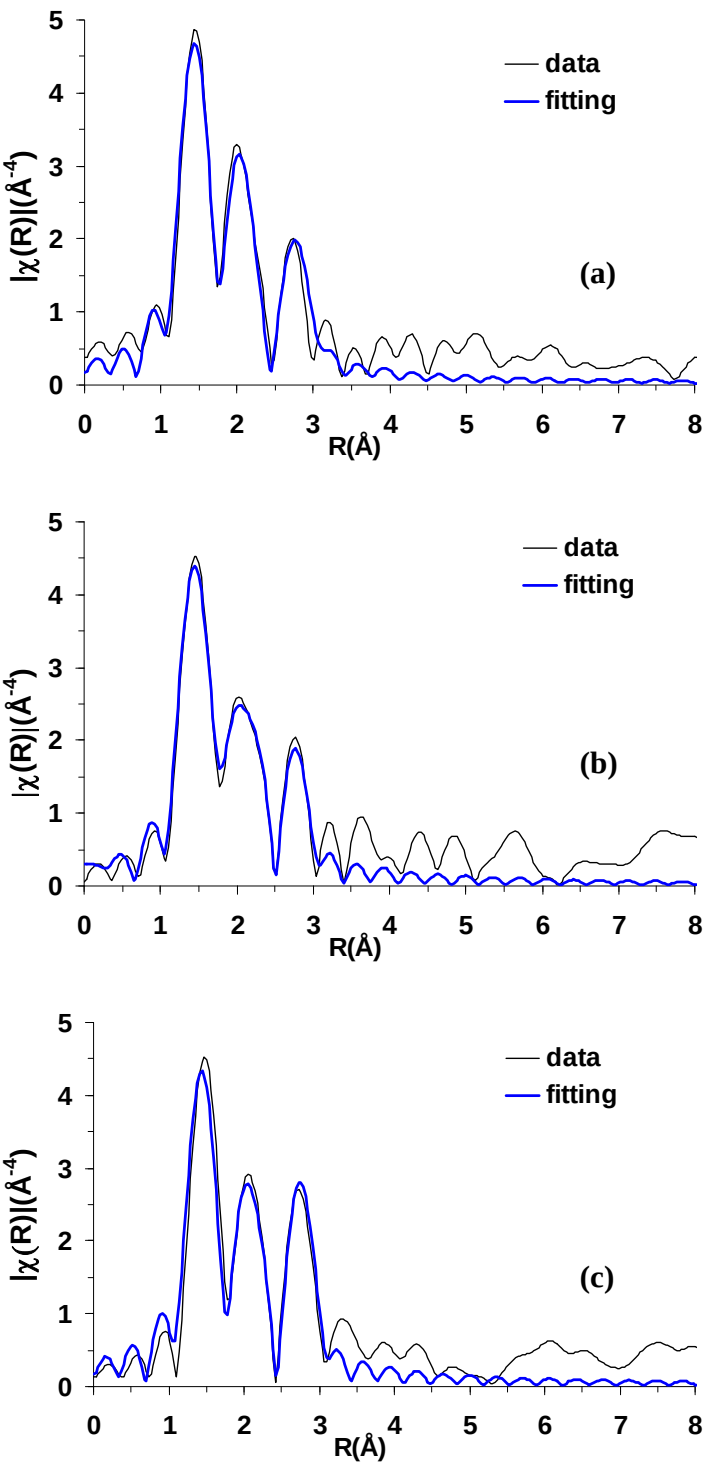

Figure 5.4 Theoretical fitting and experimental EXAFS data of complete cell structure. (a) fresh cell; (b) 2-day light soaked; (c) 5-day light soaked.

As mentioned in our third quarterly report of Phase II, an explanation of the shift of the Cu-Au bond length might be that the amount of copper diffused into the Au layer is too small to form Cu-Au alloy. Instead of forming the true Cu-Au alloy, the copper atoms may locate at the grain boundary of the polycrystalline Au layer. Lattice dislocation of Au can be clearly seen in the HRTEM image as shown in Figure 6.1. Assuming 30 Å of Cu diffused into Au and uniformly distributed along the surface of Au crystal grains, which can be assumed with 10Å diameter in average, then the thickness of the Cu layer covering Au grain surface is only ~0.75 Å. This is not even thick enough to form a monolayer and can explain the small coordination number obtained for the fit to the Cu-Cu path. Meanwhile, pressure due to lattice dislocation of Au may explain the distorted bond lengths of the Cu-Au and Cu-Cu paths.

In the EXAFS spectra from cells after light soaking (for 2 and 5 days, respectively), all three peaks at 1.47, 2.0 and 2.73 Å are observed although the intensities change (Figure 5.2a and Figure 5.4). Numerical fitting indicates that the intensities of the 1.47 Å and 2.0 Å peaks drop mostly due to a decrease in the coordination number of oxygen shell. As summarized in Table 5.2, for both the 2 and 5 days light-soaked samples, the number N of the oxygen and gold atoms in these shells decrease to 1.3 and 11.2, respectively from 1.4 and 11.9 in a fresh cell. This may suggest loss of oxygen atoms from the Cu_2O phase during light soaking. For the 2-day stressed sample, there is no obvious change for coordination number - N and scattering path length - R, besides the decrease of N's.

Table 5.2 Fitting of EXAFS spectra of complete cell structure before and after light soaking.

bond scattering	N	ΔN (+/-)	R(Å)	ΔR(±)	σ^2 (10^{-3}Å)	$\Delta\sigma^2$($\pm10^{-3}$Å)	ΔE_o
0 day stressed							
Cu - O (Cu_20)	**1.4**	0.3	**1.84**	0.02	2	fixed	
Cu - Au (CuAu)	**11.9**	3.0	**2.59**	0.06	21	8	-3.07±4.09
Cu - Cu (CuAu)	**0.9**	0.22	**2.63**	0.11	12	13	
2 day stressed							
Cu - O (Cu_20)	**1.3**	0.3	**1.85**	0.02	2	fixed	
Cu - Au (CuAu)	**11.2**	2.9	**2.59**	0.05	20	8	-3.26±3.23
Cu - Cu (CuAu)	**0.9**	0.23	**2.66**	0.06	7	5	
5 day stressed							
Cu - O (Cu_20)	**1.3**	0.3	**1.85**	0.01	2	fixed	
Cu - Au (CuAu)	**8.5**	2.2	**2.65**	0.03	15	3	0.75±1.98
Cu - Cu (CuAu)	**3.0**	0.8	**2.81**	0.06	19	fixed	
Cu_2O							
Cu - O (Cu_20)	**1.5**	0.39	**1.84**	0.004	1.6	0.9	8.31±0.32
Cu - Cu (Cu_20)	20.1	5.12	3.04	0.01	27.6	1.5	

However, a dramatic change occurs in the 5-day stressed sample. Holding the coordination number N and scattering path length R of the oxygen shell to be the same as in the 2-day stressed sample, the coordination number, N, both first neighbor Au and second neighbor Cu shells changes from 11.9 to 8.5 and from 0.9 to 3.0, respectively. The scattering lengths, R, change from 2.59 to 2.65 and from 2.63 to 2.81 Å (Table 5.2). These parameters are very close to the ones of the Cu-Au reference structure - eight Au atoms at distance 2.70 Å and the 2nd nearest one is four Cu atoms at 2.80 Å around Cu atom (Figure 5.3).

We suggest that this indicates the formation of a 50:50 Cu-Au alloy with some Cu sites substituted by Au atoms. The structure model plotted in Figure 5.5 a and b can explain this well. Figure 5.5a shows such Cu-Au alloy layer forms in the (001) plane. But when the Cu atoms in the positions as circled in Figure 5.5 b are substituted by Au atoms, the coordination numbers of the Au neighbor shell and Cu shell around Cu atoms become 9 and 3, which matches our fitting results for the 5-day light-soaked sample. Insufficient Cu available to form the full Cu (001) plane in Cu-Au alloy structure can explain such Au atom substitutions on Cu sites. These results then suggest that the copper atoms diffused into the Au layer during back-contact activation start to precipitate into the Cu/Au alloy island structure during the 5-day light soaking. This Cu/Au alloy formation could explain the change in coordination number – N and scattering path length – R from the fresh cell to the 5-day light-soaked one.

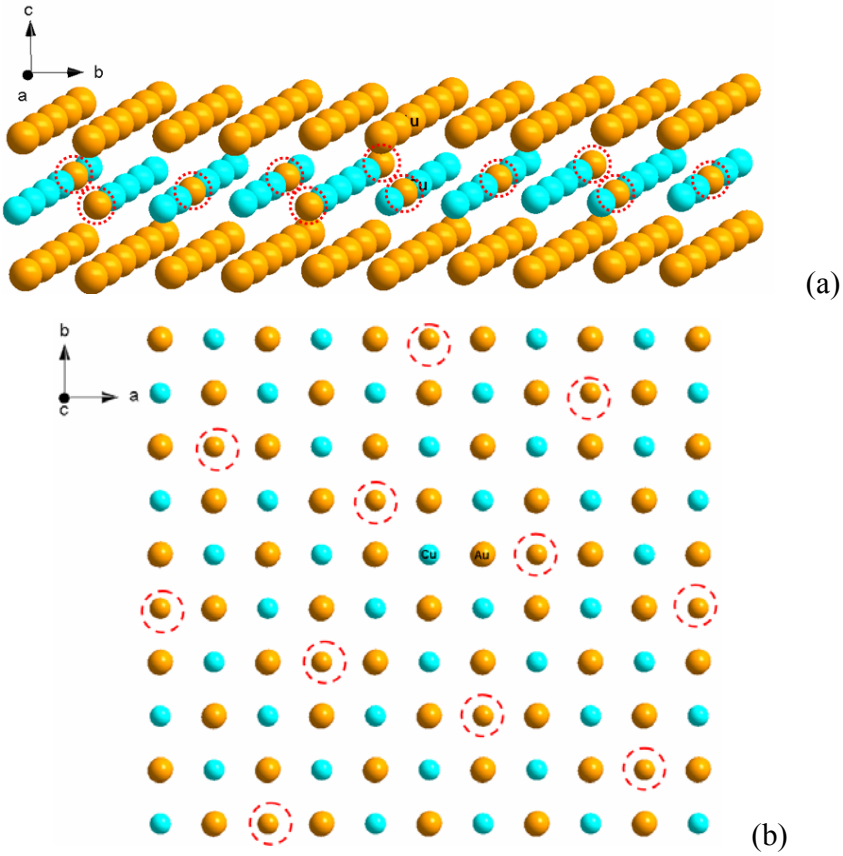

Figure 5.5 Cu-Au alloy layer in (001) direction: (a) Side view of the (001) plane, (b) top view of the (001) plane. Circled atoms are the Cu atoms in reference Cu-Au crystal which are substituted by Au atoms in our proposed model structure.

5.4. Conclusion

This EXAFS study on sister samples with structures identical to complete cells except for the TCO and different substrate confirms the existence of copper oxide in CdTe solar cells. We find that the other major chemical phase of copper in the cell structure is a Cu-Au alloy. We are currently working with fine-probe EDS spectra on the back contact region collected together with the HRTEM images to confirm the distribution of copper in the gold contact layer.

6. High Resolution Transmission Electron Microscopy near Cu/Au Back Contacts

6.1. Introduction

Through collaborations with Jeff Terry and the MRCAT beamline of the Advanced Photon Source in Argonne National Lab, the UT CdTe PV group has studied aspects of the Cu K-edge EXAFS spectrum revealing the local structure of Cu atoms in CdTe solar cells. We have identified the Cu_2O bonding structure in $CdCl_2$ treated films. However, the x-ray beam in the photon energy range (from 8.8 keV through 10 keV) penetrates completely through the 2μm CdTe cell structure and leaves questions about the location of the Cu_2O phase in the cell unresolved.

As we reported in Phase I, x-ray fluorescence data from peeled-off metal back contact layers and the remaining structures of the cells indicate 90% of the 3.5nm evaporated Cu remains in the Cu/Au back contact structure. This indicates that very little copper diffuses into CdTe after the 45 minute heating at 150 ^{o}C.

Our I-V measurement of recontacted cells confirms the significance of such interfacial copper on the cell performance. The results were reported in the 2nd quarterly report of Phase II. Our latest theoretical fitting on the EXAFS spectra of light-stressed devices, reported in Section 5 above, further suggests that diffusion of Cu into the Au layer occurs under light stressing.

A high resolution investigation into the Cu distribution in the region near the Au back contact was needed to provide better evidence of the Cu location. Such study requires nanometer scale resolution, since the evaporated Cu layer is only 3.5 nm. To obtain direct evidence of the interfacial Cu2O structure, we have used High Resolution Transmission Microscopy (HRTEM), which can provide Z-contrast imaging with point-to-point resolution of 1.7 Å together with X-ray energy dispersive spectroscopy (EDS).

6.2. High Resolution TEM and Sample preparation

In Phase II we have collaborated with Kai Sun and the Electron Microbeam Analysis Laboratory (EMAL) at the University of Michigan working on HRTEM of our rf sputtered samples. We used a JEOL 3011 ultra-high resolution microscope (~0.17nm) and a JEOL 2010F analytical electron microscope that can be operated either in TEM or STEM mode (~0.17 nm). When performed in the STEM mode, simultaneous atomic resolution HAADF (high-resolution high-angle annular dark field) image, i.e. Z-contrast imaging can be obtained. Sample preparation was done mostly at the University of Toledo with final ion beam thinning at UMich using a Gatan 691 Precision Ion Polishing System (PIPS^{TM}).

We fabricated CdS/CdTe devices by magnetron sputtering in the conventional structure on 3.2mm TEC7 glass. 0.13μm CdS and 2.3μm CdTe films were deposited without vacuum break, followed with standard $CdCl_2$ vapor treatment at 387 $^{\circ}$C for 30 minutes. As the next step, 35Å Cu and 200Å Au layers were evaporated on the top of chloride-treated films. The devices were then finished by diffusion at 150 $^{\circ}$C in ambient air for 45 minutes.

The cross-section TEM images and fine probe energy dispersive spectra (EDS) from the thinned area were collected in the JEOL 3011 system at EMAL. HRTEM imaging was performed using the JEOL3011 UHR HREM at EMAL. This microscopy has an ultra high resolution pole-piece operated at 300kV that gives a point resolution down to about 0.17 nm. The

EDS analysis was performed in the JEOL 2010F at the same lab in the STEM mode. The probe size for both imaging and EDS spectrum collection was set to 0.5nm.

6.3. Interfacial Cu-Rich Layer

Figure 6.1 shows the cross sectional Z-contrast image of the back-contact region of sputtered CdTe cells, collected in transmission mode with a point-to-point resolution of *1.7Å*. The micrograph clearly shows the lattices structures of CdTe and Au. The HRTEM image demonstrates a continuous interfacial layer with thickness of approximately 4 Å which is observed everywhere along the interface between CdTe and Au. This interfacial layer appears as the thin layer between CdTe and Au brighter than the other two in the image of Figure 6.1. Lower Z number elements in this layer produce stronger electron beam intensity collected in transmission through the material. The contrast of the images indicates this interfacial layer between CdTe/Au contains an element with Z number lower than Cd, Te and Au, which is probably copper. Fine-probe EDS spectra from CdTe, Au and the interfacial layer confirm higher copper concentration at CdTe/Au interface.

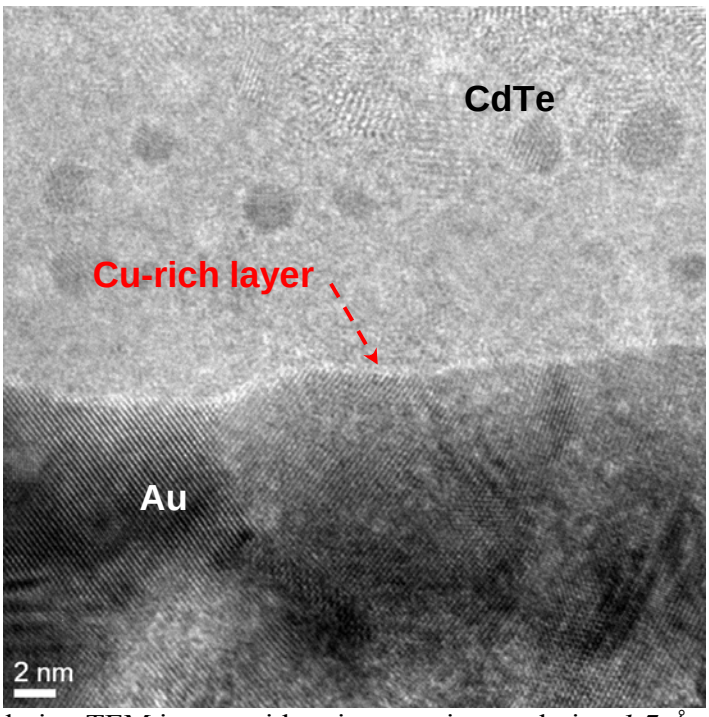

Figure 6.1 High resolution TEM image with point-to-point resolution *1.7 Å* at the CdTe/Au interface.

6.4. Distribution of Copper Near the Back Contact Region

Fine-probe EDS spectra across this interfacial layer were then collected to plot the distribution of Cu near the back contact. The 200 keV electron beam was defocused to around 0.5 nm to reduce possible beam damage of the sample due to long exposure to high beam current (usually several tens to 100 nA).

Cu fluorescence intensities are compared from the Au layer (spot labeled EDS-1) and from the CdTe grain boundary (GB) about 500nm away from the back contact (spot labeled EDS-2) in Figure 6.2a. The EDS spectra (Figure 6.3i) of these two positions show that the Cu K_α peak intensity (at 8048eV) from the CdTe grain boundary is below the sensitivity of the detector, whereas the Cu K_α Au layer shows a weak but significant intensity. Intensity ratios of Cu and Mo K_α peaks were calculated and compared to determine the relative Cu concentration as summarized in Table 6.1. [We chose to use the Mo K_α peak as the intensity reference in this study. The Mo K_α fluorescence is generated from the Mo ring by the excitation of scattered electrons, which is expected to be independent of the sample surface texture or thickness variation of the position where EDS signal was collected.]

EDS spectra were also taken at several positions across the Au and Cu-rich layers and into the CdTe. As shown in Figure 6.2b, the spectra were collected on spots aligned along the direction of a grain boundary. For the two positions in the Au layer (spots EDS-b and EDS-c in Figure 6.2b, the Cu/Mo ratios are 1.61 and 1.73, respectively (Figure 6.3ii), which is close to the value (1.44) of EDS-1. The most interesting result of this work is the Cu peak intensity from the position EDS-a at the interface between the Cu/Au layer and the CdTe, as shown in Figure 6.3iii. The Cu/Mo intensity ratio of EDS-a is 2.24, the *highest* among all the positions. Entering the CdTe layer, EDS from the three positions – EDS-e, EDS-d, and EDS-f indicates a sudden drop of Cu fluorescence signal (Figure 6.3iv). Increasing distance from back contact yields weaker Cu signals. The Cu/Mo ratios of positions e and d are 0.32 and 0.27, respectively (Table 6.1). The Cu signal at position f, located at the grain boundary only 70 nm away from Au contact, is undetectable. This confirms the observation at position EDS-2 in Figure 6.3a.

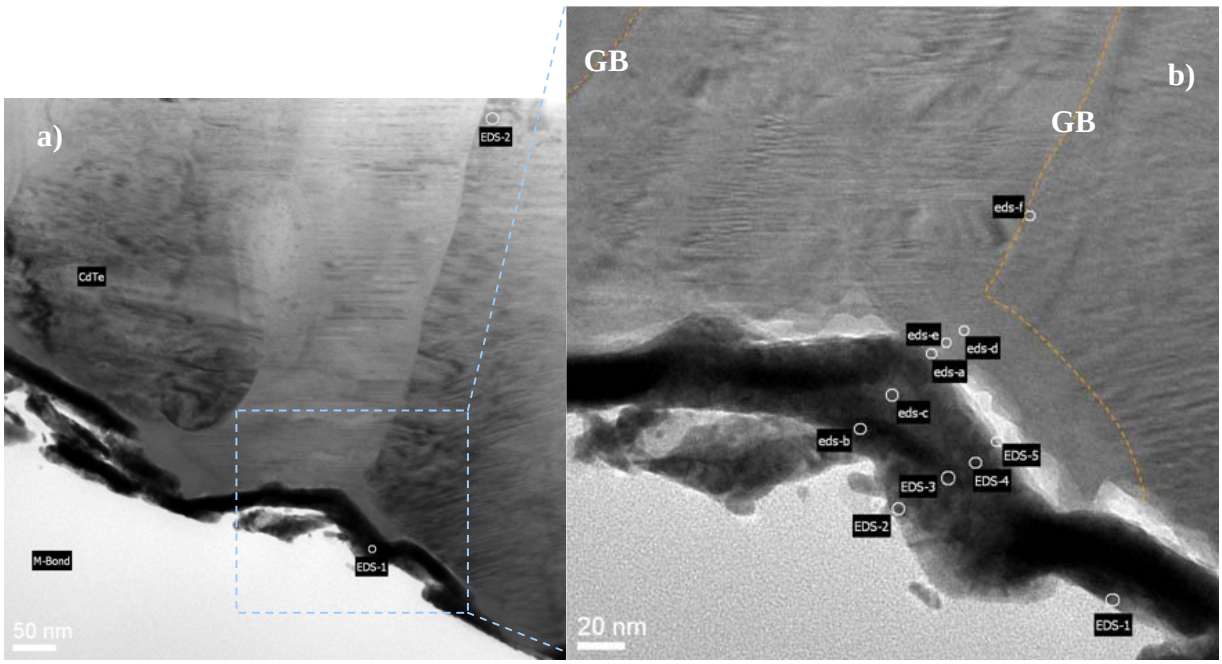

Figure 6.2 Cross-section TEM image of CdTe and Au layer. Circles are the locations where the fine-probe EDS spectra were taken.

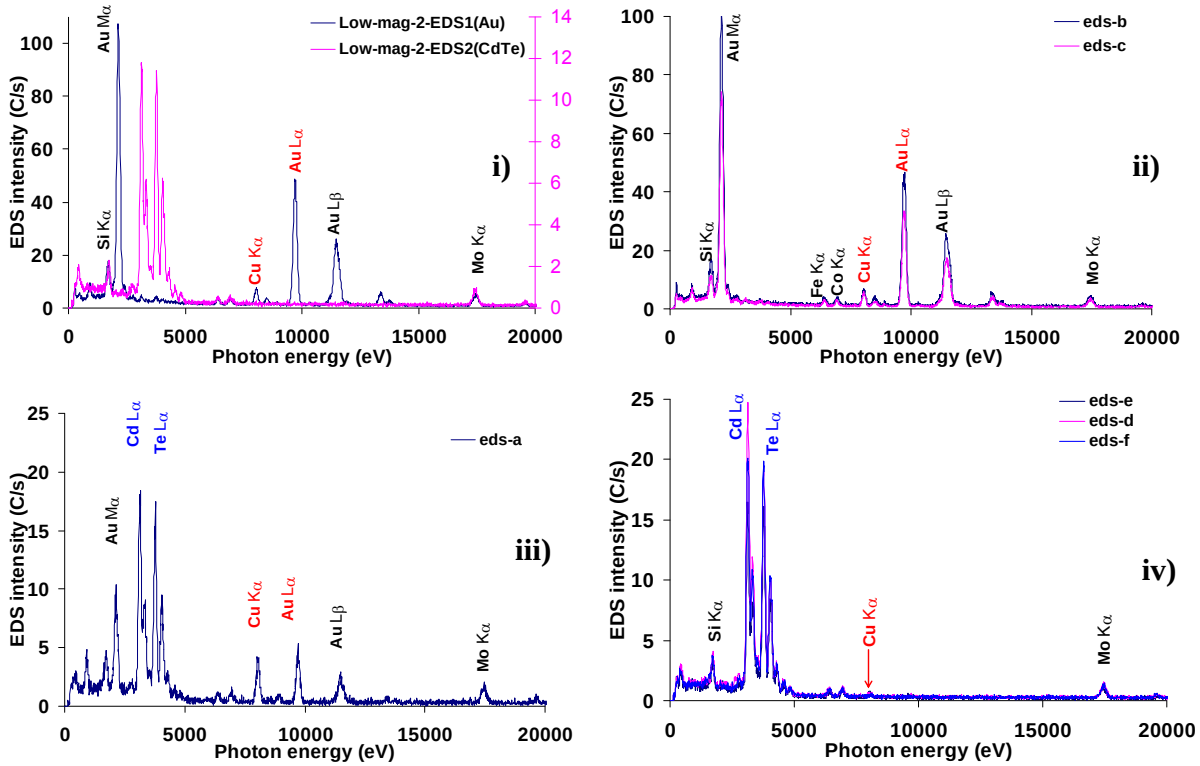

Figure 6.3 Fine-probe EDS spectra taken at locations indicated in Figure 6.2

Table 6.1 Comparison of Cu K_α and Mo K_α intensities.

Position	Cu/Mo peak intensity ratio
EDS-1	1.44
EDS-2	0
eds-b	1.61
eds-c	1.73
eds-a	**2.24**
eds-e	0.32
eds-d	0.27
eds-f	0

These results indicate the highest Cu concentration occurs at the CdTe/Au interface, which confirms the qualitative analysis based on image brightness of the interfacial Cu-rich layer in the high resolution TEM images (Section 6.3). These EDS spectra confirm that interdiffusion is occurring between the Cu and Au layers as concluded from our theoretical fitting of the EXAFS data from complete cell structure. (See Section 5.) The HRTEM and fine-probe EDS directly show the high concentration of copper at the CdTe/Au interface and in the Au layer but any Cu in the CdTe is near the detection limit 20 nm or less from the contact/CdTe interface. There is no

evidence indicating higher Cu concentration at the CdTe grain boundary than grain interior. Although some Cu is undoubtedly present, we believe that these high resolution EDS data are not consistent with a model we proposed earlier, based on EXAFS data, in which the grain boundaries might be decorated with a monolayer or two of Cu_2O.[16]

6.5. Conclusion

Given the theoretical fitting results of EXAFS data from complete cell structures (Section 5 above) and the Z contrast of the HRTEM images at CdTe/Au interface, it is most likely that the interfacial Cu-rich layer should be a copper-oxide layer with approximate thickness of 4Å. Since the Cu-O and Cu-Cu bond lengths in Cu_2O are 1.85 Å and 3.02 Å, respectively, such a presumed 4 Å Cu_2O layer is so thin that not more than two Cu-O layers could be formed in this layer. This may also explain the absence of Cu-Cu bond in our EXAFS spectra.

This high resolution cross-sectional TEM investigation on a sputtered CdTe cell at the CdTe/Cu/Au back contact interface indicates the existence of interfacial Cu_2O. We suggest that the copper-oxide layer formed at the CdTe/Au interface might serve to inhibit diffusion of copper into the CdTe layer for the case in which the CdTe has received a $CdCl_2$ treatment prior to the application of the Cu/Au back contact.

Further work on this interfacial copper-oxide layer will be focused on the stability of this layer under stressed condition. Additional TEM as well as fine-probe EDS and electron energy loss spectroscopy (EELS) investigations on light soaked cells are planned in Phase III.

7. Bifacial Transparent Back Contacts

7.1. Introduction

Transparent back contacts are useful for at least two reasons. First, if the transparent back contact is a p+/n+ structure, then it would be identical to a recombination junction in a monolithically integrated double junction tandem cell. It is possible to make a single junction cell that is the only the top half of such a cell, and optimize this top half separately.

Secondly, not only do transparent back contacts allow characterization from the "sunny" (also called front) side, as usual in solar cells, but they also allow characterization from the contact (back) side to further illuminate the internal physics of the device.

During this phase, we studied CdS/CdTe solar cells with 2.3 μm CdTe (our standard laboratory thickness) prepared with four different types of p+/n+ transparent back contacts (TBCs). We have used ZnTe:Cu and ZnTe:N as the p-type materials, and ZnO:Al and Indium Tin Oxide (ITO) as the n-type materials. This gives rise to four possible combinations ZnTe:Cu/ZnO:Al, ZnTe:N/ZnO:Al, ZnTe:Cu/ITO, and ZnTe:N/ITO. ZnTe:N/ITO was found to give the best results. This back contact was then used to make cells of lesser (1.8 μm and 0.7 μm) CdTe thickness, in those cases giving good performance up to 9.1% efficiency. Bifacial J-V and QE was performed on all cells with the optimum ZnTe:N/ITO back contact.

We characterized cell performance with current-voltage and quantum efficiency measurements, using either front or back side illumination. Figure 7.1 shows the cell structure and the direction light enters the structure in the case of front or back side illumination.

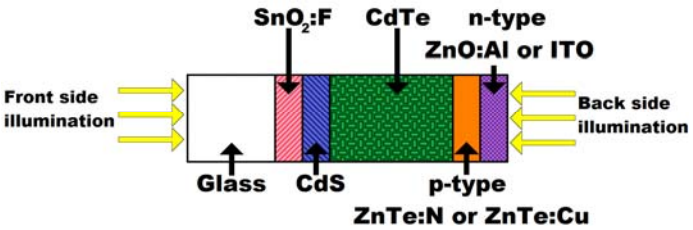

Figure 7.1 Cell structure and meaning of front and back side illumination

All cells were prepared on commercially available Pilkington TEC 7 brand fluorine-doped tin-oxide-coated soda-lime glass. All subsequent layers were deposited with RF sputtering and, excepting the reactively sputtered ZnTe:N, in pure argon atmospheres. CdS and CdTe were deposited at 250°C and 18 mTorr argon pressure. CdS and CdTe were deposited with 35 and 20 watts rf power, respectively. All samples used nominally the same 0.13 μm thickness of CdS. After CdS/CdTe deposition, 2.3 μm samples were $CdCl_2$ treated at 387°C for 30 minutes. Samples with CdTe of lesser thicknesses were treated for a time proportional to their thickness. After $CdCl_2$ treatment, either ZnTe:N was deposited by using an undoped ZnTe target and reactively sputtering in a 5% nitrogen-95% argon environment, or ZnTe:Cu was deposited by using a target doped with 2% copper by weight. In both cases, the layer was deposited with a substrate temperature of 325°C. We finally deposited an n-type transparent conductive oxide, ITO or ZnO:Al. The ITO target was 90% In_2O_3 and 10% SnO_2 by weight. For the ZnTe:Cu/ITO contact, ITO was deposited at 150°C. For the ZnTe:N/ITO contact, ITO was

deposited at various temperatures. The ZnO:Al target was doped with 2% Al_2O_3 by weight. ZnO:Al was deposited at 200°C.

7.2. Performance of 2.3 μm Cells with Different Back Contacts

Figure 7.2a shows the J-V curves (with standard front illumination) for cells with ZnO:Al as the n-type contact. Of the contacts used in our study, ZnTe:N/ZnO:Al gives the worst performance, with open circuit voltage being particularly poor. While the ZnTe:Cu/ZnO:Al contact has a reasonable open circuit voltage, typical of CdTe cells containing copper, the large series resistance (23 ohm-cm^2) decreases the fill factor, which is the greatest limitation to its efficiency as compared to ZnTe:N/ITO cells. (See below.)

(a) (b)

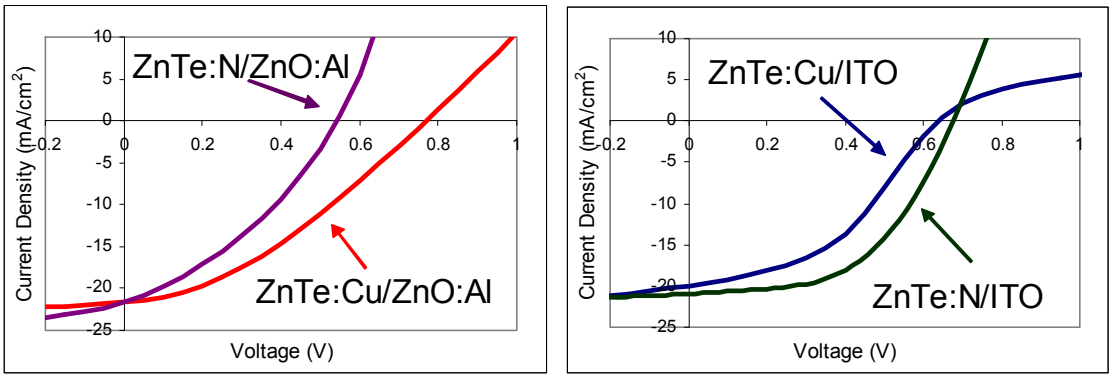

Figure 7.2 J-V data for cells with 2.3 μm CdTe, illuminated from the front side. (a), with ZnO:Al as the n-type contact. (b), with ITO as the n-type contact.

Figure 7.2b shows the J-V curves for cells with ITO as the n-type contact. For cells with ZnTe:Cu as the p-type layer, the most dramatic difference here from the cells with ZnO:Al is the rollover in the first quadrant in the ITO case. This is typical of a back contact barrier that can result from poor valence band alignment at the back contact. ZnTe:N/ITO gives the best overall results.

The parameters and performances of the best cells with each back contact are summarized in Table 7.1.

Table 7.1 Summary of efficiency and second-order metrics for 2.3 μm CdTe cells.

Back Contact	Voc (mV)	Jsc (mA/cm^2)	Fill Factor (%)	Efficiency (%)
ZnTe:Cu/ZnO:Al	762	20.8	38	6.1
ZnTe:Cu/ITO	640	17.7	43	4.9
ZnTe:N/ZnO:Al	543	21.6	35	4.1
ZnTe:N/ITO	676	21	53	7.5

7.3. Effect of ITO Deposition Temperature

The conductivity of sputtered ITO can be controlled with substrate temperature during deposition. Figure 7.3 shows the increase in conductivity, over three orders of magnitude, of ITO films deposited on glass when the substrate temperature increases from 25 °C to 300 °C.

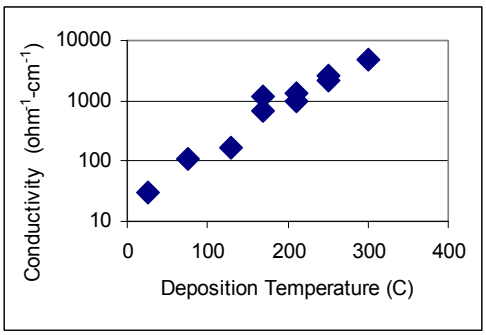

Figure 7.3 Variation of ITO conductivity with deposition temperature.

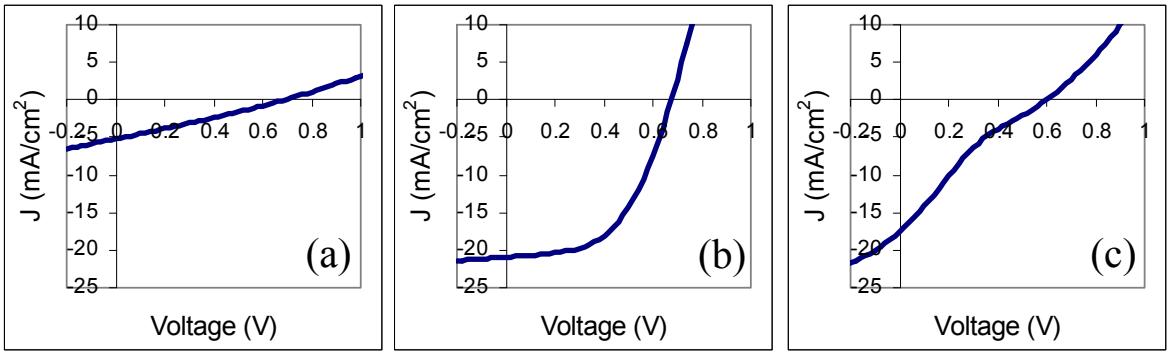

Figure 7.4 J-V curves of CdTe/ZnTe:N/ITO cells using (a) low temperature and conductivity, (b) medium temperature and conductivity, and (c) high temperature and conductivity ITO.

Although intuitively one might expect the best solar cells to use transparent back contacts with the greatest conductivity, we have observed that this is not necessarily the case. Figure 7.4 shows J-V curves (using front illumination) of 2.3 μm CdTe and a ZnTe:N/ITO back contact for various ITO deposition temperatures. For low deposition temperature (50°C) ITO (Figure 7.4a), the open-circuit voltage is similar to the middle and high temperature cases, but efficiency is limited by large series resistance, lowering short-circuit current and reducing fill factor to essentially 25%. In the case of medium temperature deposition (170°C), good overall parameters are obtained. When the temperature is increased to the high temperature (300°C) regime (Figure 7.4c), the performance does not continue to increase. "Rollunder" appears in the fourth quadrant that reduces the fill factor to less than 25%. Such cells also usually have higher efficiency when illuminated from the back side than from the front. We believe these problems are not due to subjecting the entire cell to high temperature in the final stage of the deposition, for the following reasons. The previous deposition of ZnTe:N is done at even higher temperature

(325°C). It is possible to measure J-V curves through the ZnTe:N, off the ITO contacts, and while current collection is very poor, no rollunder or rollover is observed. Finally, it is possible to first deposit contacts at the high temperature condition and then perform a second deposition of contacts at medium temperature condition between the previously existing contacts, and the behavior of the different series of cells is what would be obtained with a single deposition. We speculate that the development of roll under is caused by poor band alignment between the ZnTe:N and the higher temperature deposited ITO, as the electron affinity of ITO may change with preparation conditions.

7.4. 1.8 and 0.7 μm cells with ZnTe:N/ITO as Back Contact

Although our standard CdTe cells with metal back contacts use 2.3 μm of CdTe, such thicknesses are unlikely to be useful in double-junction cells. In monolithically integrated cells, the currents produced by the top and bottom cells must be equal. This current-matching condition is easier to meet if the top cell is more transparent, and in fact thinner CdTe can transmit an appreciable fraction of above-bandgap light. Furthermore, it is possible to fabricate cells with metal contacts and as little as 0.7 μm of CdTe and achieve reasonable performance[17] comparing favorably to our best CdTe cells.[18]

With that motivation, we have fabricated cells of different CdTe thicknesses using the ZnTe:N/ITO contact found to be best for 2.3μm CdTe cells. Table 7.2 summarizes the best cell performances as a function of CdTe thickness.

Table 7.2 Summary of efficiency and second-order metrics for cells with ZnTe:N/ITO back contact.

CdTe thickness (μm)	Voc (mV)	Jsc (mA/cm^2)	Fill Factor (%)	Efficiency (%)
0.7	652	21.7	52.4	7.4
1.8	643	19.9	65.1	9.1
2.3	676	21	52.7	7.5

It is not clear why 2.3 μm CdTe cells do not give performance equal or superior to 1.8 μm CdTe cells, but it may be an issue of the relative amount of time spent optimizing the thinner cells, which would have more value in tandem structures.

7.5. Bifacial Measurements

Figure 7.5 shows J-V curves, taken with front and back illumination, of cells with 2.3 μm (A), 1.8 μm (B), and 0.7 μm (C) of CdTe, using the ZnTe:N/ITO back contact. In all cases, the cell is more efficient and has higher short-circuit current with front side illumination. With decreasing CdTe thickness, the ratio of short-circuit current with back side illumination to front side illumination increases. For the shown cells, this ratio is 0.40, 0.48, and 0.9 for the 2.3 μm, 1.8 μm, and 0.7 μm CdTe thicknesses, respectively.

The differences between the front and back illuminated short-circuit current can be understood by considering the positional dependence of electric field strength and generation

rates within a cell. A stronger electric field increases collection of photocarriers generated at that location. Figure 7.6 shows the normalized carrier generation rates produced by AM1.5 illumination, from front or back sides, within cells of varying CdTe thickness. Figure 7.6a also includes a schematic electric field showing a decrease in field strength away from the junction and the possibility of a neutral region near the back contact.

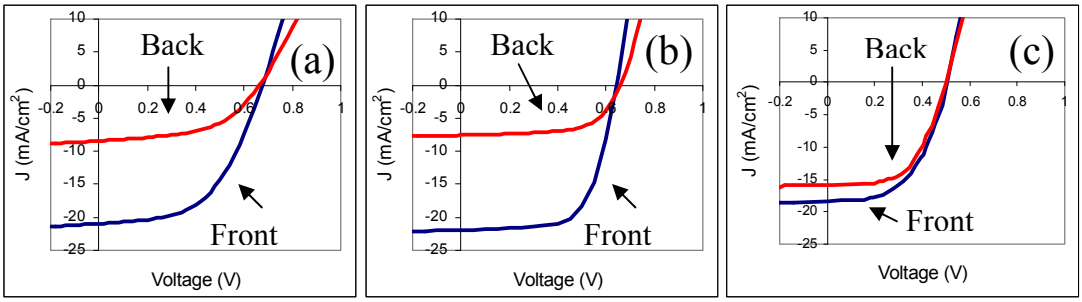

Figure 7.5 J-V curves of cells with (a) 2.3 μm, (b) 1.8 μm, and (c) 0.7 μm CdTe, using front and back illumination.

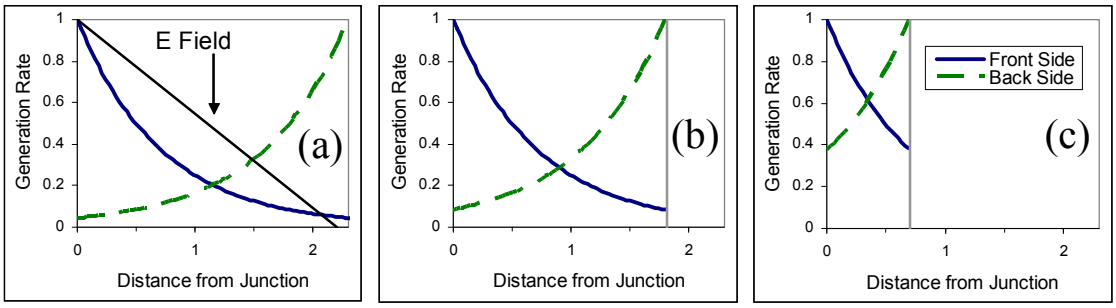

Figure 7.6 Normalized generation rates for front and back side AM1.5 illumination in the case of (a) 2.3 μm (with schematic electric field), (b) 1.8 μm, and (c) 0.7 μm CdTe cells.

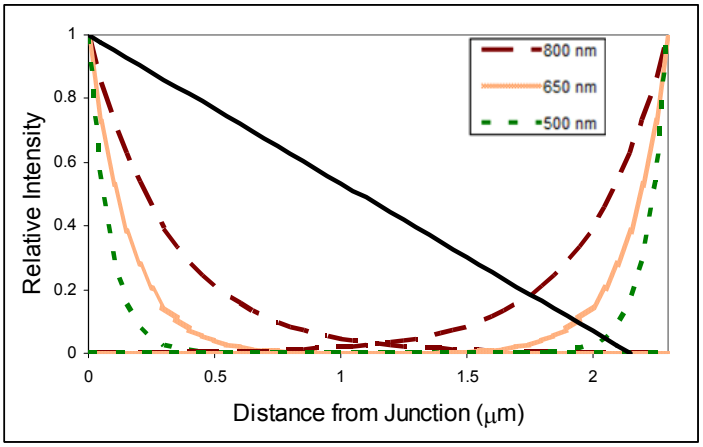

Figure 7.7 Relative intensity of 800, 650 and 500 nm light as a function of position within a 2.3 μm CdTe cell for front and back side illumination, with schematic electric field.

For front illumination and for cells of all thicknesses, the maximum generation rate is near the junction where the field strength is maximum, which leads to good collection. For back illumination, the maximum generation rate is where the field is weakest. Further, electrons generated near the back contact, as compared to those generated near the front contact, have a greater distance to travel to the CdS to become majority carriers. However, for CdTe of decreasing thickness, the back CdTe surface and point of maximum generation moves closer to the junction and strong field region, increasing the ratio of short-circuit current as measured from the back to that measured from the front.

This can be understood in even greater detail by considering bifacial quantum efficiency. While Figure 7.6 shows the generation rate due to light of all wavelengths, Figure 7.7 shows the generation rate due to three representative wavelengths.

The infrared light is absorbed most weakly. For front side illumination, this leads to a decrease in quantum efficiency towards the red end of the spectrum as CdTe thickness decreases. For back side illumination, the previous explanation, that generation is greatest where the field is weak, leads to quantum efficiency generally being lower than for front side illumination. However, now the greater penetration of red light leads to more red light reaching the strong field region, causing an upward slope in back side QE as wavelength increases. This is shown in Figure 7.8. In the case of the 0.7 mm cell (Figure 7.8), the back side QE exceeds the front side QE in the infrared and blue wavelength region. This is due to light entering from the back avoiding CdS absorption (particularly for the blue QE) and reflection from the glass substrate.

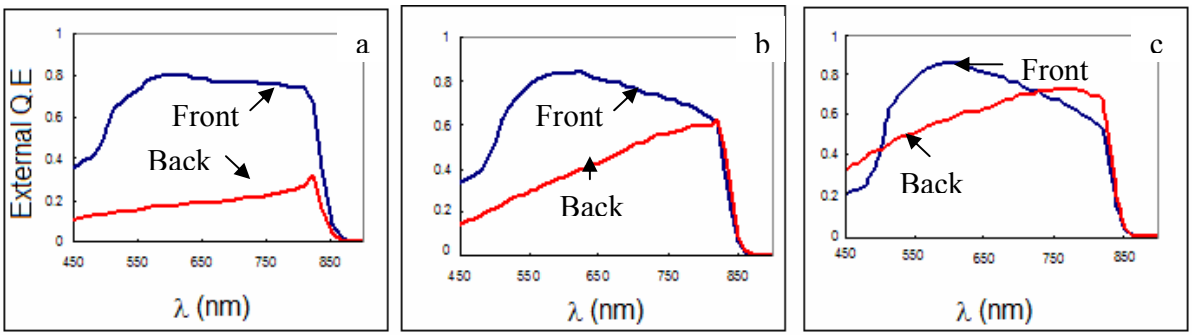

Figure 7.8 External Quantum Efficiency, measured with front and back side illumination, on (a) 2.3 μm, (b) 1.8 μm, and (b) 0.7 μm CdTe cells.

7.6. Conclusions

Among the back contacts tested in our study, ZnTe:N/ITO is found to give the best results. Our best cell with an n-type/p-type bilayer back contact is 9.1%. There is plenty of room for improvement compared to our best cell on the same TEC 7 substrate with a metal back contact, which is 12.6%, but we are optimistic that further improvements will be possible. Future work will involve other back-contact optimizations, including attempts at incorporating copper or a tellurium-rich layer. Modeling is also needed to understand band alignment issues, and to quantify future bifacial quantum efficiency results in terms of carrier lifetimes, depletion widths and neutral regions.

8. High Growth Rate Magnetron Sputtering of CdTe

8.1. Introduction

In the previous annual report (Deliverable D.1.7) and in the first quarter report (Deliverable D.2.1) of this phase we reported our investigation of the enhanced growth rates for magnetron sputtering deposition of CdTe that can be achieved with a conventional target and planar magnetron gun geometry. The deposition rate was studied as a function of sputtering gas pressure as well as RF power applied to the target. The effect of these parameters on CdTe film morphology was also studied. More recently we have studied the effect of $CdCl_2$ treatment conditions on the cells grown with different sputtering rates. The previous results are summarized, but discussion below is focused on the complete cells.

8.2. Sample Preparation and Characterization

Devices were fabricated using conditions close to our standard. Magnetron sputtering was used for the CdS/CdTe layers on TEC-7 glass. Cells were completed with Cu/Au back contacts followed by 45 minutes of diffusion activation treatment at 150 $^{\circ}$C in air. The thickness of the CdS layer was about 0.1 micron while for CdTe it was kept close to 2 micron independent of deposition conditions. The design of the vacuum chamber used for sputtering provides a distance of 3 inches between a two-inch diameter CERAC CdTe target without a backing plate and glass substrate radiatively heated up to 250 $^{\circ}$C. The system was turbomolecular pumped with a base pressure of ~$2x10^{-6}$ Torr after 60 minutes of substrate heating.

The AJA sputtering gun is water-cooled and has an unbalanced magnetron configuration. Argon was used as the sputtering gas with a pressure range from 2.5 to 50 mTorr. The range of applied RF power was from 6.6 W to 70 W with the upper limit chosen out of concern for the integrity of the unbacked target. No target damage was observed up to 70W. After the growth and before back contact formation, the structures were subjected to $CdCl_2$ vapor treatment for 30 minutes at elevated temperature, a process well-known to improve CdTe-based cell performance.[19] Treatment was done at various temperatures in order to establish the optimum temperature as a function of magnetron sputter deposition parameters.

Films were studied by the means of AFM and XRD to ensure the crystalline nature of the film and to obtain information about the grain size, orientation and residual stress in the film. Finally, complete devices were fabricated and J-V tested to determine cell efficiency and yield. Quantum efficiency (QE) measurements were done in order to study, *inter alia,* CdS/CdTe interdiffusion as a function of $CdCl_2$ treatment temperature.

For maximum sputter deposition rates, depositions have to be done at an optimum pressure which is rather specific for each individual deposition chamber. In our case it has been found that the maximum rate is achieved at an argon pressure of 5 mTorr (Figure 8.1). Increase of pressure leads to decrease of the mean free path of the sputtered species and slows the deposition rate. Extremely low pressure (<5 mTorr) eventually makes the discharge unstable and decreases the sputtering rate due to decrease of the plasma density.

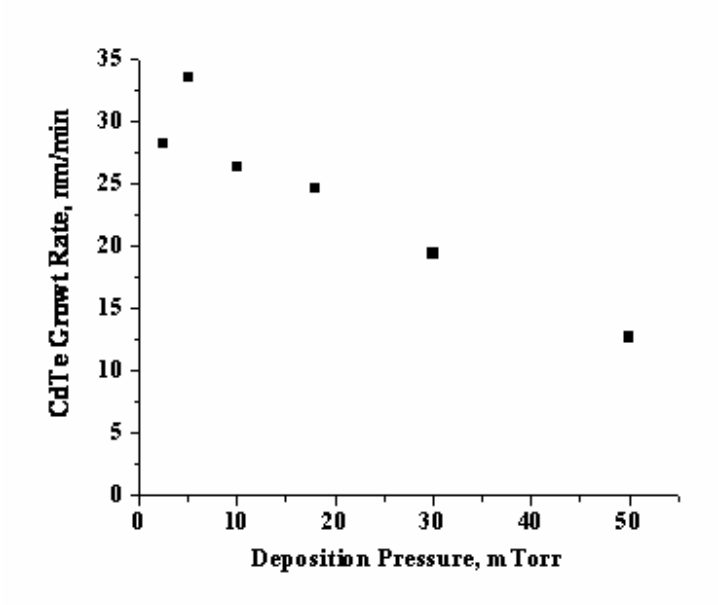

Figure 8.1 Deposition rate at 20 W of RF power as a function of argon pressure

Further, we investigated the power dependence of the deposition rate at 5 mTorr. Although the linear dependence was previously reported[20] we found it to be slightly super linear possibly due to target heating at the racetrack (Figure 8.2). Overall a deposition rate of 140 nm/min has been achieved. This corresponds to about 17 minutes of deposition for our standard 2.3 μm CdTe thickness or more a factor of 5 decrease in the time needed for fabrication of a CdTe layer in a standard 0.13 micron CdS / 2.3-micron CdTe solar cell.

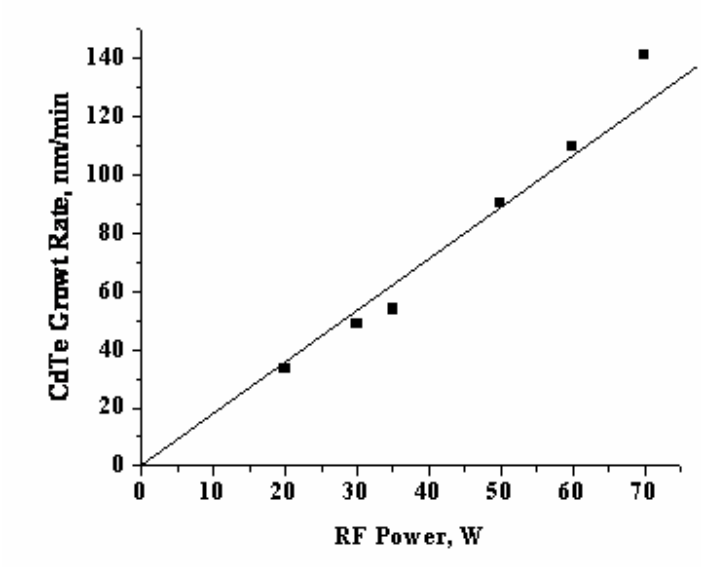

Figure 8.2 Deposition rate in 5 mT Ar as a function of RF power (linear fit is shown)

X-ray diffraction studies revealed that independent of deposition conditions, CdTe films grow as polycrystalline with preferred (111) orientation which becomes more random after

high-temperature $CdCl_2$ treatment. Figure 8.3 shows a typical result for all the deposited films. Notice a strong (111) peak at $2\theta = 23.76^o$ for an as-deposited film and the appearance of a series of peaks corresponding to regrowth in different crystallographic orientations after $CdCl_2$ treatment. These crystal structure changes were independent of film growth conditions.

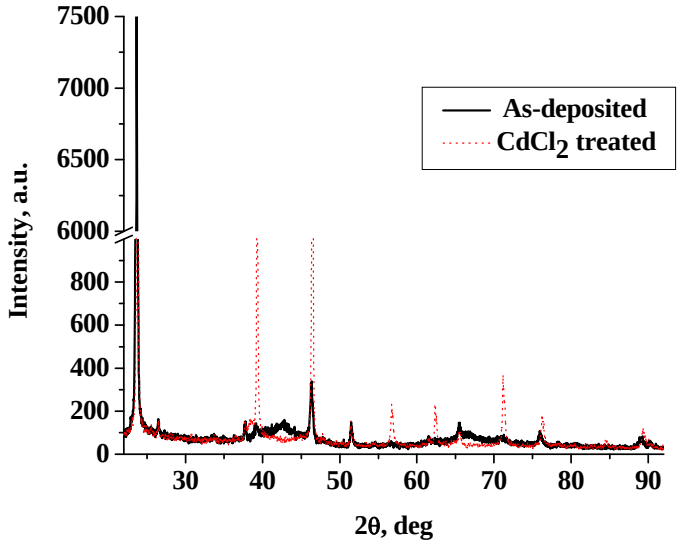

Figure 8.3 Typical XRD spectra of as-deposited and $CdCl_2$-treated films

Residual strain in as-deposited films was studied by the slight shift of the (111) peak and was described in our Phase II Quarter 1 report. Films grown at lower pressure were found to have higher in-plane compressive stress, which we associate with a denser packing of grains in the film due to a higher kinetic energy of impinging particles. Strain dependence on RF power is rather weak.

Atomic force microscopy shows a similar type of behavior with pressure and power. Morphology and surface roughness of CdTe films change significantly when deposition pressure decreases (Figure 8.4) while effect of power is rather small (Figure 8.5).

Finally, the efficiency of a set of samples grown at 10 mTorr and different RF powers (6.6 W, 20 W and 60 W) was compared with the efficiency of a cell grown at our "standard" conditions (18 mTorr, 20 W for CdTe). Figure 8.6 shows the results obtained after $CdCl_2$ treatment at different temperatures (382 $^\circ$C, 387 $^\circ$C, 397 $^\circ$C , 402 $^\circ$C ,). In all cases efficiency of at least 7% was obtained although yield varied from excellent to rather poor, especially at the extremes of $CdCl_2$ process temperatures. In many cases, though, the yield of 0.071 and 0.126 cm^2 devices was excellent, which is represented in Figure 8.6, where the average efficiency of the best 10 out of 19 cells on each sample is plotted as a function of $CdCl_2$ temperature. It can be seen from Figure 8.6 that while devices processed at standard conditions are more forgiving in terms of $CdCl_2$ treatment conditions, high-efficiency cells can be made on CdTe grown at different conditions, including high-rate conditions if the $CdCl_2$ treatment is optimized. For instance, our best high-deposition-rate cell to date has an efficiency of 11.8% which is typical of our standard cells on TEC-7 glass.

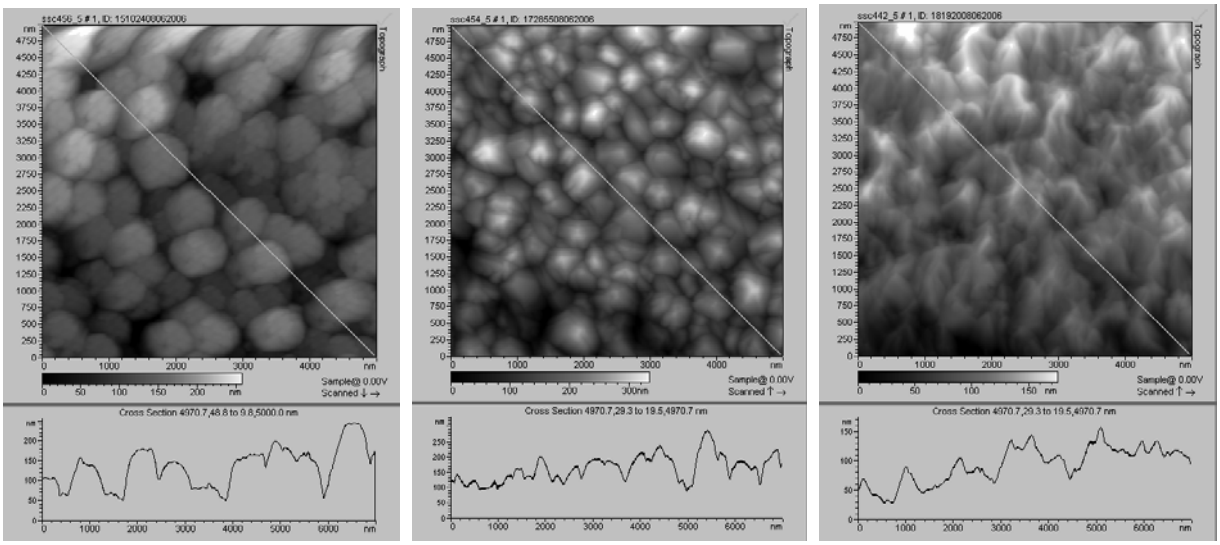

Figure 8.4 AFM images of CdTe films grown at 20W at 50 mTorr (left), 18 mTorr (middle) and 5 mTorr (right)

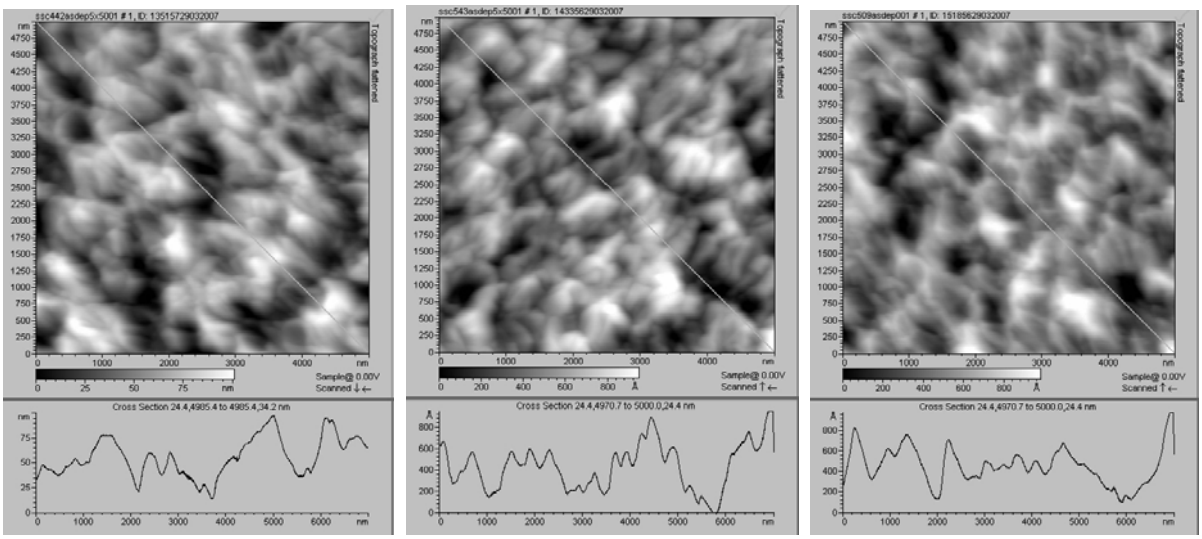

Figure 8.5 AFM images of CdTe films grown at 5 mTorr at 20 W (left), 40 W (middle) and 60 W (right)

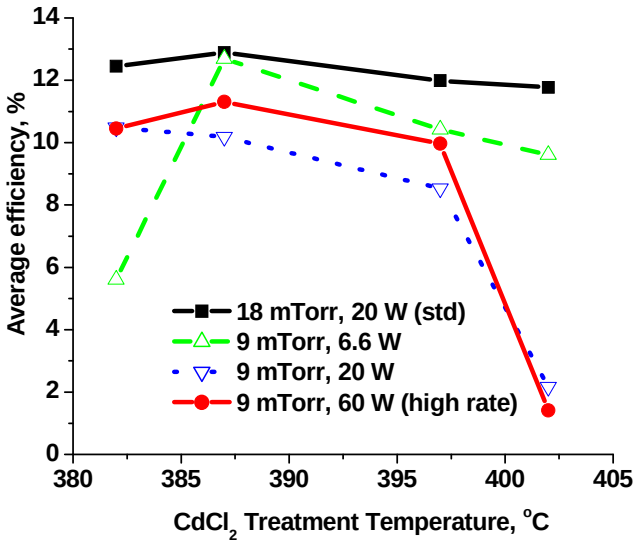

Figure 8.6 Average efficiency vs. $CdCl_2$ treatment temperature of best 50% of cells deposited at four different conditions.

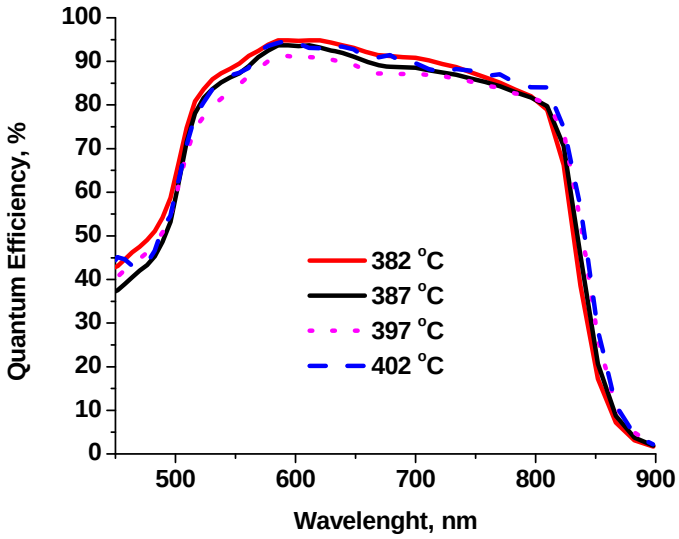

Figure 8.7 QE of the high-rate cells after $CdCl_2$ treatment at different temperatures

The QE shows evidence of slightly enhanced CdS/CdTe interdiffusion at higher chloride processing temperature (Figure 8.7), particularly evident from 530-600 nm and near 850 nm). However, these changes in carrier collection at short circuit are not the key factors responsible for the efficiency and yield of the devices. J-V data (Figure 8.8) indicate that the lower efficiency of the devices deposited at lower pressure, including the high-rate deposited cells, is due to lower V_{oc} and fill factor. We think this may be due to the smaller grain sizes and corresponding larger grain boundary area and thus higher recombination rates in these cells deposited at low pressure.

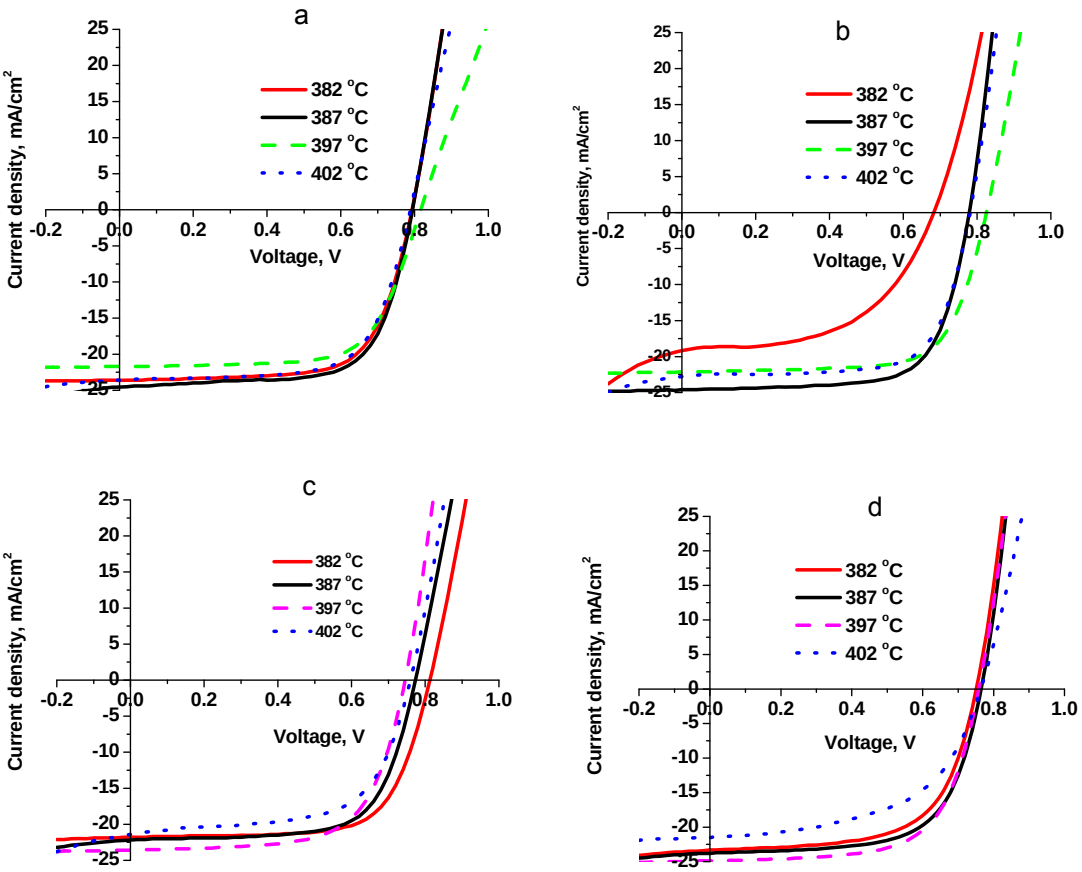

Figure 8.8 J-V curves of the best cells grown at different conditions: a) 18 mTorr, 20 W (UT standard), b) 9 mTorr, 6.6 W, c) 9 mTorr, 20 W, d) 9mTorr, 60 W (high rate) and $CdCl_2$ treated at four different temperatures.

8.3. Conclusions

The CdTe deposition rate dependence on sputtering gas pressure and RF power has been studied. It has been found that the maximum rate is achieved at 5 mTorr and the upper limit of applied power has not been identified because of concern for the integrity of the sputtering target. At a "safe" 60 W of RF power the deposition rate of 140 nm/min was achieved. The morphology of the films and the residual in-plane stress in the as-deposited films was found to have a stronger dependence on deposition pressure than power. Generally lower deposition pressure leads to more densely packed, smaller-grain-size polycrystalline films. As-deposited films have preferred (111) orientation which is randomized after $CdCl_2$ treatment just as for standard UT CdTe films. $CdCl_2$ treatment is also found to release stress in films almost completely.

Efficient cells were fabricated with CdTe layers deposited at 10 mTorr at all the different RF powers. At 133 nm/min CdTe deposition rate, a maximum of 11.8% efficiency was achieved on TEC 7 glass with no interfacial, high resistivity transparent (HRT) layer. Films deposited at very high and very low rates were found to be more sensitive to $CdCl_2$ treatment temperature variations than those deposited at our "standard" rate. Further $CdCl_2$ treatment optimization is needed to improve V_{OC} and fill factor of high-rate deposited cells.

9. XRD and SEM Studies of Pyrrole Treatment of CdTe Cells

An improved post-deposition self-healing treatment for CdTe photovoltaic devices has been developed. Aqueous solutions containing pyrrole, in place of the established reagent aniline,[21] and sodium chloride provide a self-healing treatment of the CdTe surface on illumination of the device. Evaporating gold metal onto the treated CdTe surface completes the device structure. The J-V characteristics of portions of the device treated with pyrrole and illumination compared to portions treated but not illuminated reveals a significant enhancement in device output. The performance of treatments employing pyrrole and aniline were found to be comparable, but the use of pyrrole is preferred since it is a less toxic substance than aniline.

The surface treatments are commonly employed as they provide a Te-rich layer that allows easier back-contacting, due to the formation of a degenerate semiconductor, usually a metal telluride, after metallization or an annealing step.[22] This interfacial layer allows the formation of an ohmic contact to the CdTe, which is not possible with direct metallization due to the high work function of the CdTe (>5.7eV). The aniline and pyrrole surface etch is a mild treatment option relative to the more commonly employed bromine-methanol (BM) or nitric acid/phosphoric acid (NP) treatments. The optimal treatment duration was found to be 30 minutes for both the aniline and pyrrole treatments. Degradation of the cell performance occurs for photochemical treatments using aniline or pyrrole lasting longer than one hour. An advantage with these photochemical treatments is that the Te-layer formed during the treatments is stable for a longer period of time than observed for BM and NP.[1, 23]

The TEC-15/CdS/CdTe structures used in this study were donated by Solar Fields LLC and were cut from a 60 cm x 120 cm panel to a sample size of 10 cm x 10 cm. The $CdCl_2$ treatment was conducted as a "wet"-treatment, using a saturated $CdCl_2$ solution in methanol under standard conditions. The sample was then cut in half and the two halves submersed in solution such that one half was exposed to light while the other half was shaded and not exposed to the light source. The pyrrole solution consisted of 0.15 M pyrrole, 5 M NaCl. The pH was adjusted to 6, using HCl. The aniline reference solution consisted of 0.2 M Aniline, 2 M NaCl and 0.01 M p-TSA. The illumination (1 sun) was obtained using an Eiko 300W Photo Lamp. The treatments were performed for 30 min. After treatment the cells were finished by evaporating a ~40 Å layer of gold metal as the back contact.

After the pyrrole and aniline photochemical treatments the color of the samples changed from dark to light gray. A color change can be observed after 10-15 minutes of treatment. The longer the treatment was conducted, the more pronounced was the effect, which was more distinctive for the aniline photochemical treatment compared to the pyrrole photochemical treatment.

9.1. I-V Characterization

The cell efficiencies averaged over 36 dot cells (contact area: 0.068 cm^2) on a 5 cm x10 cm plate were typically around 11% for pyrrole photochemically treated cells and 11.5% for aniline photochemically treated cells. The corresponding average values for untreated, as well as for samples in solution but not exposed to light, cells were around 10%, demonstrating the high quality of the material used in this study.

The cell parameters of the best cells obtained for the photochemical treatment in pyrrole, treated in the dark while submersed in pyrrole and photochemical treatment in aniline are shown in Table 9.1:

Table 9.1 Best cell parameters of pyrrole treated (light), pyrrole treated (dark), aniline treated (light) and untreated cells.

Parameter	Pyrrole treated (light)	Pyrrole treated (dark)	Aniline treated (light)
V_{oc} (V)	0.787	0.708	0.784
J_{sc} (mA/cm^2)	23.770	23.751	25.016
FF (%)	65.898	65.429	61.57
P_m (mW/cm^2)	12.327	10.996	12.081
R_{series} (ohm/cm^2)	4.986	5.183	4.262
R_{shunt} (Kohm/cm^2)	0.424	0.662	0.219

The cell parameters for the best cells obtained in this study (Figure 9.1) clearly demonstrate the potential of the pyrrole electrolyte surface treatment, and also show that both pyrrole and aniline light treatments provide similar increases in the efficiency of CdS/CdTe photovoltaic devices. More work is in progress to optimize the treatment parameters, such as pH of the solution, treatment time, concentration of supporting electrolyte and counterion.

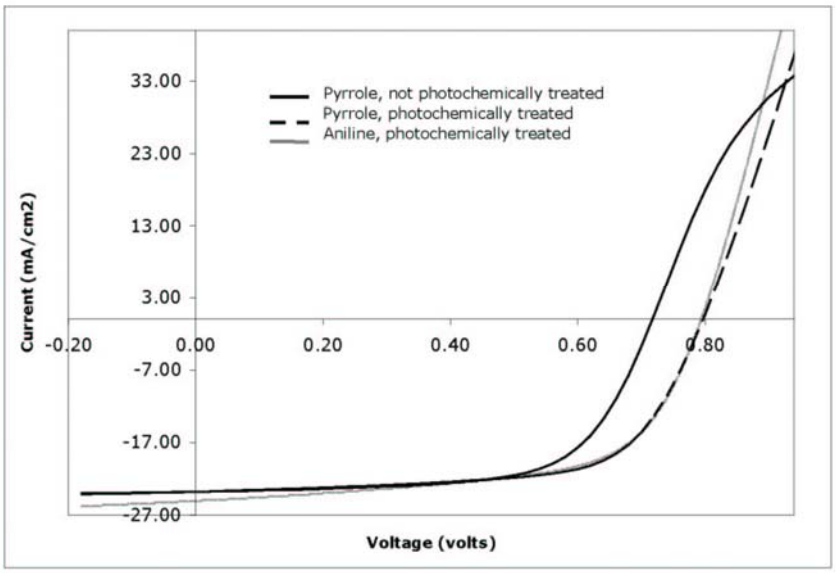

Figure 9.1 IV curves of CdS/CdTe devices with and without pyrrole surface treatment. Dot cells were 0.068 cm^2 of evaporated gold.

9.2. GIXRD-Characterization

Glancing incidence x-ray measurements were obtained with a PAN Analytical, X'PertPro PW3020Pro X-Ray diffractometer, at an incident beam angle of 0.5°. The samples used in the GIXRD study were treated for 1h, because Te could not be observed in the GIXRD after a 30 minute treatment, for both the pyrrole and the aniline photochemical treatments. The same phenomenon was reported by Dobson et al. GIXRD-measurements were performed before (Figure 9.2), and immediately after the pyrrole light treatment (Figure 9.3). The samples were measured again after 72 h of exposure to air, and no significant changes in the XRD patterns occurred, as shown in Figure 9.4. For both the aniline and the pyrrole treatments crystalline Te, shown by the Te(101) peak at 27.6°, could be found on the surface immediately after the treatment. The Te peak in the case of the aniline light treatment is more pronounced, this fact correlates with the observed visible changes on the cell surface. The complete crystallization of the tellurium layer took about 4 h in the case of the aniline light treatment, which is another hint of the thickness of Te produced. For both treatments no sign of surface oxidation was observed, even 72 h after the treatment, which is an advantage in device processing compared to common etches like BM or NP, where oxidation occurred during the first hours after the treatment.

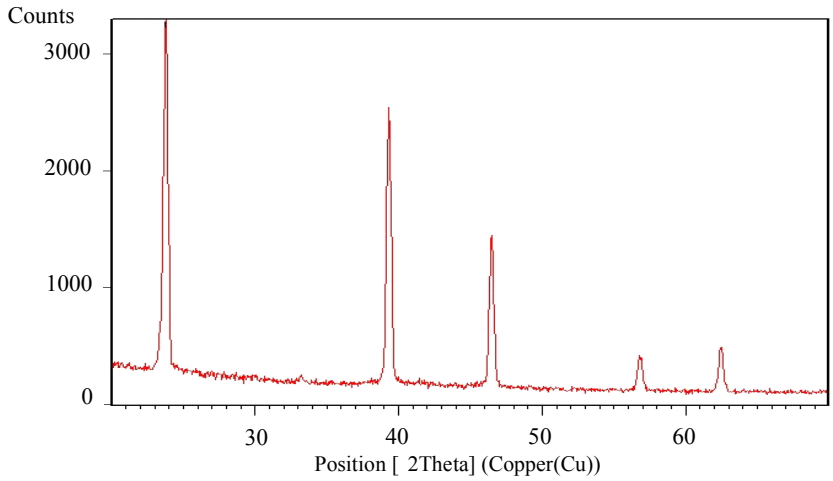

Figure 9.2 GIXRD pattern of a typical sample before light treatment

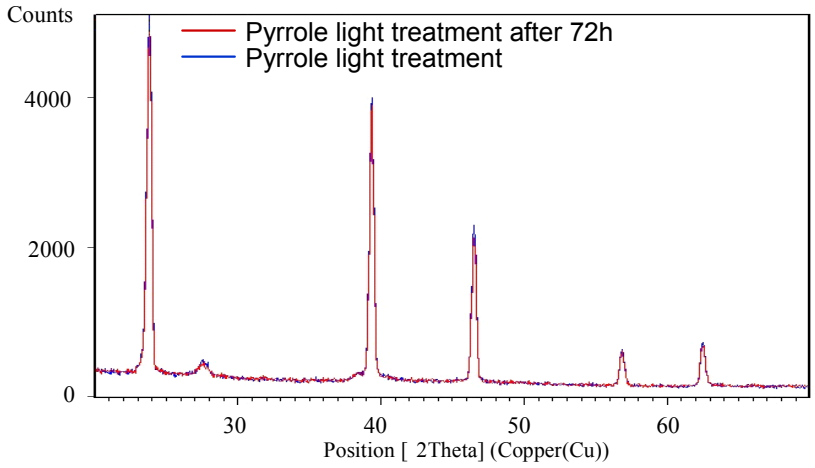

Figure 9.3 GIXRD pattern of a sample immediately after pyrrole light treatment and 72h after the treatment

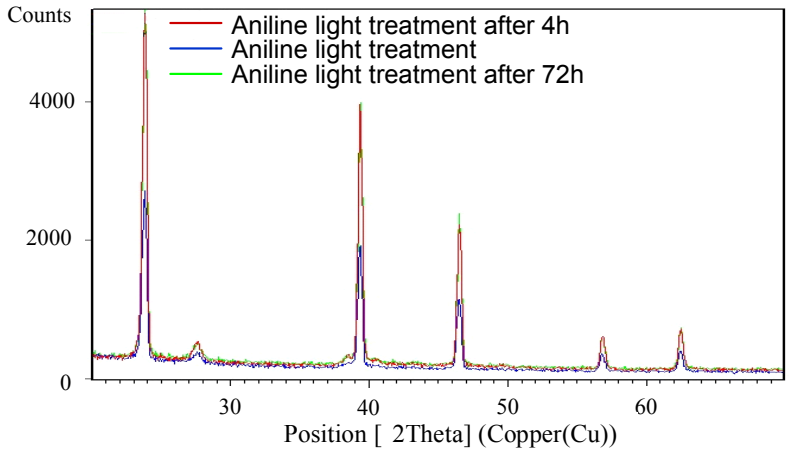

Figure 9.4 GIXRD sample immediately after aniline light treatment, 4h and 72h after the treatment

9.3. SEM-Characterization

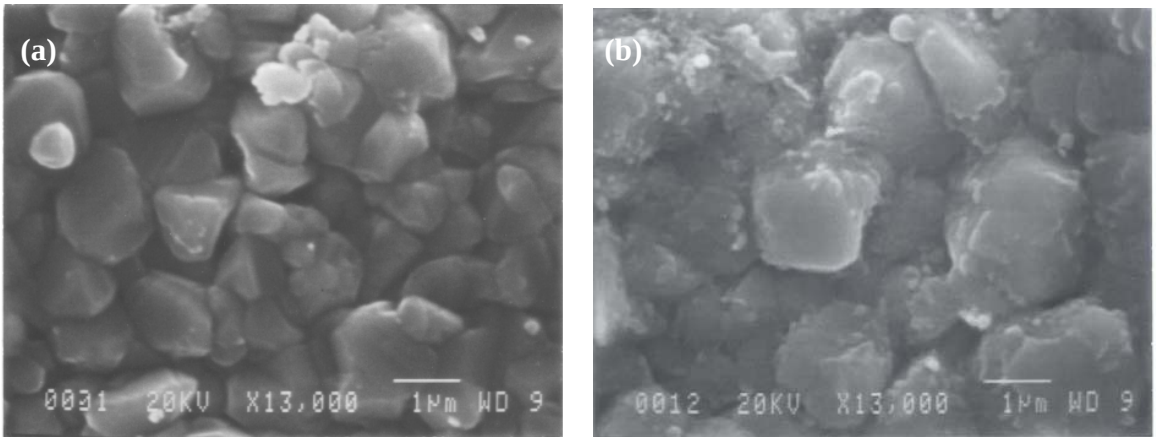

Figure 9.5 SEM images of (a) an as-deposited CdTe film, and (b) a sample after $CdCl_2$-treatment.

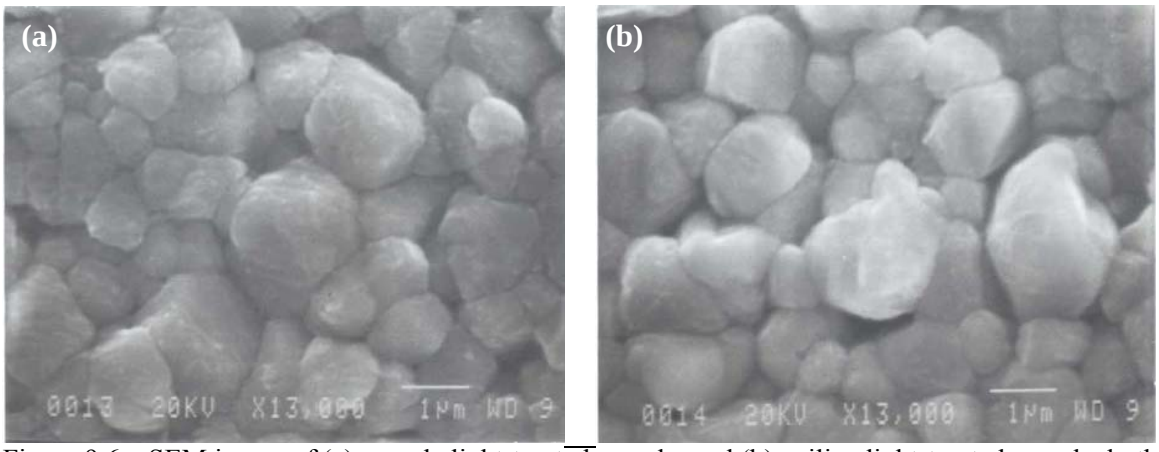

Figure 9.6 SEM image of (a) pyrrole light-treated sample, and (b) aniline light-treated sample, both after $CdCl_2$ activation.

SEM (JEOL JSM6100) images of as-deposited, $CdCl_2$ treated and both pyrrole and aniline light-treated samples are shown in Figure 9.5 and Figure 9.6. Regrowth that occurs during the standard $CdCl_2$ treatment produces a significant morphological change that reduces grain faceting and eliminates most spaces between grains thus giving rise to a more compact CdTe surface. The grains are also larger on average. Before the light treatments the CdTe surface is rather rough. Small particles are present on the CdTe surface. After the pyrrole or aniline treatment the surface appears to be still smoother with few small particles on the surface. The smoothing effect also seems more pronounced in case of the aniline treatment, which corresponds with the observation mentioned above.

10. Modeling of Ultrathin Cells (Tasks 2.1.4, 2.2.1, 2.2.2, 2.2.3, 2.2.4)t

Work on these tasks focused on modeling of the physics of degradation of devices with submicron CdTe thickness. Results were published in [V.G. Karpov, M.L.C. Cooray, and Diana Shvydka, "Physics of ultrathin photovoltaics," Appl. Phys. Lett. 89, 163518 (2006)]. A reprint of this publication is attached as Appendix A. The paper and important conclusions are summarized here, beginning with the abstract of the paper.

ABSTRACT

The authors consider physical properties of ultrathin photovoltaics with thickness (≤1 μm) smaller than both the depletion width and diffusion length, applicable to the cases of amorphous, polycrystalline, and nanostructured devices. Three phenomena underlie the unique physics of such systems: (1) lateral screening by conducting electrodes, (2) leakiness due to defect assisted tunneling, and (3) gigantic capacitive energy conducive to shunting breakdown. The authors give numerical estimates and discuss practical implications of these phenomena.

CONCLUSIONS

The implications of random potential fluctuations can be understood based on the equivalent circuit of ℓ-sized microdiodes connected in parallel through the resistive electrode (e.g., transparent conductive oxide). Strong random potential fluctuations $\delta\varphi \geq kT/e$ are detrimental, causing loss in open-circuit voltage, fill factor, and device efficiency. Our consideration predicts that suppressing such loss requires either very small or very large particle size compared to the device thickness.

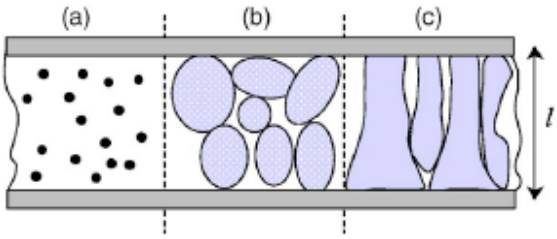

Fig. 10.1. Electric charge distributions in thin-film PV: (a) point charges due to doping impurities or defects, (b) surface charges at the interfaces of three-dimensional nanoparticles (grains) in organic or some polycrystalline photovoltaics, and (c) charges at the interfaces of columnar grains.

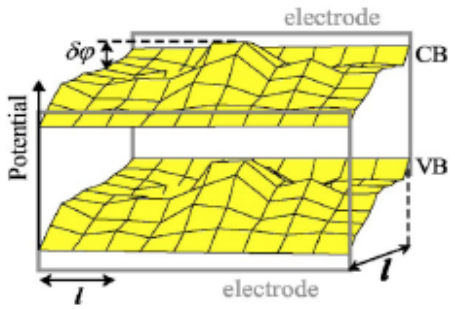

Fig. 10.2. Random electric potential fluctuations of conduction (CB) and valence (VB) bands between two equipotential electrodes (front and backplanes).

One counterintuitive consequence of the analysis presented in the paper is a higher breakdown vulnerability under low illumination, "from dusk till dawn." This happens because the area $L^2 \sim 1/J_L$ of shunt influence increases and so do its related capacitance, stored energy, and dimensionless length parameter $\alpha = (L/\ell)^2$. More exactly, since $V_{oc} \approx (kT/q)$ $\ln(J_L/J_S)$, the energy $W \sim (L^2 V_{oc}^2)$ is a maximum at low light $V_{oc} \approx 2kT/q \approx 50$ mV.

To summarize, we predict shunting to be a characteristic degradation mode of ultrathin photovoltaics (UTPV), especially detrimental under low light. A comment is in order regarding the case of polymer UTPV where flexible atomic structure is conducive to strong polaron effect accompanying the electron localization. This exponentially increases the hopping resistance R_0, thus improving the device vulnerability to leakage and dielectric breakdown. In conclusion, the characteristic physics of UTPV is due to the phenomena of electrode screening, current leakage, and shunting instability. Their respective practical implications include (1) grain (particle) sizes either much larger or much smaller than the device thickness, (2) the existence of critical thickness, below which the device performance is strongly affected by the leakage currents, and (3) the dielectric breakdown conducive to shunting, especially under low illumination. The above effects originate from purely statistical ("fundamental") fluctuations in the charge and defect density, which cannot be suppressed by technology improvements and are not accounted for by the standard device modeling. As a potential remedy we point at properly designed interfacial layers that increase the defect chain resistances, thereby mitigating the leakage and breakdown vulnerability.

[A full discussion of this analysis is given in the reprint attached as Appendix A.]

11. References (from section 1 through 10)

[1] J. Lee, P. I. Rovira, I. An, and R. W. Collins, *Rev. Sci. Instrum.* **69**, 1800 (1998); I. An, J.A. Zapien, C. Chen, A.S. Ferlauto, A.S. Lawrence, and R.W Collins, *Thin Solid Films* **455**, 132 (2004).

[2] B.E. McCandless, G.M. Hanket, D.G. Jensen, and R.W. Birkmire, *J. Vac. Sci. Technol. A* **20**, 1462 (2002).

[3] H. Fujiwara, J. Koh, P. I. Rovira, and R. W. Collins, *Phys. Rev. B* **61**, 10832 (2000).

[4] B. Johs, C. Herzinger, J. Dinan, A. Cornfeld, J. Benson, *Thin Solid Films* **313**, 137 (1998).

[5] R.W. Collins and A.S. Ferlauto, in *Handbook of Ellipsometry*, (William Andrew, Norwich, NY, 2005), p. 93.

[6] S. Ninomiya and S. Adachi, *J. Appl. Phys*. **78**, 1183 (1995).

[7] P. Hofmann, K. Horn, A.M. Bradshaw, R.L. Johnson, D. Fuchs, and M. Cardona, *Phys. Rev. B* **47**, 1639 (1993).

[8] K. Wei, F.H. Pollak, J.L. Freeouf, D. Shvydka, and A.D. Compaan, *J. Appl. Phys.* **85**, 7418 (1999).

[9] C.C. Kim, M. Daraselia, J.W. Garland, and S. Sivanathan, *Phys. Rev. B* **56**, 4786 (1997).

[10] J.I. Pankove, *Optical Processes in Semiconductors*, (Dover, New York, 1975).

[11] G.F. Feng and R. Zallen, *Phys. Rev. B* **40**, 1064 (1989).

[12] H. Windischmann, *J. Vac. Sci. Technol. A* **9**, 2431 (1991).

[13] D. Dunstan, B. Gil, C. Priester, K. Homewood, *Semicond. Sci. Technol.* **4**, 241 (1989).

[14] Xiangxin Liu, Alvin D. Compaan and, Jeff Terry, 'Cu K-edge X-ray fine structure changes in CdTe with $CdCl_2$ processing', 2004 European MRS meeting, Strasbourg, *Thin Solid Films* **480-481** (2005), pp. 95-98.

[15] "Pearson's Handbook of Crystallographic Data for Intermetallic Phases", P. Villars and L.D. Calvert, V. 2 , Metals Park, Oh : American Society for Metals, 1985.

[16] Xiangxin Liu, Alvin D. Compaan, Nadia Leyarovska, and Jeff Terry, "Cu K-edge EXAFS in CdTe before and after treatment with $CdCl_2$," Mat. Res. Soc. Symp. Proc. **763,** 139-144 (2003)

[17] A. Gupta, V. Parikh, and A. D. Compaan, *Solar Energy Materials and Solar Cells*, **90**, 2263 (2006).

[18] A. Gupta and A. D. Compaan, *Applied Physics Letters* **85**, 684 (2004).

[19] B. McCandless, J. Sites, in *Handbook of Photovoltaic Science and Engineering*, edited by A. Luque, S. Hegedus. (John Wiley and Sons, 2003) pp. 633-637

[20] M. Shao. PhD. Thesis. The University of Toledo, 1995.

[21] Y. Roussillon, D.M. Giolando, D. Shvydka, A.D. Compaan and V.G. Karpov, Appl. Phys. Lett., **84,** (2004), 616.

[22] B.E. McCandless and K.D. Dobson, Solar Energy, **77**, (2004), 839

[23] K.D. Dobson, S.A. Einstein, D.D. Sadowsky, B.E. McCandless and R.W. Birkmire, Mater. Res. Soc. Symp. Proc. **865** (2005), 293.

12. Publications

12.1. Refereed papers published or in press

1. R.W. Collins, C. Chen, M.W. Horn, S. Pursel, and C. Ross,"The ultimate in real-time ellipsometry: multichannel Mueller matrix spectroscopy", *Applied Surface Science* **253**, 38-46 (2006)

2. J. Li, J. Chen, N.J. Podraza, and R.W. Collins, "Real time spectroscopic ellipsometry of sputtered CdTe: effect of growth temperature on structural and optical properties", *Conference Record of the 2006 IEEE 4th World Conference on Photovoltaic Energy Conversion 2006*, (IEEE, Piscataway NJ, 2006) p. 392-395.

3. J. Chen, J. Li, D. Sainju, K.D. Wells, N.J. Podraza, and R.W. Collins, "Multilayer analysis of the CdTe solar cell structure by spectroscopic ellipsometry", *Conference Record of the 2006 IEEE 4th World Conference on Photovoltaic Energy Conversion 2006*, (IEEE, Piscataway NJ, 2006) p. 475-478.

4. R.W. Collins, A.D. Compaan, S. Marsillac, A. Parikh, J. Chen, and J. Li, "Optical analysis of II-VI alloys and structures for tandem PV", *FY07 DOE Review* (presented April 17-19, 2007).

5. R. W. Collins, A.D. Compaan, J. Li, and J. Chen, "RTSE studies of the fabrication of high efficiency CdTe PV", *FY07 DOE Review* (presented April 17-19, 2007).

6. J. Li, J.A. Stoke, N.J. Podraza, D. Sainju, A. Parikh, X. Cao, H. Khatri, N. Barreau, S. Marsillac, X. Deng, and R.W. Collins, "Analysis and optimization of thin film photovoltaic materials and device fabrication by real time spectroscopic ellipsometry", *Proceedings of Society of Photo-Optical Instrumentation Engineers* (accepted August 29, 2007).

7. J. Li, N.J. Podraza, and R.W. Collins, "Real time spectroscopic ellipsometry of sputtered CdTe, CdS, and $CdTe_{1-x}S_x$ thin films for photovoltaic applications", *Physica Status Solidi* (submitted June 11, 2007).

8. P. Petrik, N.Q. Khánh, J. Li, J. Chen, R.W. Collins, M. Fried, G. Radnóczi, T. Lohner, and J. Gyulai, "Ion implantation-induced disorder in single-crystal and sputter-deposited polycrystalline CdTe characterized by ellipsometry and backscattering spectrometry", *Physica Status Solidi* (submitted June 11, 2007).

9. Victor Plotnikov and Alvin Compaan, “CdS/CdTe Solar Cells Made by High-rate Magnetron Sputtering,: Mater. Res. Soc. Symp. Proc. 1012, Y12.28 (2007),

10. L. Weinhardt, S. Liu, J. Zhou, M. Baer, T. Hofmann, O. Fuchs, A. Compaan, X. Wu, and C. Heske, “X-ray and Electron Spectroscopy Investigation of Interfaces and

Surfaces in CdTe Thin Film Solar Cells," Mater. Res. Soc. Symp. Proc. 1012, Y7.6 (2007).

11. V. Parikh, A. Vasko, A.D. Compaan, and S.X. Marsillac, "Transparent Back Contacts in CdTe/CdS: Evaluation for Tandem Cells," Mater. Res. Soc. Symp. Proc. 1012, Y2.8 (2007).

12. V.G. Karpov, M.L.C. Cooray, and Diana Shvydka, "Physics of ultrathin photovoltaics," Appl. Phys. Lett. 89, 163518 (2006)

13. T. K. Wilson, Diana Shvydka and V. G. Karpov, "Propagating Electric Impulses in Thin Film PV", Proc. 32nd IEEE Photovoltaic Specialists Conference-2006, Waikoloa, Hawaii May 7-12, 2006 (IEEE Piscataway, N.J.) p. 471.

14. M. L. C. Cooray and V. G. Karpov, "Phenomenological model of CdS based thin film photovoltaics", Proc. 32nd IEEE Photovoltaic Specialists Conference-2006, Waikoloa, Hawaii May 7-12, 2006 (IEEE Piscataway, N.J. p. 542.

15. Jennifer Drayton, M. Mitra, and Diana Shvydka "Piezo-photovoltaic coupling in thin-film CdS/CdTe solar cells", Proc. 32nd IEEE Photovoltaic Specialists Conference-2006, Waikoloa, Hawaii May 7-12, 2006 (IEEE Piscataway, N.J.), p. 491.

16. Diana Shvydka, J. Drayton, M. Mitra, S.X. Marsillac, F. Jacob, "Pressure dependence of photovoltaic parameters in thin film Cu(In,Ga)Se2 solar cells", Proc. 32nd IEEE Photovoltaic Specialists Conference-2006, Waikoloa, Hawaii May 7-12, 2006 (IEEE Piscataway, N.J.), p.465.

17. M.L.C. Cooray and B.G. Karpov, "Long-range random potential in thin-film structures," Phys. Rev. B. 75, 1 (2007).

12.2. Publications and presentations at DOE Program Reviews

1. Alvin D. Compaan, Robert W. Collins, Victor Karpov, Dean Giolando "Fabrication and Physics of CdTe Devices by Sputtering," DOE Solar Energy Technologies Program Review/Peer Review Meeting, Denver, Apr 17-19, 2007.

2. R. W. Collins, A.D. Compaan, Jian Li, and Jie Chen, "RTSE Studies of the Fabrication of High Efficiency CdTe PV," DOE Solar Energy Technologies Program Review/Peer Review Meeting, Denver, Apr 17-19, 2007. (Manuscript available on-line at: http://www1.eere.energy.gov/solar/review_meeting/pdfs/p_15_collins_univ_toledo.pdf)

3. A.D. Compaan, oral invited review presentation at the Solar Program Review, "Fabrication and Physics of CdTe Devices by Sputtering" Denver, CO, April 18, 2007. (Presentation available on-line at: http://www1.eere.energy.gov/solar/review_meeting/pdfs/tf_4_compaan_univ_toledo.pdf)

13. Project Personnel

13.1. Postdoctoral Associates / Research Assistant Professors

1. Xiangxin Liu (Ph.D., University of Toledo, 5/2006)(5/06–)
2. Diana Shvydka (Ph.D. University of Toledo, 5/2002)(3/1/05 - 10/31/2006)

13.2. Graduate Students (with Principal Advisor)

1. Xiangxin Liu (Compaan)
2. Victor Plotnikov (Compaan)
3. Jian Li (Collins)
4. Anuja Parikh (Collins)
5. Jie Chen (Collins)
6. Lilani Cooray (Karpov)

13.3. Undergraduate Students

NSF Research Experience for Undergraduates (REU), Summer 2007;

1. Craig McClellan, from California University of Pennsylvania, "Accelerated Life Testing of CdTe Solar Cells with Differing Semiconductor Film Thicknesses" (advisor, Compaan)
2. Ryan Zeller, from Univ. of Toledo, "Optical Thickness Monitoring System for High Vacuum Deposition" (advisor, Compaan)

13.4. Technical Assistants

Terry Kahle (3/03–)